Diss. ETH No. 13547

Noise Characterization and Modeling of InP/InGaAs HBTs for RF Circuit Design

A dissertation submitted to the
SWISS FEDERAL INSTITUTE OF TECHNOLOGY
ZURICH

for the degree of
Doctor of Technical Science

presented by
ALEX HUBER
Dipl. El.-Ing. ETH
born July 7, 1967
citizen of Dietlikon ZH, Switzerland

accepted on the recommendation of
Prof. Dr. H. Jäckel, examiner
Prof. Dr. W. Bächtold, co-examiner

2000

Contents

Abstract

The demand for large capacities in the transmission channels as e.g. an optical fiber of telecommunication or in data-transmission systems in general is growing rapidly. The speed capability and also the sensitivity of the transmitter and receiver circuits has therefore to be improved. The requirements for the electronic circuits can only be fulfilled with an adequate transistor technology. One promising technology is the heterojunction bipolar transistor (HBT) technology based on indium phosphide (InP), which provides good high-frequency properties in order to satisfy the speed requirements. An InP HBT-technology, which is investigated in this thesis, has been developed in a previous work at the Institute of Quantum Electronics. In addition to the technology itself, the models of the transistors have to be developed, which make it possible to simulate and optimize the circuit before fabrication. For the development of these models, the transistors have to be characterized with respect to their DC, RF, and noise behavior.

The main focus of this work is the characterization and modeling of the noise properties of the transistors which are above all related to the sensitivity of receivers. To acquire the fundamentals for the noise considerations, we first give a short introduction into the theory of noisy two-ports. The individual noise phenomena such as thermal noise, shot noise, generation-recombination noise, and diffusion noise are described.

A complete characterization of the transistors was carried out by measuring the DC characteristics, the RF S-parameters, and the noise parameters for different transistor geometries, bias-points, and at different temperatures. These measurement data serve, together with the theoretical considerations, to develop and verify the small-signal and noise model. This model will be used for the simulation and optimization of the circuits and should therefore be valid in the whole frequency range where the circuits will be designed. This means for the noise model that the low- and high-frequency

noise sources have to be included.

The model is not only verified for a single device but also for complete circuits. For this purpose, we have designed and fabricated a 50 GHz amplifier, a 40 Gb/s photoreceiver with differential outputs and two oscillators providing center frequencies of 40 and 60 GHz. The selection of the circuits was mainly based on two reasons. First, to demonstrate the potential of our in-house InP HBT-technology to operate in the multi-ten gigahertz range. Second, because of the facts that the high-frequency noise is meaningful in amplifier circuits and the low-frequency noise determines the phase-noise in oscillators.

The main objective of this work was to investigate the noise properties of our InP HBT-technology and to develop a model which can be used for the design of RF circuits such as amplifiers and oscillators.

Zusammenfassung

In der Telekommunikation und Datenübertragung für z.B. Multimediaanwendungen, Videokonferenzen werden immer grössere Anforderungen an die Kapazität des Übertragungsmediums (optische Fiber) und damit verbunden, an die Geschwindigkeit und Empfindlichkeit der Sende- und Empfangselektronik gestellt. Um die nötigen Anforderungen zu erfüllen, müssen dafür geeignete Technologien zur Verfügung stehen. Die Heterobipolar Transistortechnologie (HBT) basierend auf Indium Phosphid (InP) ist dank ihrer guten Hochfrequenzeigenschaften bestens für den Einsatz in schnellen elektronischen Schaltungen geeignet. Eine InP HBT-Technologie wurde im Rahmen einer früheren Arbeit am Institut für Quantenelektronik der ETH Zürich entwickelt. Diese Technologie wurde in dieser Arbeit vor allem bezüglich der Rauscheigenschaften der Transistoren untersucht. Zudem wurden auch Schaltungen mit den HBTs entworfen und fabriziert. Um die nötigen Leistungsdaten der Schaltungen zu erreichen, müssen die Schaltungen vor der Herstellung simuliert werden können. Dazu ist es notwendig, dass die Transistoren bezüglich DC, Hochfrequenz- und Rauscheigenschaften charakterisiert werden, um daraus ein Modell für die Simulationen zu erstellen.

Der Schwerpunkt in dieser Arbeit wird auf die Charakterisierung und Modellierung der Rauscheigenschaften der Transistoren gelegt. Dazu wird zuerst eine kurze Einführung in die Theorie rauschender Zweitore gegeben. Die Rauschphänomene wie Schrotrauschen, thermisches Rauschen, Generations-Rekombinations-Rauschen, welche das Rauschen in elektronischen Schaltungen generieren, werden theoretisch betrachtet. Diese gewonnenen Erkenntnisse dienen als Grundlage für die Rauschbetrachtungen am HBT.

Um einerseits die Eigenschaften der Transistoren zu bestimmen und andererseits das Kleinsignal- und Rauschmodell zu erstellen und zu überprü-

fen, werden DC-Messungen sowie S-Parameter- und Rauschparametermessungen durchgeführt. Diese Messungen werden sowohl bei verschiedenen Transistorgeometrien und Arbeitspunkten als auch bei verschiedenen Temperaturen durchgeführt.

Das Kleinsignal- und Rauschmodell, welches zu Simulations- und Optimierungszwecken von Schaltungen verwendet werden soll, wird aufgrund der theoretischen Untersuchungen und der Messungen entwickelt. Das Modell soll im ganzen messbaren Frequenzbereich gültig sein. Das heisst im speziellen für das Rauschmodell, dass dieses sowohl die Hochfrequenz- als auch die Niederfrequenz-Rauschquellen enthalten soll.

Nicht nur die Übereinstimmung der Modelle mit den Messdaten der Einzeltransistoren wird gezeigt, sondern es wird auch die Verwendbarkeit der Modelle für den Schaltungsentwurf demonstriert. Dazu wurden ein 50 GHz Verstärker, ein 40 Gb/s Photoreceiver mit differentiellen Ausgängen und zwei Oszillatoren mit Oszillationsfrequenzen von 40 und 60 GHz entworfen und implementiert. Die Wahl der Schaltungen beruht darauf, dass das Hochfrequenzrauschen vor allem in Verstärkern und das Niederfrequenzrauschen für das Phasenrauschen in Oszillatoren von Bedeutung ist. Am Ende der Arbeit liegt ein Modell vor, mit welchem Verstärker und Oszillatoren entworfen werden können.

Chapter 1

Introduction

The transmission capacity of fiber-optical communication systems and the number of wireless applications in the millimeter-wave range have increased rapidly. High-speed electronic circuits are required for the transmission and processing of the data with data rates in the multi-gigabit per second range. The transistors incorporated in these circuits must therefore provide good high-speed characteristics to be able to handle these high data rates. Heterojunction bipolar transistors (HBT) [1, 2, 3, 4] and high electron mobility transistors (HEMT) [5] realized in different material systems are the most promising technologies to cover the speed requirements. In a previous work at the Institute of Quantum Electronics (IQE), an indium phosphide indium gallium arsenide (InP/InGaAs) HBT technology was developed [6], which provides the potential for high-speed communication circuits. This technology is the ideal candidate for investigations in the field of high-frequency circuits and was therefore used in this work.

In communication system not only high data rates, but also the sensitivity, e.g. of receiver systems, are of interest. Since the sensitivity is directly related to the noise properties of the receiver, it is a figure of merit for the smallest detectable signal level. Besides dispersion effects, the sensitivity limits therefore the maximal distance between two data regeneration circuits in a transmission system. This is a consequence of the fact that signals are attenuated during the transmission and only amplitudes larger than the noise floor can be detected. The total noise floor is determined by the noise in the incoming signal and the noise added by the receiver. The distance between the regeneration circuits determines the required number which has

a direct impact on the cost of the system. Hence, noise considerations and moreover, the optimization are important issues in data communication systems. Thus, we concentrate on the analysis of the noise properties of the InP-HBT technology.

1.1 Motivation and State-Of-The-Art

The data rates of opto-electronic communication have reached 40 Gb/s and higher using III-V semiconductor technologies. These technologies provide the potential for high-speed front-end circuits, amplifiers, and multiplexers, which are needed in these communication systems. Moreover, oscillators are required in clock and data regeneration circuits as well as for applications such as wireless communication, radar, or collision avoidance systems, which operate in the the V- and W-bands. Accurate models are necessary for the design and optimization of all these circuits.

Noise is an important issue especially in the front ends but also in oscillators. In order to predict and optimize the noise properties of the critical circuits, noise models were developed. The classical noise models have serious deficiencies when applied to microwave HBTs such as neglecting the correlation and the exclusion of the collector delay. However, there exist models which take the correlation between base and collector noise into account [7, 8] and even consider the bias- and temperature dependence of the model elements [9, 10, 11], but they have the following drawbacks. Although all these models were developed for the investigation of the noise properties of the HBT or the design of low-noise circuits in the microwave range, the noise sources incorporated in the model are frequency-independent. The variation of the power spectral densities of the noise sources with frequency may become important when the operating frequencies are extended to 40 GHz and higher. Noise models which include frequency-dependent noise sources [12] often neglect the correlation between the base- and collector noise current.

For the design of noise optimized oscillators, it is further important that the model includes the low- and high-frequency noise sources. On the one hand, the combination of low- and high-frequency noise is often missing in models of HBTs which were developed for the design of microwave circuits. On the other hand, noise models which are used to investigate the noise behavior in the low-frequency range [13, 14, 15] do not account of the microwave noise.

This work summarizes and discusses methods for noise modeling with emphasis on the correlation between base and collector current noise and on the frequency dependence of the noise source which is relevant on the one hand in the low-frequency range ($<$ 10 MHz) and in the very high frequency range ($>$ 40 GHz).

1.2 Organization

In this thesis, the major aspects of noise in InP single heterojunction bipolar transistors (SHBT) are discussed. A detailed investigation of the issues, presented in the previous sections, will be carried out.

In Chapter 2, a short introduction to the theory of noisy two-ports is given and the noise parameters, which completely describe the noise behavior of a two-port, will be explained. Furthermore, the fundamental noise phenomena with their physical origins are described.

Chapter 3 deals with the heterojunction bipolar transistor technology used throughout this work. The basic technological aspects involved in the fabrication of the devices are discussed and the epitaxial layer structure as well as the complete process flow are presented.

Chapter 4 concentrates on the experimental results of the DC, RF, and noise measurements. A complete characterization of the transistors is performed for different bias points, temperatures, device geometries, and layer structures.

In Chapter 5, the broadband noise model based on the measurement results of the previous chapter will be developed. The small-signal model is presented and model elements are determined. Most of our emphasis is attributed to the calculation of the power spectral densities of the noise sources which are included in the model. For the verification of this model, the simulation results are compared with the measurement data.

Chapter 6 summarizes the implementation of the noise-critical circuits which were designed using the noise model of the the InP HBTs. The selected circuits are a 50 GHz broadband amplifier, a 40 Gb/s differential photoreceiver, and 40 and 60 GHz oscillators. They are all key components in communication systems. For all those circuits, the design and measurement results are presented. The results are also compared with the simulations.

In Chapter 7, concluding remarks and an outlook for further investigation of noise problems in InP HBTs are given.

Chapter 2

Noise Theory

In active and passive electronic circuits and devices, we do not only find the signals carrying the information, but also additional statistical fluctuations of the currents and voltages are observed. These fluctuations are called *noise*. Noise is especially relevant in measurement equipments and in communication systems. In both applications, it can be important to detect signals with amplitudes as small as the noise level. In order to improve the signal-to-noise ratio, we have to employ low-noise devices and circuits, e.g. low-noise amplifiers. For the design and optimization of such low-noise circuits, the noise behavior of the devices must be accurately described and noise models have to be developed.

The noise behavior of devices and circuits is modeled by employing equivalent noise sources. The amount of noise is most often expressed by the power spectral density which is the voltage square, respectively current square, within a bandwidth of one Hertz. Each noise phenomenon provides its particular spectral distribution of the noise power. A specific noise phenomenon may therefore dominate the total noise behavior of a device in a specific frequency range.

In this chapter, we describe methods to analyze and describe the noise behavior of one- and two-ports (Sec. 2.1). Therefore, the parameters which are necessary for the characterization of the noise properties are explained. Section 2.2 concentrates on the physical origin of the individual noise phenomenon. The origin of each phenomenon will be analyzed in the following sections.

2.1   Noise in One- and Two-Ports

The noise behavior of a noisy one port is described by an ideal noise-free part and one noise source. Figure 2.1 shows the two possibilities to arrange the noise source. The noise source is either connected in series, as a voltage
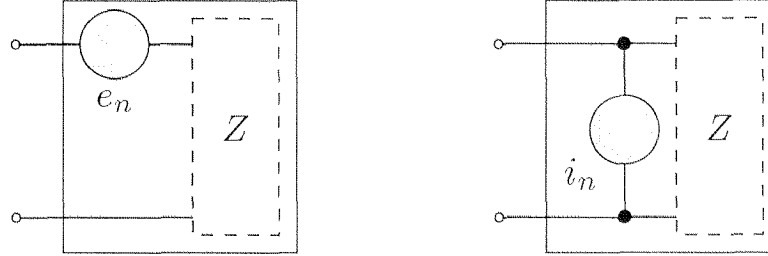

Figure 2.1: *Representation of a noisy one-port with the impedance Z*

noise source (e_n), or in parallel, as a current noise source (i_n), to the one-port. The two representations of Figure 2.1 are equivalent if $e_n = Z \cdot i_n$, where Z is the impedance of the one-port. Noise analysis is most often carried out in the frequency domain where the power spectral densities $S_{ee}(f)$, $S_{ii}(f)$ are considered. These are related to the time domain sources by

$$S_{ee}(f) = \mathcal{F}(\phi_{ee}(\tau)) \tag{2.1}$$

$$S_{ii}(f) = \mathcal{F}(\phi_{ii}(\tau)) \tag{2.2}$$

where $\mathcal{F}$ denotes the Fourier-transform and $\phi_{ee}(\tau)$ and $\phi_{ii}(\tau)$ are the auto-correlations of e_n and i_n, respectively. The power spectral densities $S_{ee}(f)$ respectively $S_{ii}(f)$ of the noise sources in Figure 2.1 can be calculated by transforming all the internal noise sources of the one-port to its input. If the internal physical processes are independent of each other, this transformation can be made individually for each internal source. Otherwise, the correlations between the processes have to be taken into account.

For the description of the noise behavior of a two-port, we use a noise-free linear two-port and two generally correlated noise sources. These two noise sources can either be placed at the input, the output or one source at each port. Analogous to the one-port, all the internal noise sources of the two-port have to be transformed into these two noise sources e_n and i_n and their correlation factor c.

The noise analysis becomes especially easy when a voltage noise source e_n and a current noise source i_n are placed at the input of the two-port. Figure 2.2 shows this configuration. The reference directions of the noise
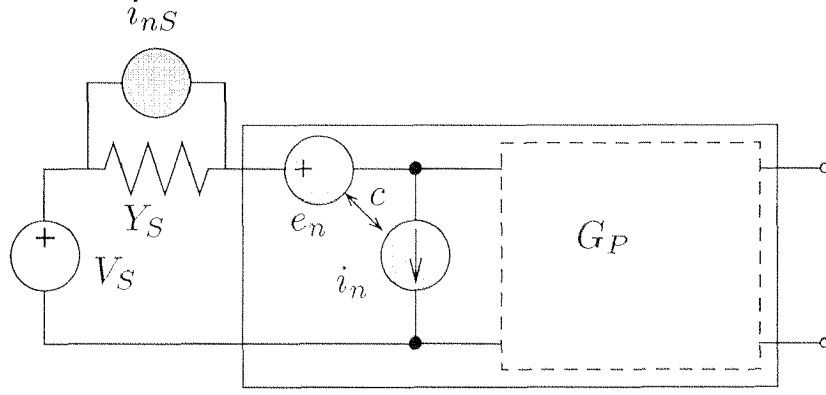
Figure 2.2: *Noisy two-port, with power-gain G_P, the voltages noise source e_n, and the current noise source i_n, connected to a signal voltages source V_S providing a noisy source admittance Y_S with a noise current spectral density of $\overline{|i_{nS}|^2}$*

sources have to be introduced for the definition of the correlation factor c is given for this configuration by

$$c_{ei} = \frac{\overline{e_n^* i_n}}{\sqrt{\overline{|i_n|^2}\,\overline{|e_n|^2}}} \tag{2.3}$$

Often, not the two noise sources, but the *noise figure F* is used to characterize the noise behavior of a two-port. The definition of F is given in Eq. (2.4).

$$F = \frac{S/N|_{\text{noisy 2-port}}}{S/N|_{\text{noise-free 2-port}}} = \frac{S_{in}/N_{in}}{S_{out}/N_{out}} = 1 + \frac{N_{2-port}}{N_S} \tag{2.4}$$

where S/N designates the signal-to-noise ratio. N_{2-port} and N_S are the noise powers of the two-port and the source, respectively. The noise figure is a measure for the noise which is added by the two-port to the noise of the signal source. The subscripts *in* and *out* denote input and output of the two-port. The noise of the two-port N_{2-port} can be expressed by the noise sources e_n, i_n, and the source admittance Y_S and the noise power of the source N_S by $i_{nS} = 4kTG_S$ (see Sec. 2.2.1), $G_S = \Re\{Y_S\}$, where $\Re$ denotes the real part. We then obtain

$$F = 1 + \frac{\overline{|i_n + Y_S e_n|^2}}{\overline{|i_{nS}|^2}} = 1 + \frac{\overline{|i_n|^2} + |Y_S|^2\overline{|e_n|^2} + 2\Re\{\overline{i_n e_n^* Y_S^*}\}}{\overline{|i_{nS}|^2}} \tag{2.5}$$

The noise figure is independent of the noise-free part of the two-port, but it is a function of the source admittance and can therefore be minimized

with respect to the source admittance Y_S. When this minimum is reached, we have noise match. The noise figure is then equal to the *minimum noise figure* F_{min} and the source admittance reaches then the *optimum source admittance* Y_{opt}. To determine this minimum, respectively optimum, we have to differentiate of Eq. (2.5) with respect to G_S and $B_S = \Im\{Y_S\}$ and set it zero. $\Im$ denotes the imaginary part. The result is then

$$F_{min} = 1 + \frac{1}{2kT_0}\left(\Re\{\overline{e_n i_n^*}\} + \sqrt{\overline{e_n^2}\,\overline{i_n^2} - \Im\{\overline{e_n i_n^*}\}^2}\right) \qquad (2.6)$$

$$R_n = \frac{\overline{e_n^2}}{4kT_0} \qquad (2.7)$$

$$G_{opt} = \sqrt{\frac{\overline{i_n^2}}{\overline{e_n^2}} - \left(\frac{\Im\{\overline{e_n i_n^*}\}}{\overline{e_n^2}}\right)^2} \qquad (2.8)$$

$$B_{opt} = \frac{\Im\{\overline{e_n i_n^*}\}}{\overline{e_n^2}} \qquad (2.9)$$

In order to determine the deviation of the noise figure from its minimum for $Y_S \neq Y_{opt}$, we use Eq. (2.10) consisting of F_{min}, the difference $Y_S - Y_{opt}$ and the noise resistance R_n.

$$F = F_{min} + \frac{R_n}{G_S}|Y_S - Y_{opt}|^2 = F_{min} + \frac{4r_n|\Gamma_{opt} - \Gamma_S|^2}{(1 - |\Gamma_S|^2)|1 + \Gamma_{opt}|} \qquad (2.10)$$

where $r_n = R_n/R_0$ is the normalized noise resistance, Γ_S is the source reflection factor and Γ_{opt} its optimum. From Eq. (2.10), we can see that R_n describes the increase of the noise figure if $Y_S \neq Y_{opt}$. The minimum noise figure F_{min}, the optimum source reflection factor Γ_{opt}, and the noise resistance R_n are not only functions of the noise sources in the two-port but also of the noise-free part of the two-port. The three *noise parameters* F_{min}, R_n, and Γ_{opt} are often used for the characterization of the noise behavior of a two-port.

When N two-ports are connected in a cascade, a general formula of the overall noise figure F can be calculated if the impedances for optimum noise match and optimum power match are identical and if the output of each two-port is matched to the input of the following stage. We then obtain *Friis's formula* [16]

$$F = 1 + F_1 - 1 + \frac{F_2 - 1}{G_{P1}} + \ldots + \frac{F_N - 1}{G_{P1} \cdot \ldots \cdot G_{PN}} \qquad (2.11)$$

which points out that for a large power gain G_{P1} of the first stage the overall noise figure F approximates the noise figure F_1 of the first stage. Hence, the input stage of a low-noise amplifier should not only have a small noise figure but also a large power gain. For that reason, we need a figure of merit which includes the stage gain in addition to the noise figure. To find this parameter, we determine the noise figure of a cascade of a large number N of identical two-ports. If $N \rightarrow \infty$ we have

$$F = 1 + \frac{F_1 - 1}{1 - 1/G_{P1}} = 1 + M \qquad (2.12)$$

where M is called the *noise measure*. It provides a good measure of the noisiness of a stage because the power gain is as well taken into account besides the noise properties of the two-port.

Previously, we have elaborated the possibilities of describing a noisy two-port by the noise sources or noise parameters. The next section will report on the physical origin of the noise sources.

2.2 Noise Phenomena

There are different types of noise phenomena in electronic devices which lead to a fluctuation of the signals. The most important types are thermal noise, shot noise, diffusion noise, generation-recombination noise, and flicker $(1/f)$ noise. The amount of contribution of one noise phenomena to the overall noise not only depends on the device and its operation principals but also on the operating conditions such as temperature, bias point, and frequency. A description of the noise phenomena is given in the following sections. More details can be found in [17, 18].

2.2.1 Thermal Noise

Thermal noise is generated in any physical resistance which shows dissipation if current is passed through it. There is no macroscopically measurable average-current if the electric field $\mathcal{E}$ is zero. However, there is a random thermal motion of the charge carriers generating microscopic current fluctuations. The direction of the charge carrier motion is changed after each impact. To determine the noise power in a solid with an area A and a length l, the currents i_1 and i_2 in the positive and negative directions, respectively,

have to be calculated.

$$i_1 = A j_1 = A n_1 q v_x = \frac{N_1}{l} q v_x \qquad (2.13\text{a})$$

$$i_2 = A j_2 = -A n_2 q v_x = -\frac{N - N_1}{l} q v_x \qquad (2.13\text{b})$$

where j_1 and j_2 are current densities, n_1 and n_2 are the carrier concentrations, N, N_1, and N_2 are the total numbers of carriers, the number of carriers flowing in positive and negative direction, respectively, v_x is the thermal velocity in x-direction, and q is the charge of an electron. The total current which is flowing is the sum of the two currents

$$i(t) = i_1(t) + i_2(t) = \frac{2 q v_x}{l} \left[N_1(t) - \frac{N}{2} \right] \qquad (2.14)$$

We do not know the exact number of carriers contributing to the two current i_1 and i_2, but we can calculate the probabilities of carriers moving in either direction. Having a probability p_1 of an electron moving in positive direction, the probability for the negative direction becomes $(1 - p_1)$. If the single events of movement are independent of each other, the probability P_{N_1} that this event is occurring N_1 times and not occurring $N - N_1$ is given by the product of the single probabilities

$$P_{N_1} = p_1^{N_1} (1 - p_1)^{N - N_1} \qquad (2.15)$$

where N is the total number of electrons. There are $\binom{N}{N_1}$ ways to chose N_1 events out of N and hence, the probability that the number of events η equals N_1 will be

$$P(\eta = N_1) = \binom{N}{N_1} p_1^{N_1} (1 - p_1)^{N - N_1} \qquad (2.16)$$

The probabilities of a single charge carrier to move in positive or negative direction are the same. Thus $p_1 = 0.5$ and as a result, the mean value $M(\eta) = N/2$ and variance $M^2(\eta) = N/4$.

Assuming that the change in the number of charge carriers is proportional to the number of carriers suffering impacts, the density function of the time distribution between two collisions will be exponential (Appendix A.1.1). We can then write for the autocorrelation function of the current $i(t)$ (Eq. 2.14)

$$\phi_i(\tau) = \overline{i(t) i(t + \tau)} = \frac{4 q^2 \overline{v_x^2}}{l^2} M^2(\eta) e^{-\tau/\theta} = \frac{q^2 \overline{v_x^2}}{l} n A e^{-\tau/\theta} \qquad (2.17)$$

where θ denotes the average time between impacts and $n = \frac{N}{Al}$. To calculate the power spectral density of thermal noise, Eq. (2.17) is transformed into the frequency domain using the Wiener-Khinchine theorem

$$S_i(\omega) = 4 \int_0^\infty \phi_i(\tau) \cos(\omega\tau) d\tau = \frac{4q^2\overline{v_x^2}}{l} nA \frac{\theta}{1 + \omega^2\theta^2} \qquad (2.18)$$

With the equipartition theorem

$$\frac{1}{2} m^* \overline{v_x^2} = \frac{1}{2} kT \qquad (2.19)$$

and the facts that the conductivity $\sigma = \frac{q^2}{m^*} n\theta$ (Appendix A.1.2) and $G = \sigma\frac{A}{l}$, Eq. (2.18) results in

$$S_i(f) = 4kTG \qquad (2.20a)$$
$$S_v(f) = 4kTR \qquad (2.20b)$$

if $\omega\theta \ll 1$ which is fulfilled for $\omega < 10^{12}$ rad/s [18]. Thus, for our considerations, the thermal noise has a white spectrum, it is proportional to the temperature and to the conductance, respectively resistance.

For very high frequencies, not only the frequency dependent term of Eq. (2.18) but also the zero-point energy of the electrons must be taken into account. Hence, we have [17]

$$S_i(f) = 4G\left(\frac{1}{2}hf + \frac{hf}{\exp(hf/kT) - 1}\right) \qquad (2.21)$$

which is identical to Eq. (2.20a) for $hf \ll kT$. At room temperatures $hf = kT$ for $f = 6$ THz. For extremely low temperatures, the increase in $S_i(f)$ should be taken into account even in the microwave region. Increasing the frequency toward optical regions, the charge carriers are causing shot noise (Sec. 2.2.2) since the optical radiation is inherently quantized. This kind of noise is called *quantum noise*.

In the HBT, thermal noise occurs in the series resistances from transistor terminals to the active region. We will see that the thermal noise of the base series resistance is one of the dominant noise sources.

2.2.2 Shot Noise

Shot noise occurs when charge carrier pass through a junction, e.g. the emitter-base or base-collector junction in a bipolar transistor. Each electron

passing the junction causes a current pulse i with the length Δt, where Δt is the time for the transition. For a constant velocity of the charge carriers, the current i carried by N_1 electrons is

$$i = \begin{cases} \frac{N_1 q}{\Delta t} & 0 < t < \Delta t \\ 0 & \text{elsewhere} \end{cases} \tag{2.22}$$

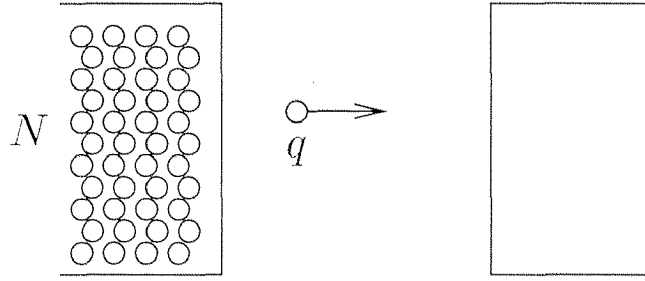The generation of this current is randomly. To determine the noise of the

Figure 2.3: *Junction where the total number of N electrons have to pass through*

current, we first have to calculate the fluctuation of the current i carried by N_1 electrons.

If the total number of N electrons pass through a junction within the time T, the probability that one single electron passes the junction is $\Delta t/T$. The movements of the electrons are independent of each other. Therefore, the overall probability is given by the product of the single probabilities. According to the Sec. 2.2.1, Eq. (2.16) we have then

$$P(\eta = N_1) = \binom{N}{N_i} \left(\frac{\Delta t}{T}\right)^{N_i} \left(1 - \frac{\Delta t}{T}\right)^{N - N_i}. \tag{2.23}$$

Because a current is flowing through the junction, the number N of the electrons is not fix. To approximate this situation, both N and T will approach infinity. In this case, we have to operate with an average number $\lambda = N\frac{\Delta t}{T}$ of electrons passing the junction. Eq. (2.23) is modified as follows

$$\lim_{\substack{N \to \infty \\ \Delta t/T \to 0}} P(\eta = N_1) = \frac{\lambda^{N_1}}{N_1!} e^{-\lambda} \tag{2.24}$$

which is the Poisson distribution. Both, the mean value $M(\eta)$ and the mean square value $M^2(\eta)$ equal to λ. The mean value of the current carried by

N_1 electrons (Eq. 2.22) is

$$i(t) = \frac{\Delta N(t) q}{\Delta t} \Rightarrow I = \bar{i} = \frac{M(\eta)q}{\Delta t} = \frac{\lambda q}{\Delta t} \qquad (2.25)$$

where $\Delta N(t) = N_1(t) - \overline{N_1}$. Using Eq. (2.22) and (2.25) the autocorrelation function of the current i can be expressed as

$$\phi_i(\tau) = \overline{i(t)i(t+\tau)} = \begin{cases} \left(\frac{q}{\Delta t}\right)^2 M^2(\Delta N)\left(1 - \frac{|\tau|}{\Delta t}\right) & |\tau| \le \Delta t \\ 0 & \text{elsewhere} \end{cases} \qquad (2.26)$$

Since the mean value $M(\eta)$ and the mean square value $M^2(\eta)$ of Eq. (2.24) are the same, we have for the autocorrelation function

$$\phi_i(\tau) = \frac{q}{\Delta t} I \left(1 - \frac{|\tau|}{\Delta t}\right) \qquad (2.27)$$

in the interval $|\tau| \le \Delta t$. Thus, the power spectral density can be calculated

$$S_i(f) = 4 \int_0^{\Delta t} \phi_i(\tau) \cos(\omega \tau) d\tau = 2qI \frac{\sin^2(\omega \Delta t/2)}{(\omega \Delta t/2)^2} \qquad (2.28)$$

In junctions with short transit times Δt, the term $\omega \Delta t \ll 1$ for frequencies below $160\,\text{GHz}$ at Δt shorter than 1 ps which is fulfilled e.g. for the collector transit time. Eq. (2.28) can then be simplified to

$$S_I(f) = 2qI \qquad (2.29)$$

which is a white spectrum. The power spectral density of the shot noise is proportional to the current flowing through the junction.

2.2.3 Diffusion Noise

Diffusion noise occurs in semiconductors with an electron density gradient $\partial n/\partial x$ where the thermally activated electrons move from locations with a high electron concentration to locations with a low concentration. The noise is caused by collisions of the moving carriers with the lattice. For modeling these collisions, the semiconductor is divided into boxes with the volume $\Delta x \, \Delta y \, \Delta z$ indicated by the indices (k, l, m). Two of these boxes are shown in Figure 2.4. Due to the collisions, the electrons can make random jumps
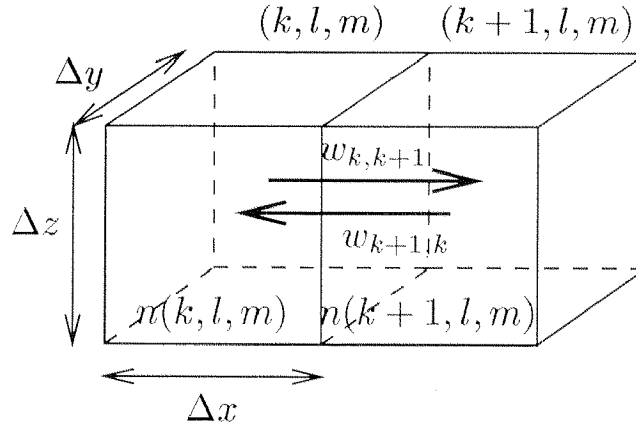
Figure 2.4: *Diffusion noise model with the two particle current $w_{k,k+1}$ and $w_{k+1,k}$ flowing between the two boxes (k,l,m) and $(k+1,l,m)$ which have an electron concentration $n(k,l,m)$ and $n(k+1,l,m)$*

from one box to its adjacent box. These jumps are assumed to be independent of each other. $n(k,l,m)$ is the charge carrier density. The particle current $w_{k,k+1}$ from the element (k,l,m) to $(k+1,l,m)$ is

$$w_{k,k+1} = a\,n(k,l,m)\,\Delta x\,\Delta y\,\Delta z \qquad (2.30a)$$

and in the reverse direction

$$w_{k+1,k} = a\,n(k+1,l,m)\,\Delta x\,\Delta y\,\Delta z$$

$$= a\left[n(k,l,m) + \left(\frac{\partial n}{\partial x}\right)_{k,l,m}\Delta x\right]\Delta x\,\Delta y\,\Delta z \qquad (2.30b)$$

where a is the probability that and electron makes a jump within the time interval Δt and has to be calculated. The net particle current $w = w_{k,k+1} - w_{k+1,k}$ is

$$w = -a\left(\frac{\partial n}{\partial x}\right)_{k,l,m}\Delta x^2\,\Delta y\,\Delta z \qquad (2.31)$$

The net particle current density $w/(\Delta y\,\Delta z)$ must be independent of the way in which the semiconductor is divided. Therefore, $a\,\Delta x^2$ has to be constant and is called *electron diffusion constant* D_n. The particle current $w_{k,k+1}$ and the net particle current w can then be expressed by

$$w_{k,k+1} = D_n\,n(k,l,m)\frac{\Delta y\,\Delta z}{\Delta x} \qquad (2.32)$$

$$w = -D_n\left(\frac{\partial n}{\partial x}\right)_{k,l,m}\Delta y\,\Delta z \qquad (2.33)$$

respectively. The particle currents $w_{k,k+1}$, $w_{k+1,k}$, and w generate electrical currents $i_{k,k+1} = qw_{k,k+1}$, $i_{k+1,k} = qw_{k+1,k}$, and $\bar{i} = qw$, respectively. The noise generated by these currents are the fluctuations Δi around the mean value which equals the net current $\bar{i}$.

$$\Delta i = i_{k,k+1} + i_{k+1,k} - \bar{i} = \Delta i_{k,k+1} + \Delta i_{k+1,k} \qquad (2.34)$$

with $\Delta i_{k,k+1} = \Delta i_{k+1,k} = D_n q n(k,l,m)\frac{\Delta y \Delta z}{\Delta x}$. The currents $\Delta i_{k,k+1}$ and $\Delta i_{k+1,k}$ are independent of each other and show full shot noise. The spectral density of these currents is then (Sec. 2.2.2)

$$S_i(f) = 2q\Delta i_{k,k+1} + 2\Delta i_{k+1,k} = 4q^2 q D_n\, n(k,l,m)\frac{\Delta y \Delta z}{\Delta x} \qquad (2.35)$$

If the current is made up of majority carriers and if the Einstein relation ($D_n = \mu_n k T/q$) holds, the diffusion noise reduces to thermal noise

$$S_i(f) = 4kT[q\mu_n n(x)]\frac{\Delta y \Delta z}{\Delta x} = \frac{4kT}{\Delta R} \qquad (2.36)$$

where

$$\Delta R = \frac{\Delta x}{q\mu_n n(x)\Delta y \Delta z} \qquad (2.37)$$

is the resistance of the box ($\Delta x\, \Delta y\, \Delta z$). If the current is determined by the minority carriers the step from Eq. (2.35) to Eq. (2.36) is not allowed and therefore, Eq. (2.35) is used for the analysis of the diffusion noise of minority carriers. Hence, we will refer to this equation for the determination of the noise of the diffusive base transport of the HBT.

2.2.4 Generation-Recombination Noise

Generation and recombination cause fluctuations in the number of free electrons producing changes in the resistance. The resistance R of a homogeneous semiconductor block of length L and cross section A is

$$R = \frac{L}{A\, q\,(\mu_n n + \mu_p p)} = \frac{L^2}{q\,(\mu_n N + \mu_p P)} \qquad (2.38)$$

where n and p are the densities of the electrons and holes, μ their mobility, and N and P are the number of electrons and holes in the volume $Vol = AL$, respectively. The number of electrons and holes are fluctuating due

to generation and recombination. Thus, we have $N = N_0 + \Delta N(t)$ and $P = P_0 + \Delta P(t)$, where $\Delta N(t)$ and $\Delta P(t)$ are the random fluctuations. The current $I(t)$ through a semiconductor with a constant voltage drop V is

$$I(t) = \overline{I} + \Delta I(t) = V \frac{q(\mu_n(N_0 + \Delta N) + \mu_p(P_0 + \Delta P))}{L^2} \qquad (2.39)$$

for the fluctuation of the current we have then

$$\Delta I(t) = V \frac{q(\mu_n \Delta N + \mu_p \Delta P)}{L^2} = \frac{V}{\overline{\overline{R}}} \frac{b \, \Delta N + \Delta P}{b \, N_0 + P_0} \qquad (2.40)$$

where $b = \mu_n/\mu_p$. Using the fact that the DC current $\overline{I} = V/\overline{\overline{R}}$ is flowing, the mean square value of the fluctuation of the current $\overline{\Delta I^2}$ can be expressed by

$$\overline{\Delta I^2} = \frac{\overline{I}^2}{(b \, N_0 + P_0)^2} \left(b^2 \phi_{NN}(\tau) + 2b\phi_{NP}(\tau) + \phi_{PP}(\tau) \right) \qquad (2.41)$$

where $\phi_{NN}(\tau)$ and $\phi_{PP}(\tau)$ are the autocorrelation functions of the electron and hole number fluctuations, respectively, and $\phi_{NP}(\tau)$ is the crosscorrelation function. Transforming Eq. (2.41) into the frequency domain, we have

$$S_i(f) = \frac{\overline{I}^2}{(bN_0 + P_0)^2} \left(b^2 S_{NN}(f) + 2 \, b \, S_{NP}(f) + S_{PP}(f) \right) \qquad (2.42)$$

where S_{NN} and S_{PP} power spectral densities of the fluctuations of the number of electrons and holes, respectively, and S_{NP} is the cross power density spectrum. For example in an n-type semiconductor where $P_0 \ll N_0$, Eq. (2.42) is simplified to

$$S_i(f) = \frac{I^2}{N_0^2} S_{NN} \qquad (2.43)$$

or in an intrinsic semiconductor only pair-wise generation and recombination occur. Thus, the number of the fluctuating electrons ΔN and holes ΔP is identical, and we have

$$S_i(f) = I^2 \left(\frac{b+1}{bN_0 + P_0} \right)^2 S_{NN}(f) \qquad (2.44)$$

To determine $S_i(f)$, the spectral densities S_{NN}, S_{NP}, and S_{PP} have to be calculated. For simplicity, only single step processes e.g. transitions between the conduction band and the valence band are treated here.

The power spectral density of the noise is determined by the autocorrelation function which is derived from the differential equation of the generation-recombination process

$$\frac{d\Delta N(t)}{dt} = -\frac{\Delta N(t)}{\tau_{gr}}$$ (2.45)

where ΔN is the fluctuation in the number of carriers, and τ_{gr} is the recombination time of added carriers. According to Eq. (2.17), the autocorrelation function is then

$$\phi_{NN}(\tau) = \overline{\Delta N^2} e^{-\tau/\tau_{gr}}$$ (2.46)

and finally, by transforming $\phi_{\Delta N}(\tau)$ into the frequency domain, the power spectral density will be

$$S_{NN}(f) = 4\overline{\Delta N^2} \frac{\tau_{gr}}{1 + \omega^2 \tau_{gr}^2}$$ (2.47)

Hence, the spectrum $S_{NN}(f)$ is known as soon as $\overline{\Delta N^2}$ and τ_{gr} are determined. These two parameters are obtained using the *master equation* (Appendix A.2.1, [19]) which is the differential equation for the probability $P(N)$ of finding N electrons in the conduction. The result of this equation is

$$\overline{\Delta N^2} = g(N_0) \left(\frac{dr}{dN} \bigg|_{N_0} - \frac{dg}{dN} \bigg|_{N_0} \right)^{-1}$$ (2.48)

and for the carrier lifetime

$$\tau_{gr} = \left(\frac{dr}{dN} \bigg|_{N_0} - \frac{dg}{dN} \bigg|_{N_0} \right)^{-1}$$ (2.49)

where r and g are the recombination rate and the generation rate, respectively. As $\Delta N = g_0 \tau_{gr}$ the spectrum of Eq. (2.47) may be rewritten as

$$S_{NN} = \frac{4g_0 \tau_{gr}^2}{1 + \omega^2 \tau_{gr}^2}$$ (2.50)

If more than one generation-recombination process having different lifetimes τ_i are involved in the noise process, Eq. (2.47) may be reformulated as

$$S_{NN}(f) = 4\overline{\Delta N^2} \sum_{i=1}^{m} p(\tau_i) \frac{\tau_i}{1 + \omega^2 \tau_i^2}$$ (2.51)

where $p(\tau_i)$ is the probability function of the lifetimes τ_i and m is the number of g-r centers.

At not too low temperatures, the generation-recombination noise has only an influence if the conductance of the semiconductor is dominated by the minority carriers, since the density of the majority charge carriers is constant and is practically equal to the density of the doping atoms.

There exists a special kind of g-r-noise called *burst* or *popcorn* noise. Generally, this type of noise is observed in passive or active devices of imperfect structure e.g. imperfect crystal in carbon film [20] resistors, $p - n$ junction [21] etc. It typically manifests itself by random pulses of variable length and equal height. Often, more than two levels are observed which can be explained by pulses being superimposed upon each other. Since burst noise has the character of g-r noise, it leads to a Lorentzian spectrum.

Generation-Recombination noise may be observed in a frequency range depending on the recombination time. In the HBT, recombination noise in the base contributes to high-frequency noise, but also Lorentzian spectra can be observed in the low-frequency range.

2.2.5   Flicker Noise

Flicker noise is a low-frequency noise with a $1/f$ slope of the spectrum and is therefore usually called $1/f$-*noise*. In contrast to the noise phenomena described in the previous sections, the physical origin of the $1/f$-noise is not fully clear [22]. One of the main questions is whether flicker noise is a bulk effect or a surface effect. Furthermore, if there is no lower frequency limit for the $1/f$-noise, the the total noise power would be infinite. Flicker noise has been observed down to 10^{-6} Hz [23] and no lower frequency limit could be found yet.

The power spectral density of this noise can generally be expressed as

$$S(f) = \frac{C}{f^\gamma} \qquad (2.52)$$

where f is the frequency of measurement. The parameter C depends on material, scattering mechanism, and operating conditions. The exponent γ is close to unity, which can be explained by a superposition of a large number of Lorentzian spectra (this is one explanation having not necessarily to be true for all kinds of $1/f$ noise). Therefore, Eq. (2.51) has to be reformulated

as

$$S_{NN}(f) = \overline{4\Delta N^2} \int_0^\infty p(\tau) \frac{\tau}{1 + \omega^2 \tau^2} \qquad (2.53)$$

The probability $p(\tau)$ has to be normalized and must have a form which leads to a $1/f$ spectrum of Eq. (2.53). This is the case for (Appendix A.2.2)

$$p(\tau)d\tau = \begin{cases} \frac{d\tau/\tau}{\ln(\tau_1/\tau_0)} & \text{for } \tau_0 < \tau < \tau_1 \\ 0 & \text{otherwise} \end{cases} \qquad (2.54)$$

One obtains for the power spectral density

$$S_{NN}(f) = \frac{2\overline{\Delta N^2}}{\pi f \ln(\tau_1/\tau_0)}[\tan^{-1}(\omega\tau_1) - \tan^{-1}(\omega\tau_0)] \qquad (2.55)$$

Figure 2.5 shows the spectrum of $S_{NN}(f)$ and in Eq. (2.56) are the corresponding formula.
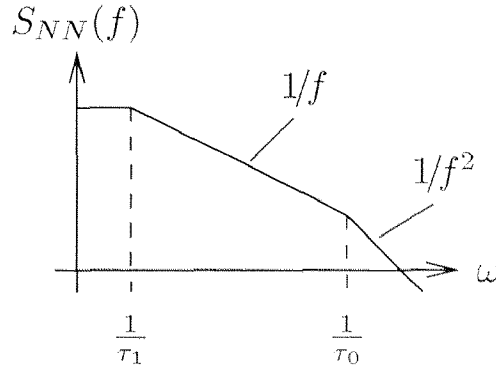
Figure 2.5: *Superposition of Lorentzian spectra with distributed time constants*

$$S_{NN}(f) = \begin{cases} \frac{4\overline{\Delta N^2}\tau_1}{\ln(\tau_1/\tau_0)} & \text{for } \omega \ll 1/\tau_1 \\ \frac{\overline{\Delta N^2}}{f \ln(\tau_1/\tau_0)} & \text{for } 1/\tau_1 \ll \omega \ll 1/\tau_0 \\ \frac{\overline{\Delta N^2}/\tau_0}{\pi^2 f^2 \ln(\tau_1/\tau_0)} & \text{for } \omega \gg 1/\tau_0 \end{cases} \qquad (2.56)$$

Over a wide intermediate frequency domain ($1/\tau_1 \ll \omega \ll 1/\tau_0$), the spectrum varies as $1/f$. For very low frequencies ($f_1 \ll 1/4\tau_1$), the spectrum is constant and above $f_2 = 1/\pi^2\tau_0$, we have a $1/f^2$ slope.

The above theory cannot be considered as a general explanation of the $1/f$ slope of the flicker noise and is only applicable if the distribution function $p(\tau)$ can be justified by the physical phenomena causing the noise. This is only possible in several cases.

$1/f$-noise as a surface effect

The low-frequency noise is generated by the charge carriers interacting with traps located in e.g. an oxide layer [24]. The distance from the semiconductor-oxide interface to the trap is y. The greater the distance y, the longer is the average time for a transition. In this case

$$\tau = \tau_0 \exp(\gamma y) \qquad\qquad \tau_1 = \tau_0 \exp(\gamma y_1) \qquad (2.57)$$

where γ is the tunneling parameter. Assuming a uniform distribution of the traps in the oxide layer, we have

$$f(y) = \begin{cases} \frac{1}{y_1} & \text{for } 0 < y < y_1 \\ 0 & \text{elsewhere} \end{cases} \qquad (2.58)$$

From this distribution of the trap locations, we can calculate the distribution function $p(\tau)$ of the time constants τ. By the fact that $f(y)dy = p(\tau)d\tau$, the density function of the time constants τ is $p(\tau) = f(y)\frac{dy}{d\tau}$, resulting in

$$p(\tau) = \begin{cases} \frac{1/\tau}{\ln(\tau_1/\tau_0)} & \text{for } \tau_1 < \tau < \tau_0 \\ 0 & \text{otherwise} \end{cases} \qquad (2.59)$$

which is a continuous distribution of time constants τ with the statistical weights proportional to τ^{-1}. In analogy to Eq. (2.54) to (2.56), this leads to a $1/f$ spectrum in the range from $1/\tau_1 \ll \omega \ll 1/\tau_0$.

$1/f$-noise as a bulk effect

The bulk effect causing the $1/f$-noise is a fluctuation in the conductance respectively resistance [22]. If we have a resistor of the length L which contains N electrons with the mobility μ, the resistance R can be written as

$$R = \frac{L^2}{q\mu N} \qquad (2.60)$$

Only N and μ can fluctuate resulting in *number fluctuation* if N fluctuates or *mobility fluctuation* [25] if μ fluctuates.

When number fluctuation causes the $1/f$ noise in a resistor with the voltage drop V, we have

$$\frac{S_V(f)}{\overline{V}^2} = \frac{S_R(f)}{\overline{R}^2} = \frac{S_N(f)}{\overline{N}^2} = \frac{\overline{\Delta N^2}}{\overline{N}^2 f \ln(\tau_1/\tau_0)} = \frac{\alpha}{f\overline{N}} \qquad (2.61)$$

In several experiments, α was too low to be explained by number fluctuation [25] and rather mobility fluctuation is the the reason for $1/f$ noise. Mobility fluctuation noise is assumed to be caused by electrons interacting with slowly fluctuating acoustical-phonons. Since in many experiments, no lower frequency limit as in Eq. (2.56) could be found, Hooge postulated [26] a general form for the flicker noise

$$\frac{S_V(f)}{\bar{V}^2} = \frac{S_I(f)}{\bar{I}^2} = \frac{S_\mu(f)}{\bar{\mu}^2} = \frac{\alpha_H}{fN} \qquad (2.62)$$

where the Hooge parameter α_H is determined by the effective mobility μ. Assuming that μ_{latt} is the mobility due to lattice scattering and μ_{imp} the mobility due to impurity scattering, we have

$$\frac{1}{\mu} = \frac{1}{\mu_{latt}} + \frac{1}{\mu_{imp}} \qquad \frac{\delta\mu}{\mu^2} = \frac{\delta\mu_{latt}}{\mu_{latt}^2} + \frac{\delta\mu_{imp}}{\mu_{imp}^2} \qquad (2.63)$$

where $\delta\mu_{latt}$ and $\delta\mu_{imp}$ are the independent fluctuations of μ_{latt} and μ_{imp}, respectively. For the power spectral densities, this leads to

$$\frac{S_\mu(f)}{\mu^2} = \left[\frac{S_\mu(f)}{\mu^2}\right]_{latt}\frac{\mu^2}{\mu_{latt}^2} + \left[\frac{S_\mu(f)}{\mu^2}\right]_{imp}\frac{\mu^2}{\mu_{imp}^2} \qquad (2.64)$$

Often, especially for low doping levels, $[S_\mu(f)/\mu^2]_{imp}$ is negligible and lattice scattering, which is scattering due to acoustical-phonons, predominates. Therefore, the Hooge parameter can be expressed as follows

$$\alpha_H = \alpha_{H0}\left(\frac{\mu}{\mu_{latt}}\right)^2 \qquad (2.65)$$

The parameter α_{H0} was experimentally found to be a constant of the value 2×10^{-3} [26].

Several types of $1/f$ noise were discussed in the above sections. In HBTs, low-frequency noise originating from recombination at the base-emitter interface or base surface [13, 27] as well as mobility fluctuation [28, 29] were observed. However, there is no general rule to determine which of those types dominates the flicker noise in a particular case. The dominant $1/f$ noise source may be found experimentally by investigating the dependences on bias point, geometry, doping level etc. [30].

2.3 Summary

This chapter gave an introduction into the theory of noisy two-ports. The noise properties can either be described by the power spectral densities of the noise sources or by the noise parameters minimum noise figure F_{min}, noise resistance R_n and optimum sources reflection coefficient Γ_{opt}. The description using the power spectral densities is applied in the low-frequency range and the noise parameters are used for the high-frequency range. Furthermore, all the noise phenomena such as thermal noise, shot noise, diffusion noise, generation-recombination noise, and flicker ($1/f$) noise were analyzed. Thermal noise and shot noise are, in a large frequency range, independent of frequency and have therefore a white spectrum. They are the dominant noise sources in a wide frequency range. Noise originating from generation-recombination processes show a Lorentz-type spectrum. Generation-recombination noise can be observed in a large frequency range since the corner frequency is related to the carrier lifetime, which can vary from a few seconds down to picoseconds. The spectrum of flicker noise is inverse proportional to the frequency and is therefore also called $1/f$-noise. This type of noise only influences the noise behavior of a device in the low-frequency range. The $1/f$-corner frequency can range from some Hertz to a few MHz, depending on the device. Flicker noise may determine the noise behavior of an oscillator because the noise can be mixed to the oscillation frequency.

Chapter 3

Technology of the InP/InGaAs HBT

One major advantage of heterojunction bipolar transistors (HBT) is that not only the device geometries and the vertical doping profiles can be varied, but also different materials can be chosen for different transistor regions. This fact relaxes various tradeoffs which have to be made in conventional homojunction bipolar transistors. Using a wide band gap material for the emitter and a narrow band gap material for the base, an almost unity emitter efficiency can be achieved independently of the emitter to base doping ratio. An InP emitter together with a lattice-matched InGaAs base fulfill these criteria optimally. The high carrier mobilities in these two materials make them ideal candidates for high speed devices. Furthermore, InP-HBTs offer the possibility to monolithically integrate $p - i - n$ photodiodes with pre-amplifiers [31], driver circuits and lasers, which enhances the potential and performance of opto-electronic integrated circuits (OEIC).

When the materials for the different transistor regions are determined, the vertical layer structure and the device geometries have to be chosen in order to find the optimal tradeoffs for a variety of device properties. These tradeoffs are e.g. current gain versus base resistance, transit frequency f_T versus base resistance, f_T versus breakdown voltage etc. A detailed investigation for the optimization of these tradeoffs can be found in [6]. In the next sections, we give a brief overview of the layer structure (Sec. 3.1) and of the main processing steps of our in-house HBT technology [6] (Sec. 3.2). These two sections summarize the considerations which led to the particular

device structure of the HBTs used in the experiments on device characterization, modeling and for the circuit design.

3.1 Vertical Structure

The vertical device structure mainly determines important characteristic parameters of the HBT such as current gain, transit frequency, breakdown voltage etc. Hence, the vertical structure has to be carefully optimized to find an optimal structure for the application specific tradeoffs.

3.1.1 Emitter and Base-Emitter Heterojunction

Since HBTs have the advantage that they can reach almost unity emitter efficiency independently of emitter to base doping, they are relatively insensitive to emitter thickness and doping. These two parameters mainly determine the tradeoff emitter series resistance versus base-emitter depletion capacitance.

The design of the base-emitter heterojunction is much more relevant for device operation than the emitter itself. An abrupt junction, as used in the HBTs throughout this work, causes the electrons to be injected with excess kinetic energy into the base and hence, reduces the base transit time [32]. A too large energy influences the avalanche multiplication in the collector which can reduce the breakdown voltage [33]. Comparisons between abrupt and graded junctions showed [34] that for a given base delay time, the implementation of an abrupt junction permits the use of a thicker base and thus, lowers the base resistance compared to graded junctions. Since an abrupt junction increases the turn-on voltage of the device, the relatively small conduction band offset of the InP/InGaAs junction of 0.23 eV (compared to e.g. a AlInAs/InGaAs junction, 0.5 eV) represents a good compromise between high intrinsic speed, low base resistance, and high breakdown voltage. Moreover, the base-emitter junction determines the turn-on voltage of the transistor and the ideality factor of the base-emitter diode.

3.1.2 Base

In the base region, a low base resistance can mainly be traded for high current gain and low base delay. For low thermal noise of the base resistance and for a high power gain at high frequencies, the base resistance must be

small (see Eq. (4.4)). This can be reached with a high base doping or a large base thickness X_B. The latter is not preferred since the base delay τ_B which is in first approximation given by [35]

$$\tau_B \simeq \frac{X_B^2}{2D_n} \tag{3.1}$$

would be increased (D_n : electron diffusion constant). As a consequence, the transit frequency, which is dominantly influenced by the base and collector delays (Eq. (4.3)), can be reduced. Hence, the base doping should be as high as possible which is additionally advantageous for low base contact resistances. The upper limit of the base doping concentration is determined by technological aspects such as maximum dopant level of the epitaxial growth and the abruptness of the doping profile, respectively dopant out-diffusion. Furthermore, when the base is too heavily doped, the lifetime of the minority carriers is reduced leading to elevated bulk recombination. This decreases the small-signal current gain of InP/InGaAs HBTs which is mainly determined by base recombination [36]. The small-signal current gain β can be expressed as [37]

$$\beta \propto \frac{2L_n^2}{X_B^2} \tag{3.2}$$

where $L_n = \sqrt{D_n \tau_n}$ is the electron diffusion length and τ_n denotes the electron minority carrier lifetime. From Eq. (3.2) we further see that β increases with the inverse of the square of the base thickness. High β values are not only advantageous for setting the bias point of the transistors in a circuit but also to lower base current noise which is proportional to the base current.

Although the base delay is reduced and the small-signal current gain is increased with decreasing base width, the base should not be too thin. Very thin bases ($< 50\,\text{nm}$) can be problematic, as the electrons pass the base ballistically and enter the collector with an excess energy leading to scattering mechanisms, which increase the collector delay. In addition, ohmic contacts to extremely thin base layers are difficult to realize with good reliability due to contact metal diffusion into the base-collector junction.

As a general rule for the base design, the base doping should be as high as possible and the base thickness is chosen to find the optimal and application-specific tradeoff related to current gain and base delay versus base resistance.

3.1.3   Collector

The thickness and doping profile of the collector influence a series of properties of the HBT such as breakdown voltage, collector delay, base-collector capacitance, output conductance, and maximum collector current density.

The breakdown voltage BV_{CE} is an important parameter of transistors because it limits the output voltage swing. For a high breakdown voltage a large collector width X_C is required. The collector width influences the speed properties of the device as well. On one hand a large collector space charge width X_C increases the collector delay τ_C which is given by [38]

$$\tau_C = \frac{X_C}{2v_{sat}} \tag{3.3}$$

where v_{sat} is the electron saturation velocity. This reduces the transit frequency. On the other hand, the base-collector capacitance is diminished which is advantageous to achieve high f_{max} values. High speed devices are often designed with a thin collector. Nevertheless, high f_{max} values can be achieved by an under-etching of the base, resulting in a reduced collector area and therefore in a reduced base-collector capacitance.

Furthermore, the collector width has an impact on the critical collector current density J_{CK} which determines the drop of f_T in the f_T vs. I_C characteristics. J_{CK} is given by the collector current density for the onset of the base push-out [39].

$$J_{CK} = qv_{eff} \left[\frac{2\varepsilon_r \varepsilon_o (V_{CB} + V_{bi})}{qX_C^2} + N_C \right] \tag{3.4}$$

where v_{eff} is the effective carrier velocity. As the collector width is increased, J_{CK} is reduced.

When designing OEICs, the base-collector junction can be used as photodiode co-integrated with electronic circuits. In this case, the collector width does not only influence the depletion capacitance of the diode and the carrier transit time but also its responsivity [40]. With a thicker collector, more photons can be absorbed in the depleted region of the collector and therefore, the responsivity of the photodiode is improved.

3.1.4   Layer Structure

The vertical layer structures of the transistors investigated in this work was developed for high-speed circuits of fiber-optical communication systems

[6] such as laser drivers [41] or optical receivers [42]. The specific parameters of each layer are given in Table 3.1.

Layer	Material	Type	Thickness [nm]	Doping [cm^{-3}]
Cap	InGaAs	n^+	300	Sn: $2 \cdot 10^{19}$
Emitter	InP	n^+	50	Si: $1 \cdot 10^{19}$
Emitter	InP	n	250	Si: $4 \cdot 10^{17}$
Spacer	InGaAs		5	undoped
Base	InGaAs	p^+	80 / 75 / 50	Zn: $3.5 \cdot 10^{19}$
Collector	InGaAs	n^-	800 / 600 / 400	Sn: $1 \cdot 10^{16}$
Collector	InGaAs	n^+	50	Sn: $1 \cdot 10^{19}$
Subcollector	InGaAs	n^+	1100 / 340	Sn: $1 \cdot 10^{19}$
Substrate	InP:Fe	S.I.		

Table 3.1: *Vertical layer structure of the InP/InGaAs HBT grown by MOVPE*

The device layer structure is grown by metal organic vapor phase epitaxy (MOVPE). A heavily doped InGaAs cap layer and a wide band gap InP layer form the emitter of the HBT. The cap layer is introduced in order to achieve good ohmic emitter contacts where values of $\rho_{cE} \simeq 1.5 \cdot 10^{-7}$ Ωcm^2) were reached. The InP emitter and the InGaAs base constitute the heterojunction. There is a spacer layer between the emitter and the base to prevent the out-diffusion of the Zn from the base into the emitter. The base thicknesses of the devices was not the same in all experiments. We explored layer structures with base thicknesses from 80 nm down to 50 nm. This reduction improved the high speed properties due to the lower base delay. Furthermore, the current gain increased. The base dopant level of Zn: $3.5 \cdot 10^{19}$ cm^{-3} is the maximum achievable with the MOVPE-growth technology. An InGaAs layer doped to Sn: $1 \cdot 10^{16}$ cm^{-3} forms the collector. The reduction of the collector thickness from 800 nm down to 400 nm trades low base-collector capacitance and good responsivity of the photodiode for low collector delay time. For a low collector series resistance a heavily doped InGaAs layer (Sn: $1 \cdot 10^{19}$ cm^{-3}) builds the subcollector, which is the connection between the collector contact and the active collector area. A thick subcollector of is useful for the operation of high collector currents when the voltage drop over the collector series resistance can lead to saturation problems. On the other hand, it is harmful for the thermal properties. As a consequence, the thickness of the subcollector layer was reduced from 1100 nm down to 340 nm.

The different thicknesses of the base, collector and subcollector refer to the different layer structures of the wafers used in different experiments. Most of the noise characterization and modeling were carried out using the HBTs having the structure with a base and collector layer thicknesses of $X_B = 80\,\text{nm}$ and $X_C = 600\,\text{nm}$, respectively, whereas the designs of the high-speed circuits were implemented using the devices with $X_B = 50\,\text{nm}$ and $X_C = 400\,\text{nm}$.

3.2 Processing

After the epitaxial layer growth by MOVPE the HBT is processed in order to determine the lateral dimensions of the transistors. Moreover, the resistors, and capacitors are formed. The lateral dimensions have generally a large influence on the parasitic elements. Therefore, the processing steps consisting of etching steps, lift-offs, evaporation of metals etc., have to be carefully optimized in order to minimize these parasitics. The major parasitics are the series resistances and in particular the contact resistances which can be minimized using optimal metal deposition techniques. Furthermore, self-aligned processing steps help to minimize the distance between the transistor terminal and the active region, which also reduces the series resistance, e.g. the base resistance. Under-etching techniques can further reduce parasitic capacitances e.g the extrinsic base-collector capacitance. The process flow shown in Figure 3.2 will be described next.

1. The emitter mesa is formed by wet chemically etching. The etchant is material selective for InP and InGaAs which enables the complete stopping of the emitter-etch at the emitter-base interface. An other advantage of this method is the fact that the etching is crystal orientation dependent which forms an emitter undercut profile. The emitter can therefore be used as mask for the base metalization deposition without the creation of emitter-base shortcuts. In this way, the distance between the base contact and the emitter, as well as the exposed base surface, is minimized. The former reduces the base series resistance, and therefore the thermal noise of the base resistance. The latter may cause a decrease of the low-frequency noise because the area, where surface recombination can take place, is reduced.

2. When the emitter structure is formed, the base and emitter metalizations can be deposited. The same non-alloyed metalization scheme

(Ti/Pt/Au) can be applied for the p-contact to the base and the n-contact because of the narrow band gap of the InGaAs and the very high doping levels of the base and the emitter cap. A low specific contact resistance ($\rho_{cB} \simeq 3 \cdot 10^{-7}\ \Omega \text{cm}^2$) with very little penetration of the metal into the InGaAs is achieved. This is very important when contacting thin bases ($X_B < 100\,\text{nm}$). The thickness of the Au should be chosen as large as possible (55 ... 70 nm depending on the wafer) in order to reduce the series resistance of the metalization, but a too thick base metal could form base-emitter shorts.

3. Once the deposition of the base- and emitter metalization is completed, the base collector mesa is formed by wet chemical etching, which is self-aligned to the base metalization. Figure 3.1 shows a SEM (scanning electron microscopy) photograph of an HBT with an emitter area of $1.5 \times 5\ \mu\text{m}^2$ after this etching step. Part of the base contact is under-etched in order to reduce the base-collector capacitance. To prevent mechanical instability of the contacts, excessive under-etching must be avoided. The etching of the collector is stopped at the subcollector by an InP etch-stop layer.
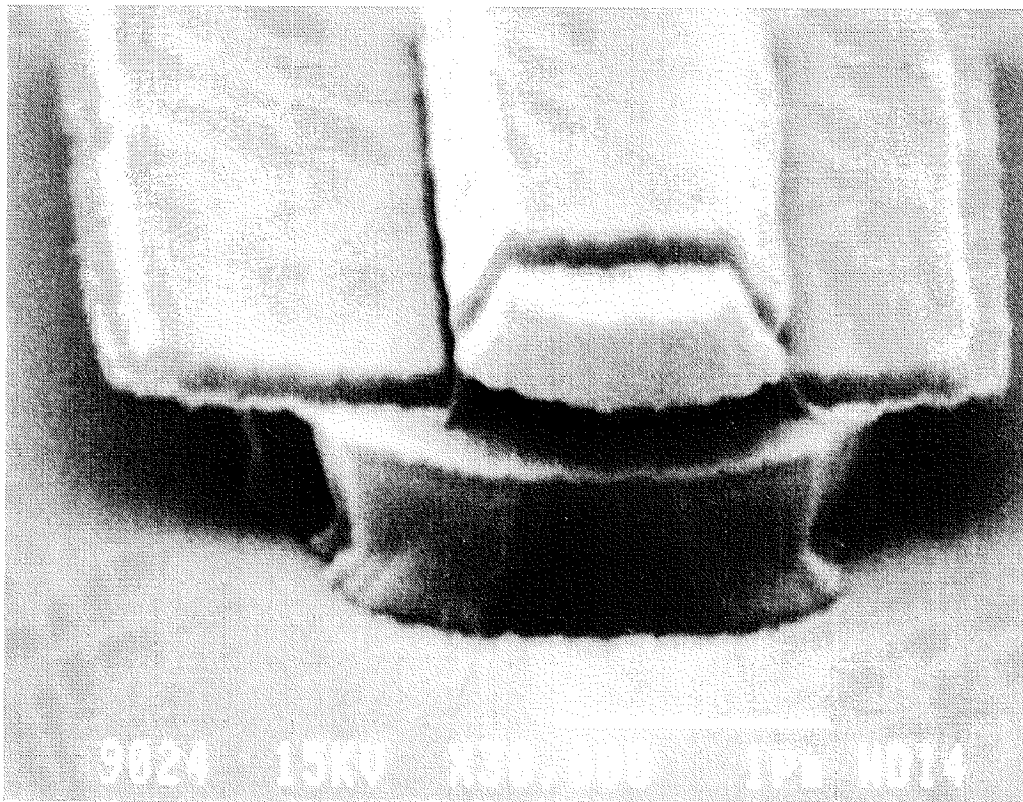
Figure 3.1: *SEM photograph of an HBT with an emitter area of* $1.5 \times 5\ \mu m^2$

4. After completion of the base-collector mesa etching, the collector metalization formed by Ti/Pt/Au can be deposited onto the InGaAs subcollector layer. As this metalization layer is also used as first interconnect metal, a low series resistance must be achieved and hence, the metal layer should be relatively thick. A specific contact resistance of $5 \cdot 10^{-8}\,\Omega\mathrm{cm}^2$ is obtained for Ti/Pt/Au of 30 nm/40 nm/500 nm.

5. The subcollector layer is wet chemically etched down to the semi-insulating InP in order to isolate the devices from each other. Since the sheet resistance of the subcollector is $10 \dots 15\,\Omega/\square$, this layer is suitable to form resistors with low values ($< 50\,\Omega$).

6. The previous etching steps formed a highly non-planar device structure which has to be planarized for the second level interconnect metal. Moreover, a dielectric is required for accessing the device terminals and the device structure has to be passivated in order to reduce leakage currents. The reduced leakage currents may also decrease the low-frequency noise level [43]. Polyimide has been used because it provides good planarization characteristics, good dielectric performance and excellent passivation of the InP based material surfaces [44].

   To be able to contact very small emitter sizes, a technique for self-aligned emitter access is required. Therefore, the wafer is coated with thick polyimide to obtain a fully planarized surface. This polyimide is etched back until the emitter contact is exposed. The minimum of the emitter width ($\approx 0.7\,\mu\mathrm{m}$) is generally given by the fact that surface recombination currents begin to dominate the base current. This reduces the current gain (Fig. 4.5).

   The base and collector are accessed using photolithographically defined via-etching. The minimum opening of the is about $1.5\,\mu\mathrm{m}$. This value is limited by the minimum feature size and the alignment tolerance of the mask, which are $0.6\,\mu\mathrm{m}$ and $0.5\,\mu\mathrm{m}$, respectively. This method is also used to form the via holes for the placing the Cr-resistors and the MIM-capacitors. A

7. There are several possibilities to form capacitors. The first is the reverse biased base-collector depletion capacitance. Its specific capacitance is a function of the collector width and varies from $0.35\,\mathrm{fF}/\mu\mathrm{m}^2$ to $0.45\,\mathrm{fF}/\mu\mathrm{m}^2$ for the collector width of 800 nm and 500 nm. This capacitor type should only be used as DC-block because of their voltage dependence. A second type of capacitor is formed by the first

and second (processing step Nr. 9) level interconnect metals and the polyimide as dielectric having a specific capacitance of $0.037\,fF/\mu m^2$. This type can only be used for small capacitor values ($< 50\,fF$). Otherwise the chip area consumption would be too large which would additionally have detrimental effects on the microwave behavior. The last kind of capacitor requires an additional processing step because it uses tantalum pentoxide (Ta_2O_5) instead of polyimide as dielectric. The Ta_2O_5 is deposited onto the collector metalization in the previously etched via openings. The specific capacitance was measured to be $0.45\,fF/\mu m^2$.

8. Resistors with higher values ($> 200\,\Omega$) formed by the subcollector layer would be longer than $100\,\mu m$. This would introduce parasitic inductances and delays, which can be a serious drawback especially in feedback amplifiers. Hence, resistors are required with a higher sheet resistance. These are formed by Cr-films deposited directly onto the semi-insulating InP substrate within the opening previously etched into the polyimide. The Cr-resistors have a sheet resistance of $50\,\Omega/\square \pm 5\%$.

9. The final processing step is the deposition of the second level interconnect metal which should provide low sheet resistance and good adhesion to polyimide. A metalization scheme with $30\,nm$ of Cr and $700\,nm$ of Au fulfills these requirements and a sheet resistance of $50\,m\Omega/\square$ is achieved.

3.3 Summary

In the preceding sections, the vertical structure, grown by MOVPE, of our InP/InGaAs HBTs and the main processing steps were presented. The abrupt InP/InGaAs heterojunction constitutes a good compromise between high intrinsic speed and low turn-on voltage. To obtain a low base and base contact resistance, the base doping is as high as technologically possible. Our devices have different base and collector thicknesses which will help to investigate their influence on current gain, speed properties and breakdown.

Wet-chemical etching and metal deposition steps lead to a self-aligned fabrication of the SHBT with reduced parasitics. Self-aligned base and emitter metalization deposition and the under-cut of the base metalization reduce the base resistance and the base-collector junction capacitance, respectively.

Emitter
Base
Collector
Subcollector
Substrate

1

2

3

4

5

6

MIM-Capacitor

7

Cr-Resistor

8

B   E   B   C

9
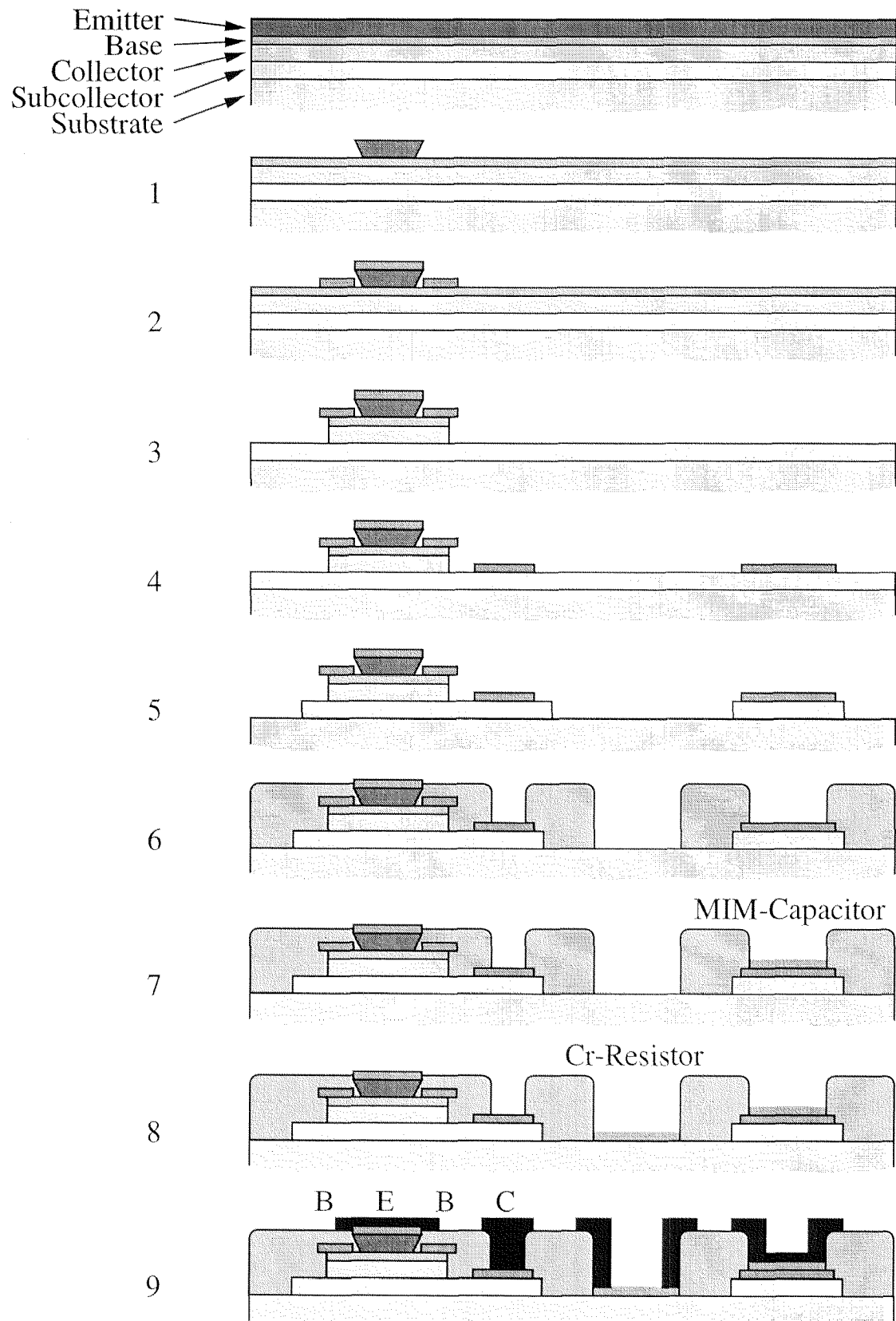
Figure 3.2: *Overview of the process flow for the fabrication of the InP SHBTs, Cr-Resistors, and MIM-Capacitors*

Chapter 4

Measurements and HBT-Characterization

In this chapter, the experimental DC, high-frequency and noise character-istics of the InP SHBT investigated during this work are presented. These measurements serve as basis for the development of the noise model. The interpretation of the measurement results is carried out by employing simple formulas derived in the literature. A more detailed analysis will be given in the modeling chapter (Chapter 5). Devices with different layer structures were examined. Furthermore, some processing steps were changed during this work as well. The influence of these technological modifications on the characteristic parameters of the devices are only described where it is relevant for the high-frequency and noise properties of the transistor.

4.1 DC-Characteristics

For the DC characterization of a bipolar transistor, mainly two types of mea-surements have been carried out. The first is the output characteristic which describes the collector current versus collector-emitter voltage and the sec-ond is the Gummel-plot which shows the collector and base currents versus the base-emitter voltage. The Gummel-plot is therefore useful to investigate the quality of the base-emitter junction.

The DC characteristics of the HBTs are obtained from on-wafer mea-surements using a parameter analyzer (HP 4145B). Although DC signals

are measured, the devices cannot be contacted with DC probe tips because the HBTs tend to oscillate. These oscillations would either lead to unacceptable measurement errors or even destroy the device. In order to prevent these oscillations the transistor has to be properly terminated to $50\,\Omega$ for frequencies in the RF range. To achieve the $50\,\Omega$ termination, the DC-bias must be applied via bias-tees with a $50\,\Omega$ resistor connected to the RF input of the bias-tee. The bias-tees are connected to ground-signal-ground (GSG) RF probe tips which contact the pads on the wafer. Coplanar lines connect these pads with the HBT.

4.1.1 Output Characteristics

Figure 4.1 shows a typical output characteristic, which is the collector current I_C versus the collector-emitter voltage V_{CE}, of an HBT having an emitter area of $2.5 \times 8\,\mu\mathrm{m}^2$. The measurement was carried out for base current
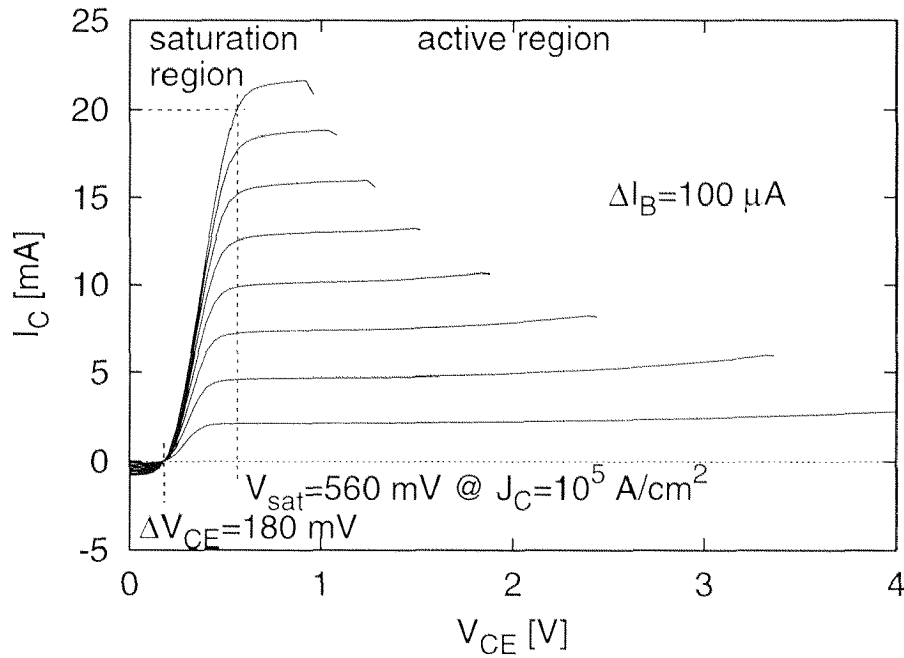
Figure 4.1: *Common emitter output characteristics of an HBT with an emitter area $A_E = 2.5 \times 8\,\mu m^2$*

steps of ΔI_B of $100\,\mu$A.

A key parameter of the transistor is the output conductance, which can be determined from the output characteristic. This parameter is related to the base thickness modulation due to the variation of the collector-emitter voltage V_{CE}. This causes an increased I_C with higher V_{CE}. As a conse-

quence, the curves in the active region have a certain slope which is characterized by the Early-voltage V_A. The output conductance g_o is then I_C/V_A. There are other effects e.g. self-heating and breakdown modifying the I_C vs. V_{CE} characteristics. The thermal effects cause that output conduction g_o extracted from the output characteristics is higher than the effective g_o, which is obtained when the device is operated at a constant collector-emitter voltage. Pulsed measurements with pulses shorter than the thermal time constant could be used to avoid thermal effects. However, the influence of these effects on the extrapolation of V_A can also be minimized if V_A is determined at a low current level. Typical values of $V_A \simeq 55 \pm 10$ V were found at $I_B = 100 \, \mu$A for a wafer with a base thickness X_B of 75 nm and 20 ± 5 V for $X_B = 50$ nm. The resulting output resistance $r_o = 1/g_o$ varies from 55 kΩ to 2.2 kΩ and from 20 kΩ to 1 kΩ for $X_B = 75$ nm and $X_B = 50$ nm with a variation of the collector current from 1 mA to 20 mA.

The offset voltage ΔV_{CE}, which is the collector-emitter voltage where the collector current starts to be positive, is 180 mV. For other materials, e.g. InAlAs/InGaAs and AlGaAs/GaAs HBTs, values of 300 mV [45] were found. This difference could be expected due to the different conduction band offsets at the base-emitter heterojunction of 0.23 eV and 0.5 eV for InP/InGaAs and InAlAs/InGaAs [46] junctions, respectively. The saturation or knee voltage is $V_{sat} = 560$ mV at $J_C = 10^5$ A/cm^2. The saturation voltage is relevant in switching transistors because saturation effects lead to slower switching times.

Figure 4.2 shows the breakdown characteristics of our HBTs which is another important figure of merit. The breakdown voltage at zero collector current is $BV_{CE0} = 8.9$ V for an HBT with an emitter area $A_E = 2.5 \times 8 \, \mu$m^2 and a collector thickness of 400 nm. This measurement was carried out with an open base terminal leading to $I_B = 0$. For a thicker collector of 800 nm, BV_{CE0} increases to 17 V. The breakdown voltages at elevated current levels are considerably reduced due to self-heating. As a consequence, the devices can only operate up to collector-emitter bias voltages of about 2 V at a collector current densities of $J_C = 10^5$ A/cm^2.

4.1.2 Gummel-Plot

The Gummel-plot is used for the investigation of the injection behavior of the base-emitter junction in forward operation. Although the injection behavior of a heterojunction is different to a homojunction, the behavior can
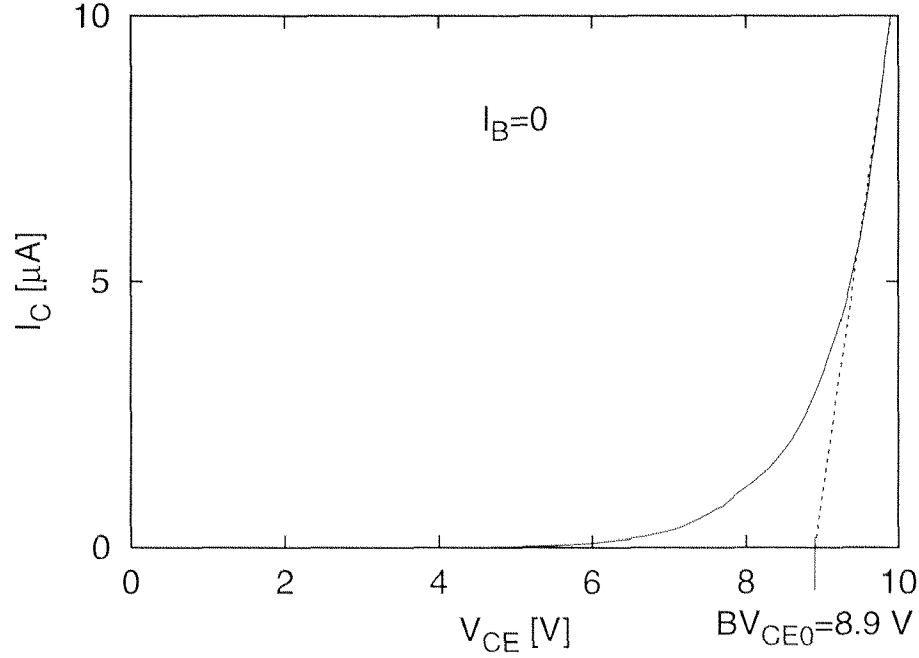
Figure 4.2: *Breakdown characteristics of an HBT with an emitter area* $A_E = 2.5 \times 8\,\mu m^2$ *and a collector thickness of 400 nm at* $I_B = 0$

be similarly described by [47, 36]

$$I_C \simeq I_S \left[\exp\left(\frac{V_{BE}}{n_F V_T} \right) - 1 \right] \tag{4.1}$$

$$I_B \simeq \frac{I_S}{BF} \left[\exp\left(\frac{V_{BE}}{n_B V_T} \right) - 1 \right] + I_{SE} \left[\exp\left(\frac{V_{BE}}{n_E V_T} \right) - 1 \right] \tag{4.2}$$

where V_T is the thermal voltage kT/q, I_S, the saturation current, BF, the large-signal forward current gain, I_{SE} denotes the low-current leakage saturation current, n_F, n_B, and n_E are the emission coefficients of the collector, base, and base-emitter leakage currents, respectively. Generally, the emission coefficients are current dependent for heterojunctions. This dependence can be neglected for base-emitter voltages $V_{BE} \gg kT/q$, which is fulfilled for the bias points of interest [48].

In order to more easily determine the parameters of Eqs. (4.1) and (4.2), the currents are plotted in logarithmic scale in the Gummel-plot which is depicted in Figure 4.3.

Two important parameters which are extrapolated from the Gummel-plot are the small- and large-signal current gains β ($= dI_C/dI_B$) and BF (I_C/I_B), respectively. Figure 4.4 shows the two current gains vs. collector current I_C. The low current gain in the low-current region ($I_B < 10\,\text{nA}$)
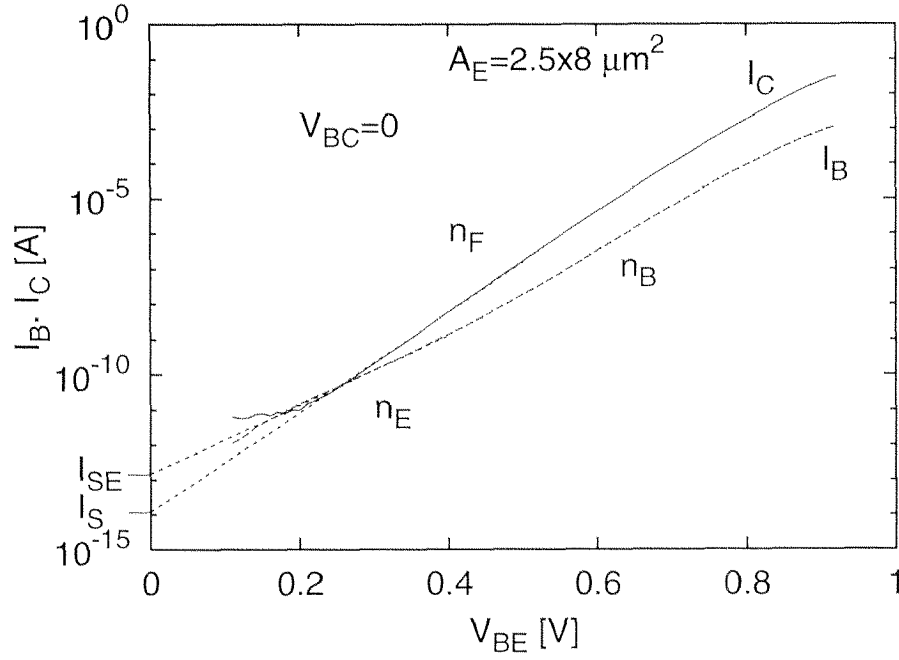
Figure 4.3: *Gummel-plot of an HBT with an emitter area of* $2.5 \times 8\ \mu m^2$
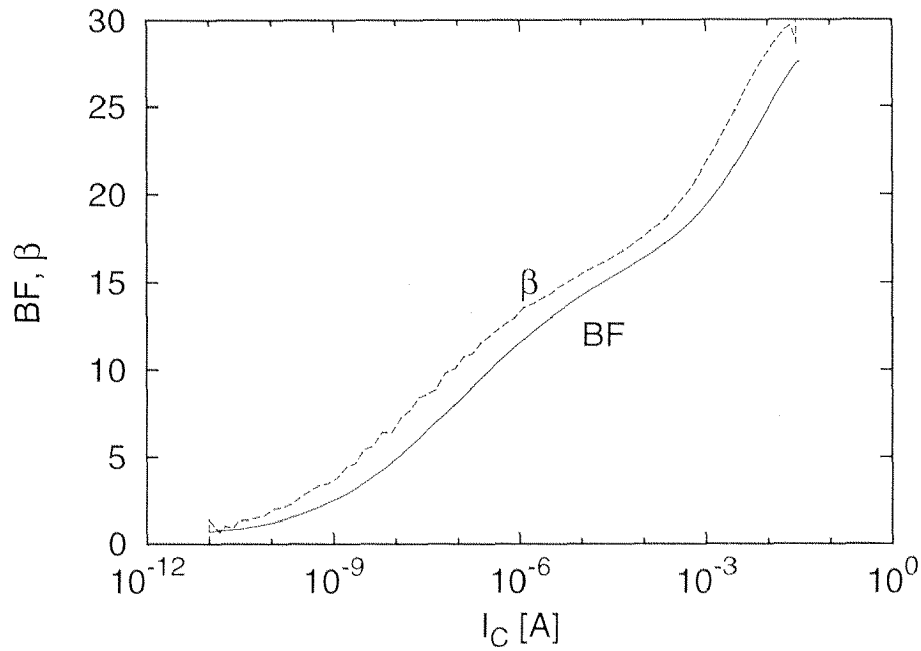
Figure 4.4: *Current gain vs.* I_C *of an HBT with a base thickness of 75 nm having an emitter area* A_E *of* $2.5 \times 8\ \mu m^2$

is a consequence of the base current I_B being dominated by base-emitter leakage or recombination currents. For large currents, the current gains increase with increasing I_C. In contrast to a homojunction bipolar transistor

(BJT), the currents gains do not reach a constant value because of the different emission coefficients of the base ($n_B = 1.55$) and collector ($n_F = 1.29$) currents. The different emission coefficients n_B and n_F are caused by portions of recombination currents in the base current which lead to an increase of the emission coefficient. These recombinations centers cannot be exactly located. Recombination in the spacer layer or at the surface are the most probable origins leading to a modification of n_B.

The maximum small- and large-signal current gains for an HBT having a base thickness of 75 nm and an emitter area of $2.5 \times 8 \ \mu m^2$ were measured to be $\beta = 30$ and $BF = 25$, respectively. The difference in the small- and large-signal current gain can be explained by the different emission coefficients of the base and collector currents, where $\beta \simeq n_B / n_F \cdot BF$. Devices with the same emitter area but a thinner base (50 nm) achieved β-values of 58. Due to surface recombination effects, the small-signal current gain β strongly depends on the emitter width W_E as depicted in Figure 4.5.
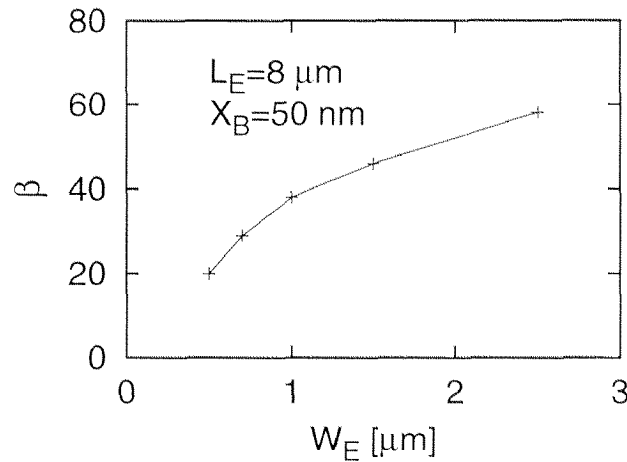
Figure 4.5: *Small-signal current gain β as a function of emitter width W_E for devices with a base thickness of 50 nm and an emitter length L_E of 8 μm*

The high-current region could not be measured due to thermal destruction of the devices. Therefore, the decrease in the current gains due to high-current effects cannot be shown. The destruction of the device could be avoided with pulsed measurements. Nevertheless, a flattening of the I_B and I_C curves at higher current levels can be observed in Figure 4.3. This is a consequence of the voltage drop over the base and emitter series resistors.

In addition to the emission coefficients, the saturation current I_S describes the transfer characteristic of the transistor in the forward active region. In contrast to the emission coefficients, which do not scale with de-
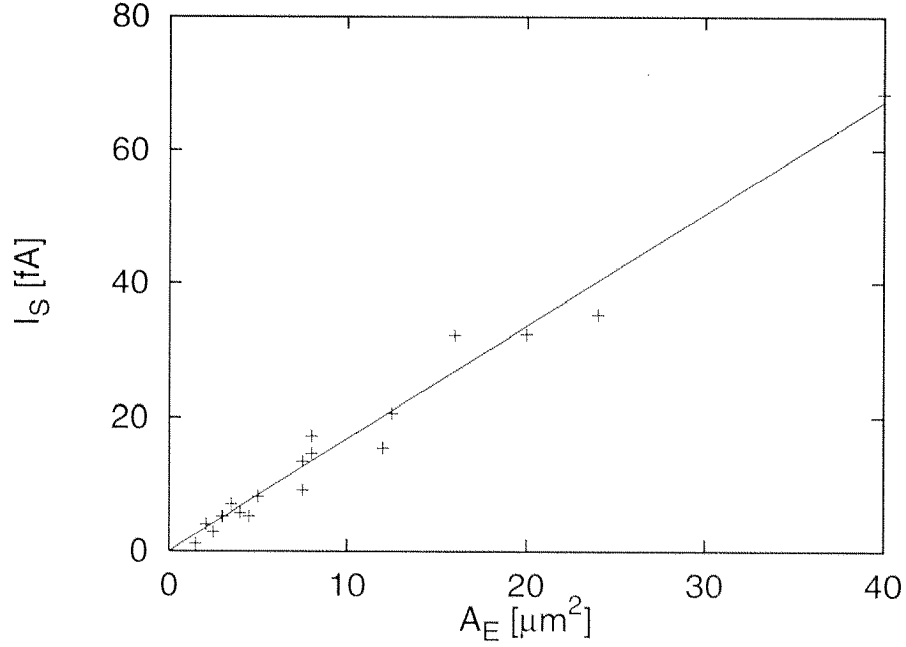
Figure 4.6: *Saturation current I_S vs. emitter-area A_E*

vice geometry, the saturation current I_S is proportional to the emitter area (Fig. 4.6) which corresponds very well with the theory [38].

As already mentioned, the small current region is dominated by leakage or recombination currents. Two parameters, the low-current leakage saturation current I_{SE} and the low-current base-emitter leakage emission coefficient n_E, are needed to characterize the device at low current level. The values for I_{SE} and n_E of the $2.5 \times 8\,\mu m^2$ device (Fig. 4.3) are 124 fA and 1.80, respectively. These two parameters also depend on device geometry which is shown in the Figures 4.7 and 4.8. The two parameters I_{SE} and n_E are plotted as a function the emitter length L_E for emitter widths ranging from 0.5 to $2.5\,\mu m$. No significant dependence upon emitter width can be observed. However, I_{SE} and n_E are functions of L_E. I_{SE} shows a $\propto L_E^{3.4}$ dependence upon L_E, whereas the emission coefficient n_E is a linear function of L_E.
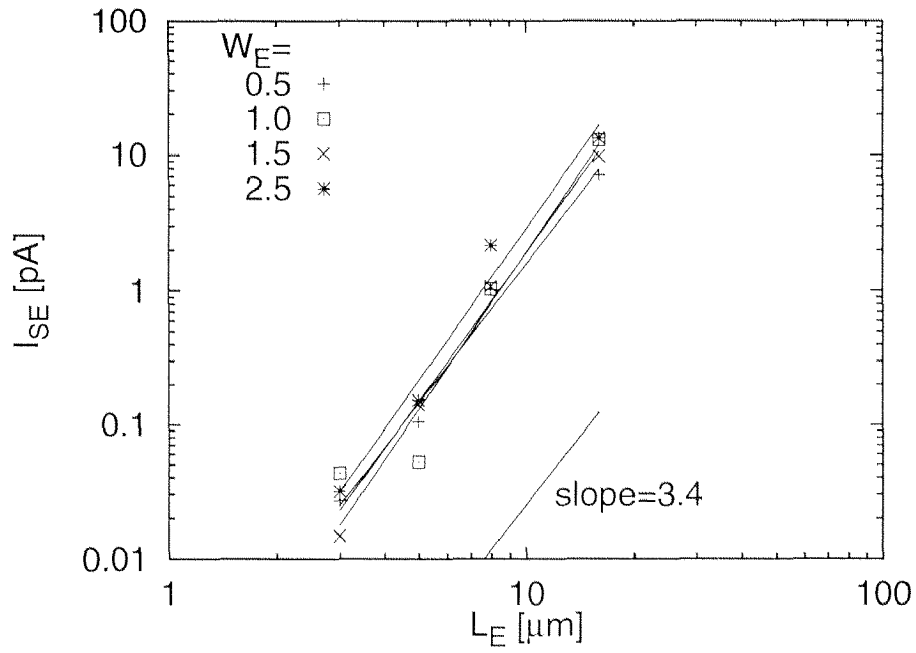
Figure 4.7: *Low-current leakage saturation current I_{SE} as a function of emitter length L_E*
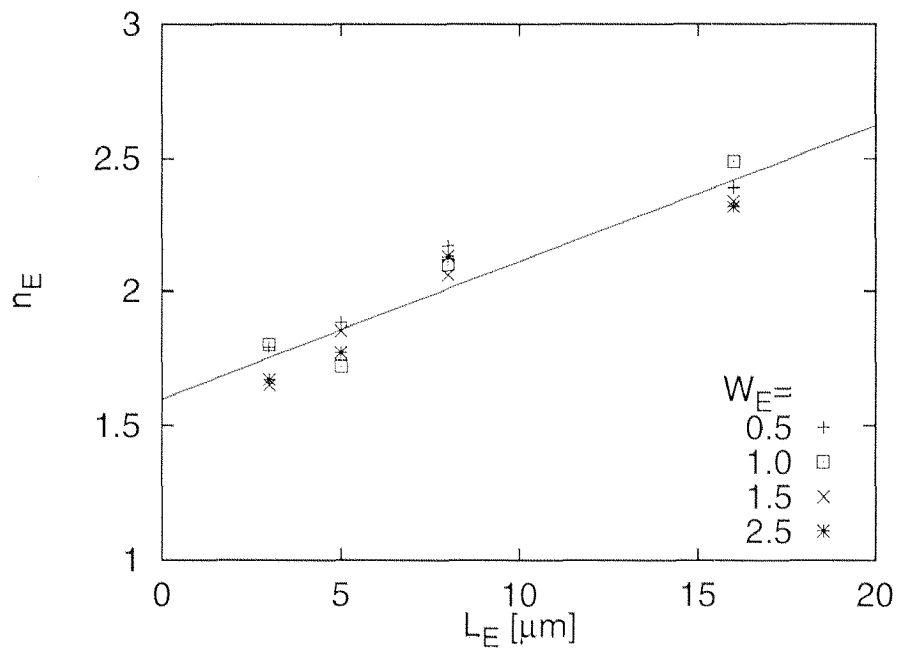
Figure 4.8: *Low-current base-emitter leakage emission coefficient N_E vs. emitter length L_E*

4.2 High-Frequency Characteristics

The HBTs were characterized in the RF range on the basis of on-wafer S-parameter measurements from 45 MHz up to 40 GHz (Wiltron 37269A) and 120 GHz (HP 8510C), respectively. Care had to be taken in order to operate the transistor in its linear region. This means that the input voltage swing should be so low that the exponential characteristic of the base-emitter diode could be approximated linearly. This is obtained when the peak-to-peak voltage swing is smaller than the thermal voltage $V_T = kT/q$. Therefore, the input power must be lower than −35 dBm.

Figure 4.9 shows the S-Parameters of an HBT having an emitter area of $2.5 \times 8\,\mu m^2$ which was operated at a collector current of 12.2 mA in the frequency range from 45 MHz to 40 GHz. These S-parameter data were cor-
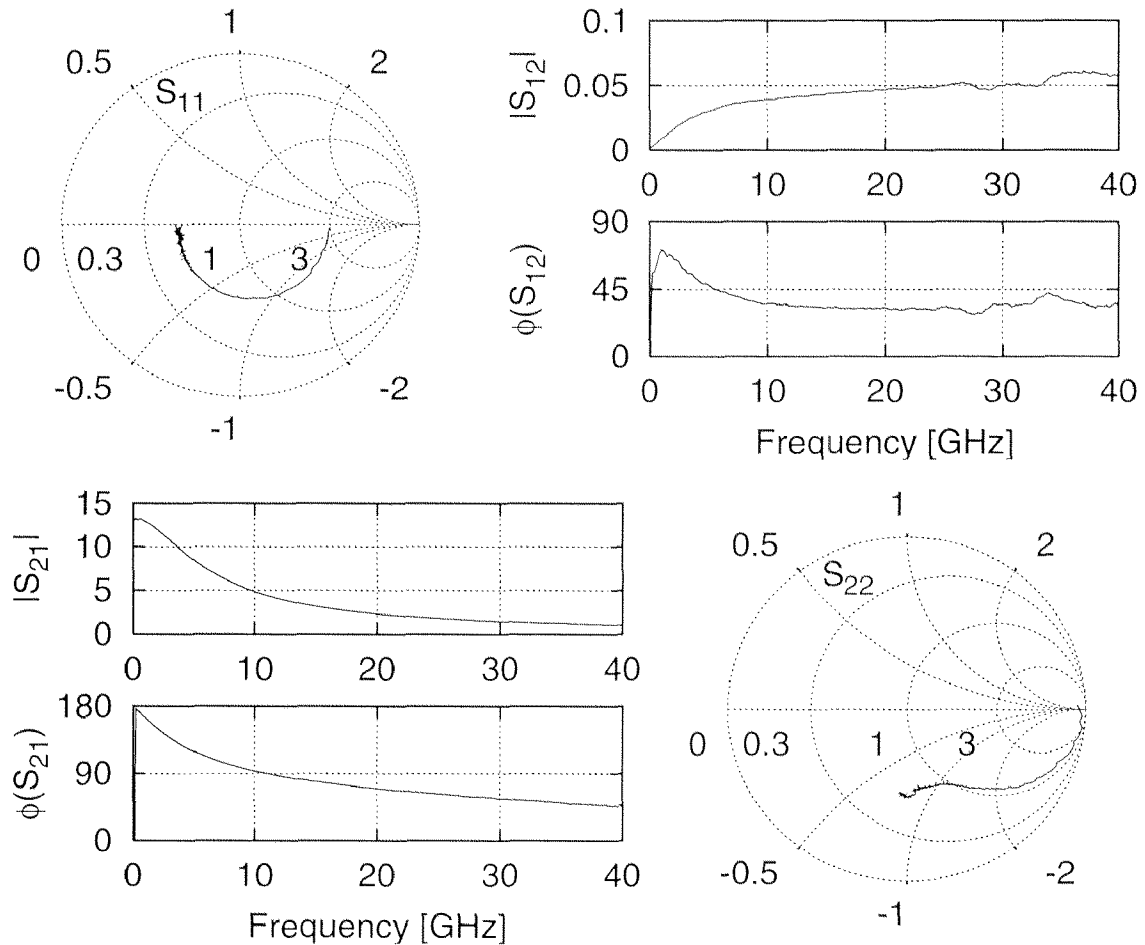
Figure 4.9: *S-parameters of an HBT (wafer W_2) with an emitter area $A_E = 2.5 \times 8\mu m^2$ at a collector current $I_C = 12.2\,mA$ and a collector-emitter voltage $V_{CE} = 1.5\,V$, frequency range: 0.045 ... 40 GHz*

rected using a de-embedding procedure (Appendix B.1) in order to eliminate the influences of the pads. To carry out the de-embedding, the S-parameters of open and short structures had to be measured before.

The high-frequency characteristics of a transistor are usually described by the transit frequency f_T and the maximum oscillation frequency f_{max}. In order to determine these parameters, the small-signal current gain h_{21}, Mason's unilateral power gain MUG [49], and the maximum available power gain MAG are plotted versus frequency, as shown in Figure 4.10 for an HBT with an emitter area of $1.0 \times 8 \, \mu m^2$. Cut-off frequencies, for devices on wa-
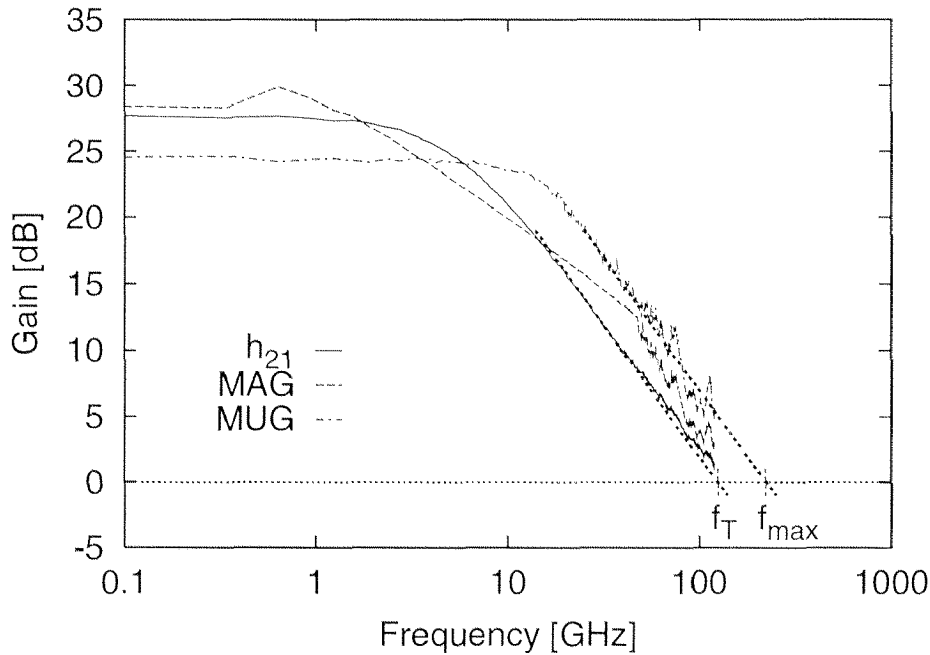
Figure 4.10: *Maximum available gain (MAG), Mason's unilateral gain (MUG), and small-signal current gain (h_{21}) of an HBT (wafer W_3) having an emitter area of $1.0 \times 8 \, \mu m^2$ at a collector current $I_C = 10.8 \, mA$*

fer W_3, f_T and f_{max} of $130 \, GHz$ and $220 \, GHz$ are obtained at a collector current $I_C = 10.8 \, mA$ and a collector-emitter voltage $V_{CE} = 2.0 \, V$. These are the highest f_T and f_{max} values reached with our InP-SHBTs. The cut-off frequencies are commonly extrapolated from $-20 \, dB/dec$ roll-offs of the gain curves. Therefore, the Mason's unilateral gain MUG is well suited to determine f_{max} because the maximum available gain MAG does not show a $-20 \, dB/dec$ roll-off. Theoretically, both gains, MUG and MAG, should have the same intercept point with the 0 dB line.

The cut-off frequencies are a function of the collector current I_C. In Figure 4.11, f_T and f_{max} are depicted as a function of the collector current

for an HBT with an emitter area of $2.5 \times 8 \mu m^2$ fabricated on three different wafers having the vertical layer structures presented in Table 4.1. A sig-
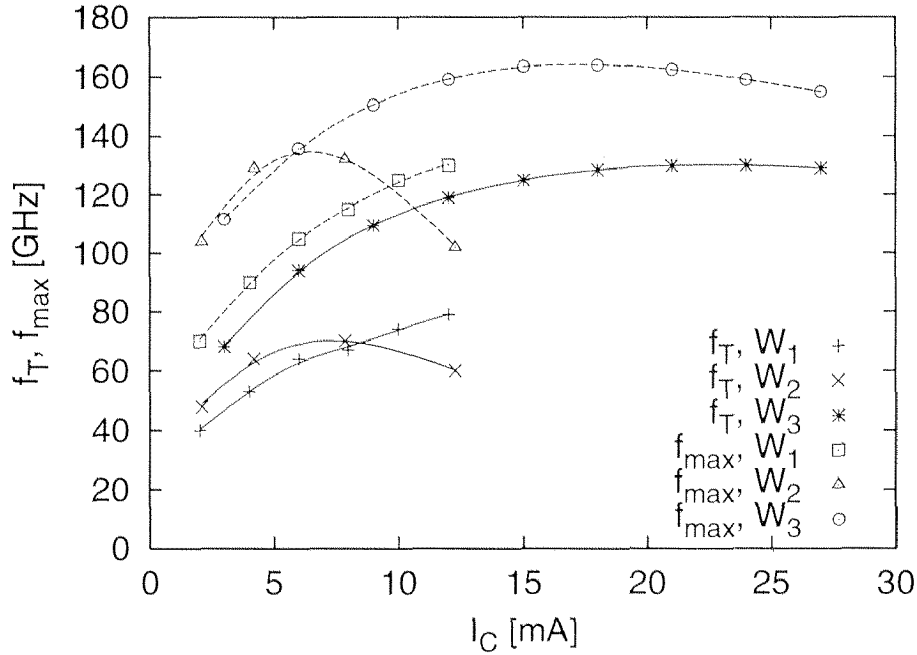
Figure 4.11: f_T and f_{max} versus I_C for three different layer structures $W_1 \ldots W_3$ (Table 4.1), device size: $A_E = 2.5 \times 8 \, \mu m^2$

	W_1	W_2	W_3
X_B [nm]	80	75	50
X_C [nm]	600	800	400

Table 4.1: *Base and collector thicknesses of the layer structures used in the experiments*

nificant influence of the collector current I_C and the layer structure can be observed. The dependence of f_T upon I_C respectively emitter current I_E is given by the following formula [50]

$$f_T = \frac{1}{2\pi} \left[\frac{n_F kT}{q I_E} C_{BE} + \left(R_E + R_C + \frac{n_F kT}{q I_E} \right) C_{BC} + \tau_B + \tau_C \right]^{-1}$$

$$(4.3)$$

where n_F is the ideality factor of the collector current, R_E and R_C are the series resistances of the emitter and collector, respectively, C_{BE} and C_{BC} denote the base-emitter and base-collector depletion capacitances, and

τ_B and τ_C are the base and collector delays. From Eq. (4.3), it becomes obvious that f_T increases with I_E and therefore with I_C as well. At higher I_C, both f_T and f_{max} decrease due to base push-out [51]. This decrease starts at smaller I_C for wider collectors because the critical current (Eq. (3.4)) is reduced with larger collector thicknesses X_C.

The layer structure, especially the thicknesses of the base and collector layers, significantly influence the RF performance of the HBT. A thinner base and collector reduces the base and collector transit times τ_B and τ_C, respectively, resulting in higher f_T (Eq. (4.3)) values. The comparison of the f_T values of the wafers W_1 and W_2 demonstrates the influence of the collector thickness X_C because they have almost the same base width. As expected, the HBTs on wafer W_1 with the thinner collector has a higher f_T than the devices on wafer W_2. A further reduction of the base and collector thicknesses (wafer W_3) leads to an additional increase of f_T, whereas the base-collector capacitance C_{BC} is also increased by the reduction of the collector thickness. Since C_{BC} is much smaller than the base-emitter capacitance C_{BE}, the increase in C_{BC} does not significantly affect f_T but is much more relevant for f_{max}. The relation of f_{max} and the transit frequency f_T, the base resistance R_B, and the base-collector capacitance c_{BC} is given by [52, 53]

$$f_{max} = \sqrt{\frac{f_T}{8\pi R_B C_{BC}}} \qquad (4.4)$$

The maximum oscillation frequency f_{max} is much more affected by parasitics than f_T which results in a different dependence upon the layer structure. This is a consequence of the influence of the base-collector capacitance C_{BC} which increases with decreasing collector thickness. The larger C_{BC} can then compensate for a shorter transit time when reducing the collector thickness which can be observed by comparing W_1 and W_2.

f_{max} also depends stronger on the emitter geometry than f_T because R_B and C_{BC} are functions of the emitter width and length. A larger emitter width increases both, r_B and C_{BC}, which affects f_{max} adversely. A longer emitter, however, enlarges the base-collector capacitance C_{BC} but reduces the base series resistance R_B and therefore the emitter length should, in first approximation, not significantly influence f_{max} very much.

From Eq. 4.4, f_{max} should show a similar current dependence than f_T, which can be observed in Figure 4.11.

The previous comments on f_T and f_{max} only explain Eqs. (4.3) and (4.4) qualitatively. In Section 5.3, the quantitative verification will be given.

4.3 Low-Frequency Noise Characteristics

Low-frequency noise becomes important in broadband applications which should operate from DC or in oscillators where the noise is converted up to the oscillation frequency. Therefore, the low-frequency noise behavior of our InP/InGaAs HBTs was measured and characterized in the frequency range from 0.2 Hz to 500 kHz. To find out where the noise sources are located and which of these sources dominate, it is necessary that the dependences of the noise behavior on bias point, transistor geometry, and temperature are known additionally to the frequency dependence.

4.3.1 Measurement Setup

The low-frequency noise was also measured on-wafer. The setup for these measurements is depicted in Figure 4.12. The supply voltage for the base
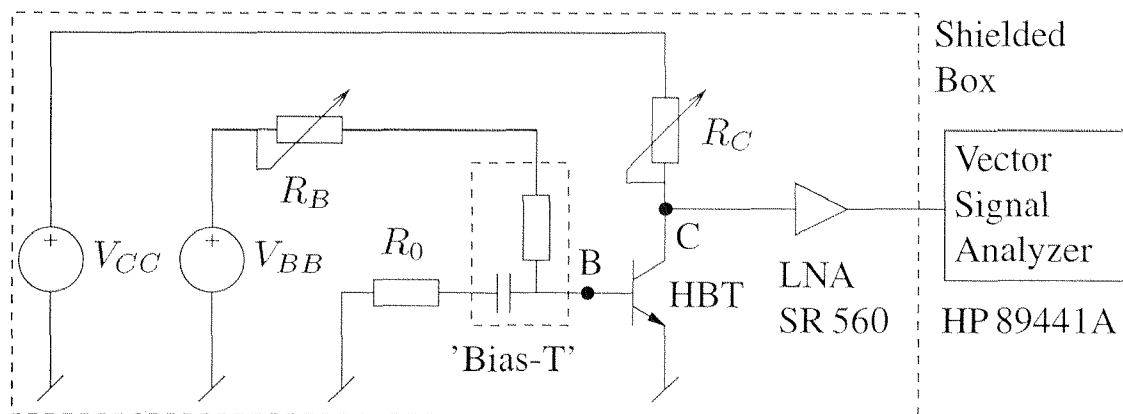
Figure 4.12: *Setup for low-frequency noise measurements*

and collector are generated by batteries because they introduce much less noise than other power supplies. The bias point of the transistor can be adjusted using potentiometer and controlled by multi-meters. These multi-meters have to be disconnected during measurement because they add too much noise. Since we have the same oscillation problem as described in Chapter 4.1, the base had to be terminated with a 50 Ω resistor using a bias-tee. We constructed this bias-tee with a resistive DC-feed. By choosing appropriate values for the resistor and capacitor of the bias-tee, it was possible that the bias-tee did not modify the frequency characteristic of the measured LF-noise data which facilitated the evaluation of the measurement results. In the analysis of the data, the noise of all the resistors in the setup had to be taken into account.

For the measurement of the output noise voltage, we connected the collector of the HBT to a low-noise amplifier (SR 560), which has an equivalent input noise voltage of $4\,nV/\sqrt{Hz}$. This value is more than a magnitude smaller than the measured output noise voltage of the transistor and does therefore not modify the results. The output signal of the amplifier was visualized using a vector signal analyzer (HP 89441A). In oder to obtain the noise at the base, the measured collector noise voltage was transformed according to the formula derived in Appendix B.2.

The DC probe station, together with the whole measurement setup without the vector signal analyzer, was placed in a shielded box. Otherwise, signals in the air or in power supply cables (e.g. 50 Hz signal) would enormously disturb the measurements.

4.3.2 Frequency-Dependence

Figure 4.13 represents the power spectral density of the base noise current for an HBT with an emitter area of $2.5 \times 8\,\mu m^2$ in the frequency range from 5 Hz to 500 kHz. At a base current of 620 μA, a power spectral noise density
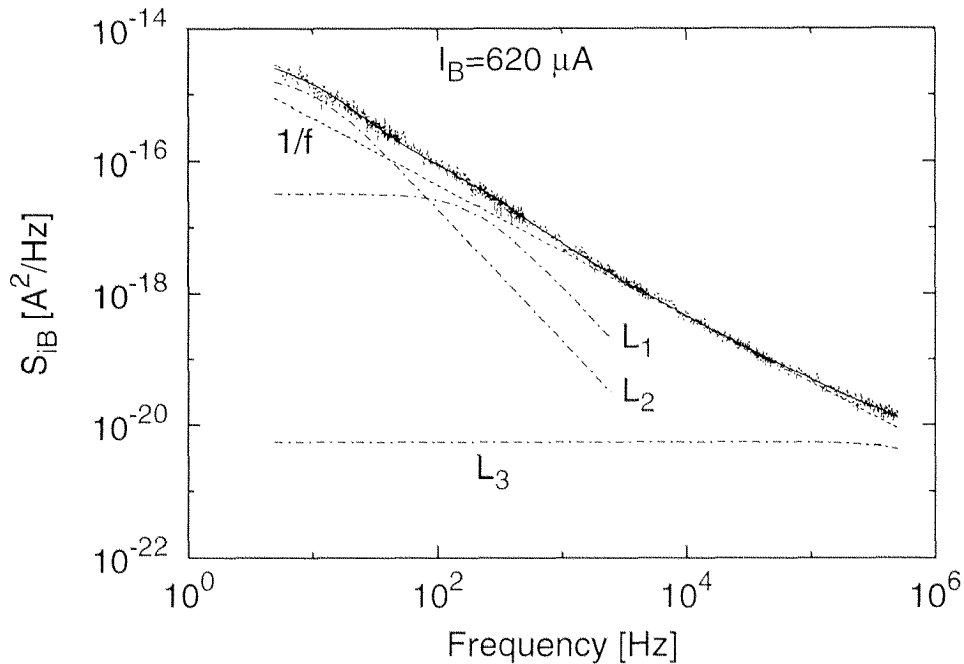
Figure 4.13: *Power spectral density of the low-frequency noise for an HBT with $2.5 \times 8\,\mu m^2$ at a base current of 620 μA in the frequency range from 5 Hz to 500 kHz*

S_{iB} of $1 \cdot 10^{16}$ A^2/Hz is measured at 100 Hz. Some InP HBTs [27, 54] show

a comparable low-frequency noise level but in general, their noise level is lower [13, 55]. The measured noise level is more typical for AlGaAs/GaAs devices [14, 56].

The investigation of the frequency dependence of the low-frequency noise helps to identify which noise phenomena dominates. This is possible because different noise phenomena show different spectral noise densities. We therefore fitted the power spectral current density of the low-frequency noise of the base current to an expression consisting of a $1/f$-part ($S_{1/f}$), a sum of Lorentzian type spectra (L_i), which are typical for generation-recombination noise (Sec. 2.2.4), and a component showing white noise.

$$S_{iB,LF} = S_{1/f} + \sum_{i=1}^{3} L_i + S_{white}$$

$$= \underbrace{\frac{B_0}{f}}_{S_{1/f}} + \underbrace{\sum_{i=1}^{3} \frac{B_i}{f_{0,i}} \frac{1}{1 + \left(\frac{f}{f_{0,i}}\right)^2}}_{S_{GR}} + S_{white} \qquad (4.5)$$

Eq. (4.5) is often used for the characterization of low-frequency noise [17] and already found to be well suited for InP/InGaAs HBTs [28]. Up to 500 kHz, the white noise S_{white} is approximately 2 decades smaller than the other noise components and can therefore be neglected here.

From the fitting procedure for the curve in Fig. 4.13, which was measured for an HBT with an emitter area of $2.5 \times 8\,\mu m^2$ operated at $I_B = 620\,\mu A$ and at a temperature of 20 °C, the values of the parameters B_0, B_i, f_{oi} presented in Table 4.2 were obtained. These parameters (B_0, B_i, f_{oi})

	$S_{1/f}$	L_1	L_2	L_3
B_i [A^2]	$4.4 \cdot 10^{-15}$	$1.9 \cdot 10^{-14}$	$6.5 \cdot 10^{-15}$	$5.4 \cdot 10^{-15}$
f_0 [Hz]	-	10	100	10^6

Table 4.2: *Amplitude B_0 of the $1/f$ component and amplitudes (B_1 and B_2) and corner frequencies of the Lorentzian spectra of an HBT with $A_E = 2.5 \times 8\,\mu m^2$ at $I_B = 620\,\mu A$*

are not constant but are functions of bias point, emitter geometry, and temperature, which is described in Sections 4.3.3, 4.3.4, and 4.3.5, respectively. The Lorentz spectrum L_3 is not considered further because of the fact that for certain bias points and transistors, the corner frequency was outside the measurement range.

When we extrapolate the low-frequency noise toward higher frequencies, we obtain the $1/f$ corner frequency f_c at the cross-point with the white noise floor. Due to the high low-frequency noise level, also high values of f_c between 1 and 10 MHz are found.

4.3.3   Bias-Dependence

Because the low-frequency (LF) noise consists of different noise contributions such as $1/f$ part $S_{1/f}$ and generation-recombination S_{GR} parts, the bias-point dependence of all these components has to be investigated. The base current I_B dominantly determines the LF-noise. Therefore, Figure 4.14 shows the LF-noise components as a function of I_B. The different
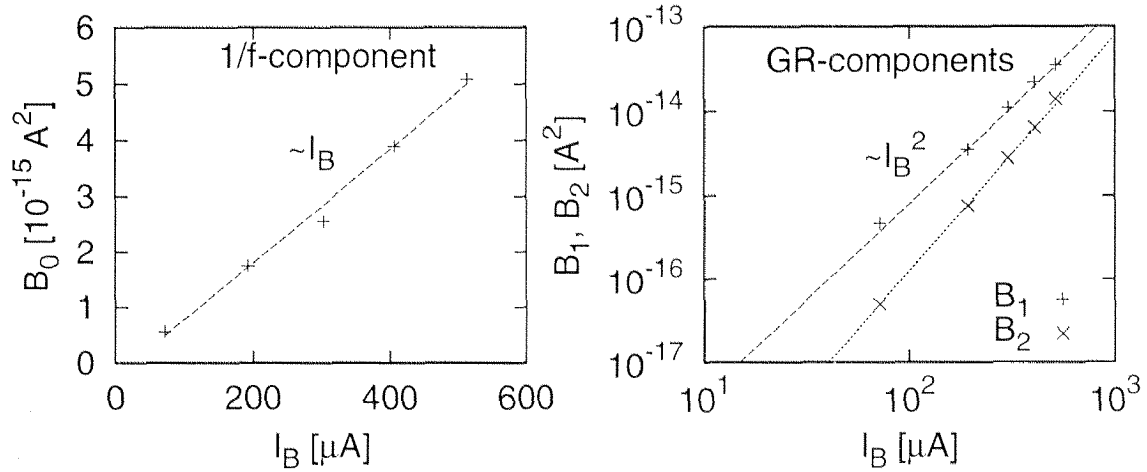
Figure 4.14: $1/f$ *component* (B_0) *and generation-recombination components* $(B_1$ *and* $B_2)$ *of the LF-noise versus base current* I_B*; emitter area* $A_E = 1.5 \times 8\,\mu m^2$

noise contributions show different I_B dependences.

The $1/f$ part (B_0) depends linearly on the base current. This behavior is typical for noise which is associated with fluctuations in the diffusion constant [30] or minority carrier trapping [57]. Hence, it can be stated that $S_{1/f}$ in our HBTs should not result from recombination of the carriers at the base surface or along the surface of the emitter-base space charge region. Otherwise, a quadratic I_B dependence would be observed (Eq. (2.43)).

The dependences of the noise components of the Lorentzian spectra of Eq. (4.5) are also depicted in Figure 4.14. These components start to contribute to the low-frequency noise when the values of B_1 and B_2 exceed the

value of B_0. The two parameters approximately show a quadratic current dependence which is typical for generation-recombination processes.

4.3.4 Geometry-Dependence

A method which is additionally used for the localization of the noise phenomena is the investigation of the influence of the geometry upon the noise power. Moreover, the geometry-dependence of the noise behavior can help to identify the noise phenomena incorporated in the total noise. Therefore, the $1/f$ and generation-recombination part of the low-frequency noise are plotted in Figure 4.15 vs. perimeter P_E to emitter area A_E ratio. In spite
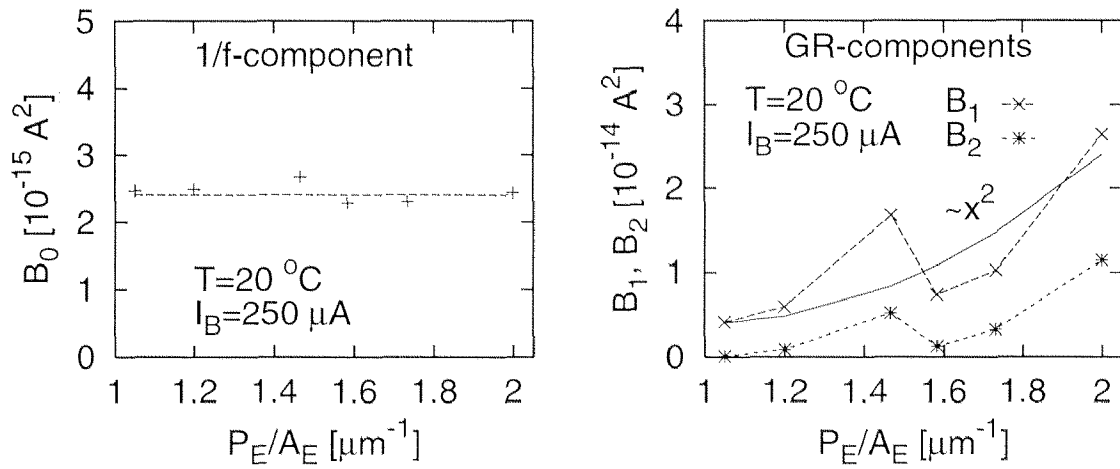
Figure 4.15: $1/f$ component (B_0) and generation-recombination components $(B_1$ and $B_2)$ of the LF-noise vs. emitter perimeter P_E to emitter area A_E ratio, base current $I_B = 250\,\mu A$, $T = 20\,^\circ C$

of the uncertainty of the measured data, quadratic dependence of the G-R-parts $(B_1$ and $B_0)$ P_E/A_E ratio is stated. Thus, the noise power can be approximated by

$$SI_{bs} \propto \left(\frac{P_E}{A_E}\right)^2 I_B^2 \qquad (4.6)$$

which is typical for extrinsic base surface recombination [13] for the following reasons. We can assume that the surface recombination current I_{bs} is proportional to the perimeter length P_E. The noise power SI_{bs} due to this recombination current is proportional to I_{bs}^2 [58]. If SI_{bs} is expressed by the base current I_B $(I_B \propto A_E)$, Eq.(4.6) is obtained.

We can observe that the $1/f$-noise part is independent of the P_E/A_E ratio. Hence, the $1/f$ noise portion should not result from surface recombination and is more likely associated with bulk effects (2.2.5). This was already found from the linear base current dependence (Section 4.3.3).

4.3.5   Temperature-Dependence

For the investigation of the temperature dependence of the low-frequency noise, the substrate was heated by placing the wafer on a Peltier element. To control the temperature, a temperature controlled LDT 5910B was used. Figure 4.16 shows the low-frequency noise components vs. substrate temperature. A $1/f$ noise component, which is insensitive to temperature vari-
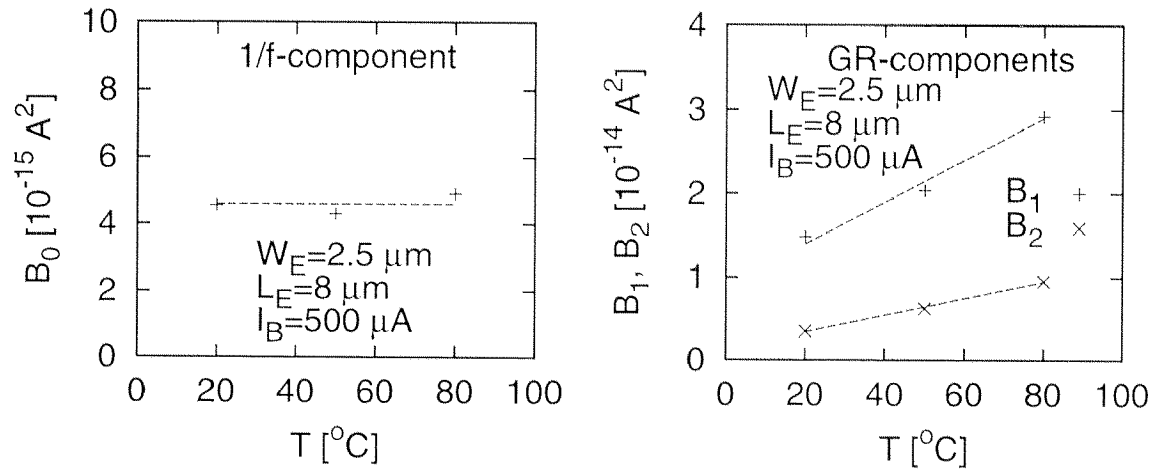
Figure 4.16: $1/f$ component (B_0) and generation-recombination components (B_1 and B_2) of the LF-noise versus temperature; $I_B = 500\,\mu A$, $A_E = 2.5 \times 8\,\mu m^2$

ations, is observed. This behavior was already found by Costa et al. [43]. The G-R-parts approximately increases linearly with temperature which can be explained by a higher recombination rate at elevated temperatures.

4.3.6   Long-Term Measurements

The long-term measurements of the $1/f$ noise are used to investigate the burn-in behavior of our HBTs. Furthermore, the results may give information on the reliability of the devices [14]. Figure 4.17 shows the base current as a function of time and the $1/f$-noise components for these base currents. The base current increases from about $40\,\mu A$ to $110\,\mu A$ and remains after
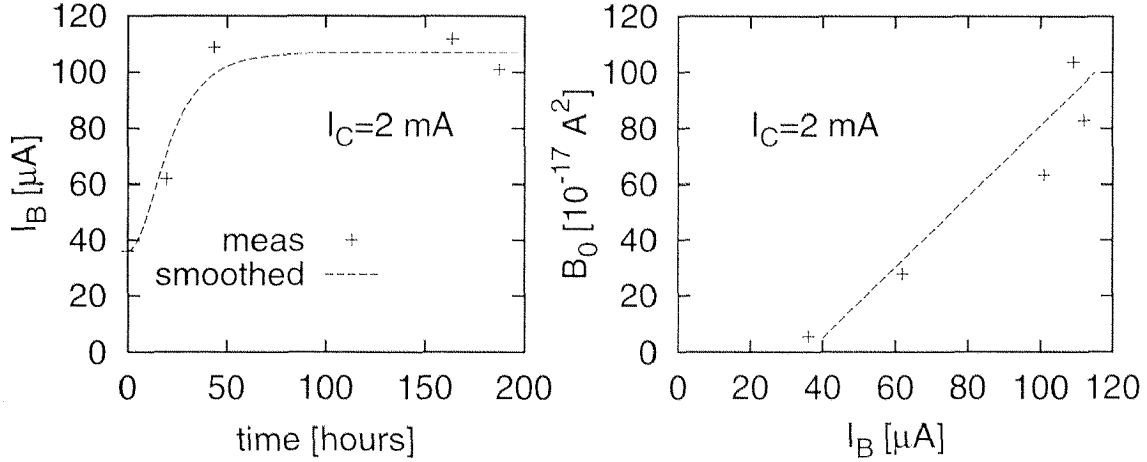
Figure 4.17: I_B *as a function of the operation time and* $1/f$ *components* (B_0) *versus* I_B

an operation time of 100 hours at this value. This equals a degradation in the large-signal current gain B of a factor of 2.5. The dependence of the $1/f$-noise upon I_B is linear during the time of measurements which was already observed in Section 4.3.3. Thus, the processes generating the $1/f$-noise do not change during burn-in.

4.4 High-Frequency Noise Characteristics

The noise generated by an electronic device at high frequencies is essential for the design of RF circuits, especially for amplifiers. The noise behavior of a two-port, and therefore of a transistor, can be described by the noise parameters F_{min}, R_n and Γ_{opt}, as already presented in Chapter 2.1. In this work, all these parameters were measured as a function of frequency, bias point, emitter geometry and temperature. After a short description of the measurement setup (Sec. 4.4.1), measurement data are presented in the Sections 4.4.2 to 4.4.5. These data are corrected for the influence of the pads as described in [59].

4.4.1 Measurement Setup

The high-frequency noise characterization of the HBT was carried out on-wafer in the frequency range from 2 to 26 GHz using the Cascade noise parameter measurement system NPT 26 shown in Figure 4.18. The most
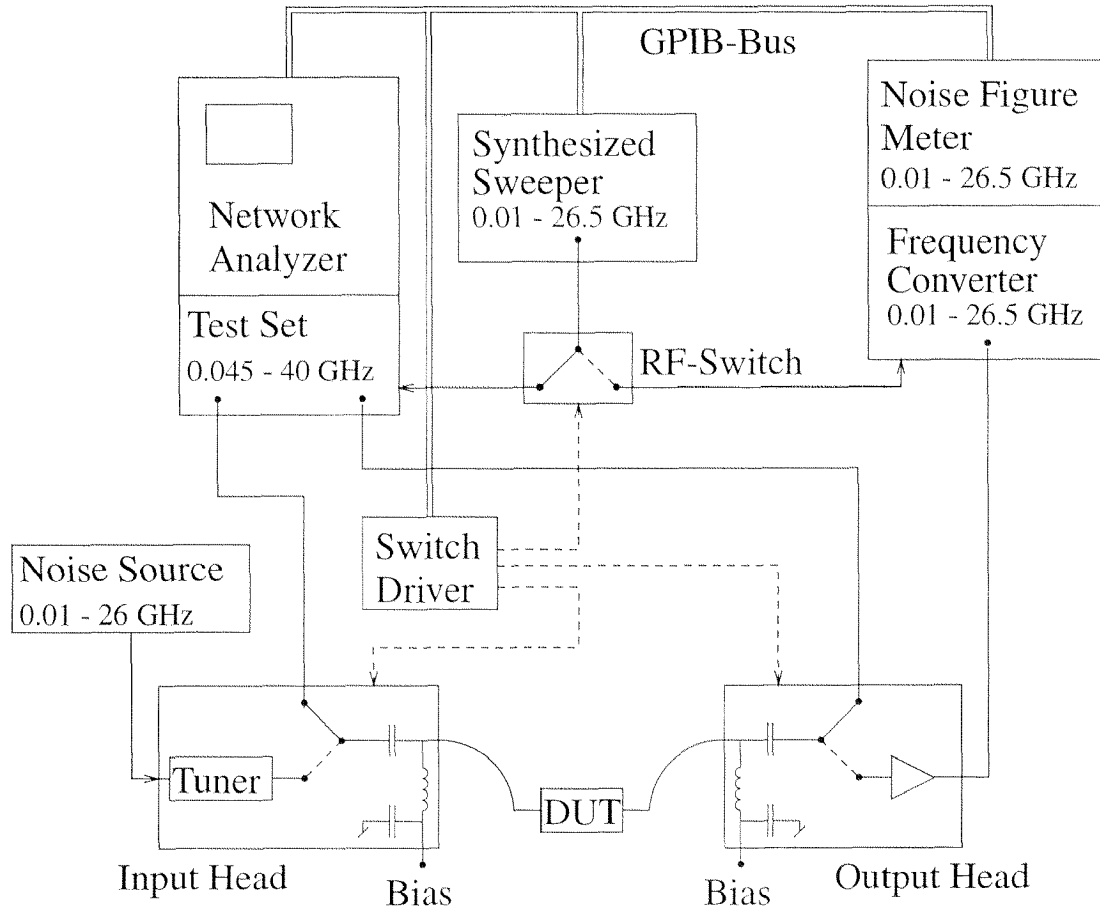
Figure 4.18: *Setup for high-frequency noise parameter measurements*

important components of this system are the input head with the tuners and an output head with a low-noise amplifier, a noise figure meter (HP 8970B), a noise source (HP 346B), and a network analyzer (HP 8510B). The part which limits the frequency range of measurements is the tuner (Fig. 4.19). The tuner generates the different source reflection factors which are neces-
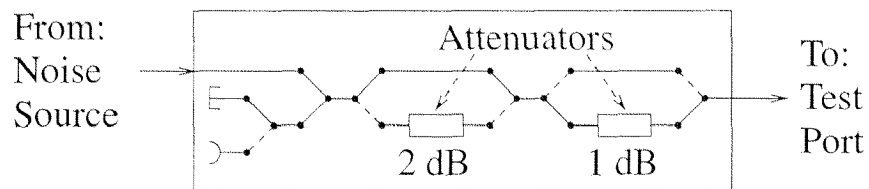
Figure 4.19: *Tuner for different source reflection factors*

sary for the noise parameter measurement. The measurement system determines the noise figure for each reflection factor. From these data, the minimum noise figure F_{min}, the corresponding optimum source reflection factor Γ_{opt}, and the equivalent noise resistance R_n can be calculated [60].

For an error-free calculation of noise parameters, it should be possible to set the attenuators of the tuner in a way that the reflection factors offered to the device-under-test are well distributed in the Smith-chart and cover a large area. This condition must be fulfilled for all frequency points. In the worst case, where the condition previously described is not fulfilled, all possible reflection factors are concentrated in one point in the Smith-chart. Thus, no F_{min} and Γ_{opt} can be calculated. Hence, the attenuators in the tuners should show similar values for all frequencies. This requirement is difficult to meet especially at higher frequencies where e.g. the connection between the tuner and the probe head introduces additional phase shift and loss which lead to a redistribution of the reflection factors and the worst case discussed above could occur. In the measurement equipment we used, the frequency range was therefore limited from 2 to 26 GHz, which is often too small for an accurate noise modeling of transistors with transit frequencies larger than 100 GHz (e.g. devices on wafer W_3, Table 4.1). Thus, the noise models for these devices, which are used for the design of the RF circuits operating up to 50 GHz, cannot be verified in the frequency range of interest. Hence, only noise models with extrapolated noise parameters can be used for the designs at these frequencies.

4.4.2 Frequency-Dependence

The room temperature frequency dependences of the minimum noise figures F_{min} for an HBT having an emitter area of $1.5 \times 8\,\mu m^2$ operated at a collector current of 7.2 mA are plotted in Figure 4.20 for different vertical layer structures. At microwave frequencies, the dominant noise sources in an HBT are the current noise from the base and collector currents and the thermal noise from the base series resistance. Because of the broadband nature of these noise sources, F_{min} remains constant over a very wide frequency range, as can be seen in Figure 4.20. At lower frequencies, F_{min} can approximately be expressed as [10]

$$F_{min}(f) \simeq 1 + \frac{1}{\beta(f)} \sqrt{\frac{2(R_B + R_E)qI_C}{n_F kT} + 1} \qquad (4.7)$$

From Eq. (4.7) we can see that F_{min} is increased with higher base and emitter series resistances (R_B and R_E) and collector current I_C but decreases with an increased small-signal current gain β. The smallest noise figure is observed for the HBT of wafer W_3. This is the wafer with the thinnest base resulting in the highest β value (Eq. (tech:eq:beta)) ($\beta = 18, 23, 52$ for W_1,
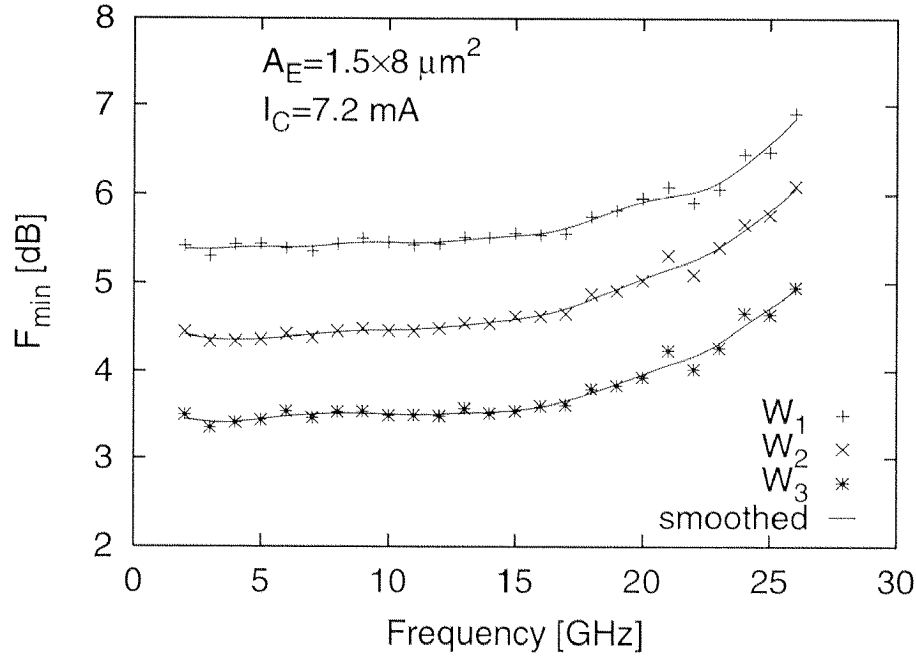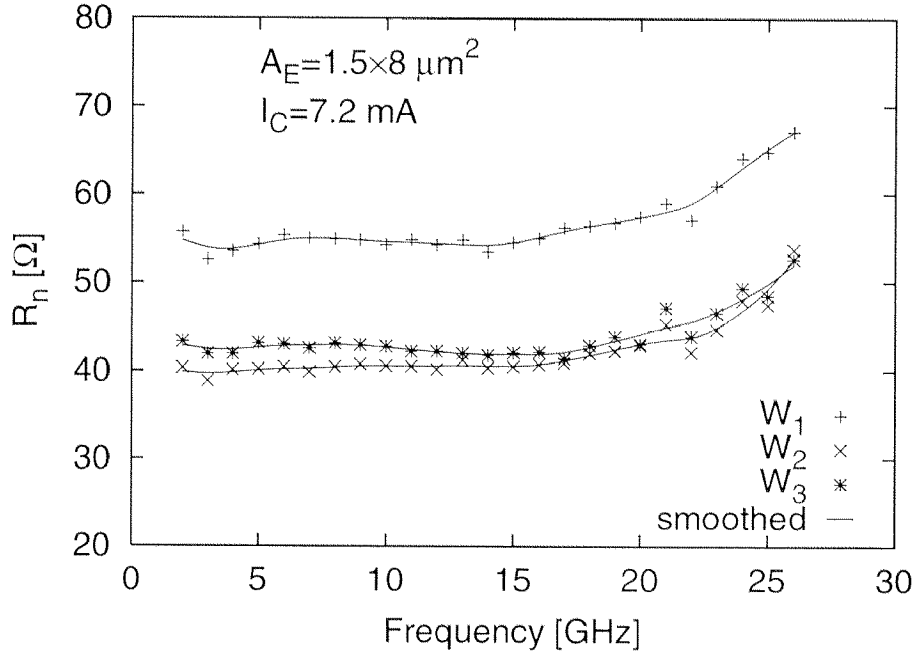
Figure 4.20: *Minimum noise figure F_{min} vs. frequency at $I_C = 7.2\,mA$ for three different layer structures $W_1 \ldots W_3$ (Table 4.1), device size: $A_E = 1.5 \times 8\,\mu m^2$*

W_2, W_3 (Table 4.1), respectively. As a consequence of the larger β, the base current noise of the transistor is reduced at a constant collector current. The voltage noise from the increased base resistance, which results as a consequence of the thinner base of W_1, is more than compensated by the decrease in the current noise. Thus, it is advantageous to design a transistor with a high current gain at a cost of a high base resistance. This statement is not valid for all collector currents. If the current is reduced, the thermal noise of the base resistance begins to dominate the current noise which makes the design strategy for the device contrary.

The minimum noise figure increases moderately at higher frequencies because the current gain is reduced. The corner frequency, where the F_{min} starts rising, is related to the 3 dB cut-off frequency of the current gain β.

The noise resistance R_n, which describes the increase of the noise figure if the source impedance does not equal the optimum value, is given by [10]

$$R_n(f) \simeq \frac{T}{T_0}(R_B + R_E) + \frac{n_C kT}{q I_C} \qquad (4.8)$$

where T_o is the ambient temperature. R_n should be equal for devices with the same emitter geometries operated at equivalent collector currents. This

is the case for the devices on wafer W_2 and W_3, as can be observed in Figure 4.21. The HBTs on wafer W_3 show a higher noise resistance than

Figure 4.21: *Noise resistance R_n vs. frequency at $I_C = 7.2\,mA$ for three different layer structures $W_1 \dots W_3$ (Table 4.1), device size: $A_E = 1.5 \times 8\,\mu m^2$*

the devices on the other two wafers. This can be caused by an elevated device temperature due to the thicker subcollector providing a worse heat sink.

The optimum source resistance R_{opt} and reactance X_{opt} are shown versus frequency in Figure 4.22. The variation of R_{opt} and X_{opt} in the frequency range of measurement is very small which simplifies broadband noise matching of our HBTs. The optimum source impedance Z_{opt} is, in first approximation, the ratio between voltage noise e_n^2 and current noise i_n^2 at the input of the transistor (see 2.1) and can be expressed as [10]

$$R_{opt}(f) \simeq \sqrt{\beta(f)\frac{n_C kT}{qI_C}2(R_B + R_E) + \frac{n_C kT}{qI_C}} \qquad (4.9)$$

$$X_{opt}(f) \simeq \omega\beta(f)C_{jE}\frac{n_C kT}{qI_C} \qquad (4.10)$$

Here we observe that the optimum real and imaginary parts of Z_{opt} are the same for the HBTs on wafer W_1 and W_2 because they have approximately
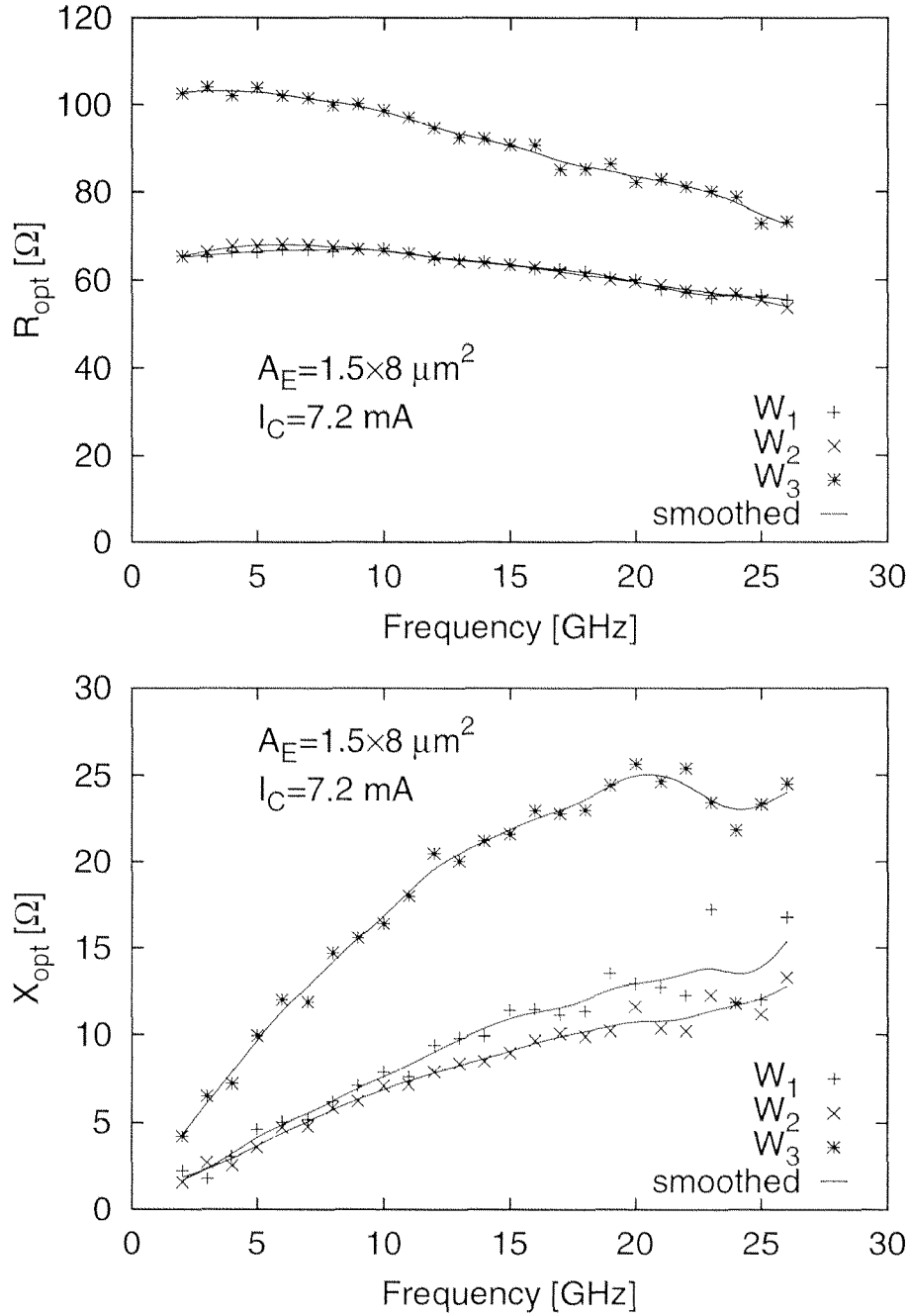
Figure 4.22: *Real and imaginary part, R_{opt} and X_{opt}, of the optimum source impedance Z_{opt} vs. frequency at $I_C = 7.2\,mA$ for three different layer structures $W_1 \ldots W_3$ (Table 4.1), device size: $A_E = 1.5 \times 8\,\mu m^2$*

the same base thickness which leads to similar current gains β and base resistances R_B. Wafer W_3 which has a thinner base, resulting in higher β and R_B values, exhibit larger values for R_{opt} and X_{opt}. This can render noise matching to $50\,\Omega$ more difficult, especially in broadband applications.

4.4.3 Bias-Dependence

For circuit design, the variation of the noise parameters as a function of bias point is an important issue. The small-signal and noise behavior of transistor is dominantly determined by the collector current I_C. Figure 4.23 shows F_{min} at 10 GHz as a function of I_C and J_C. Since the current noise
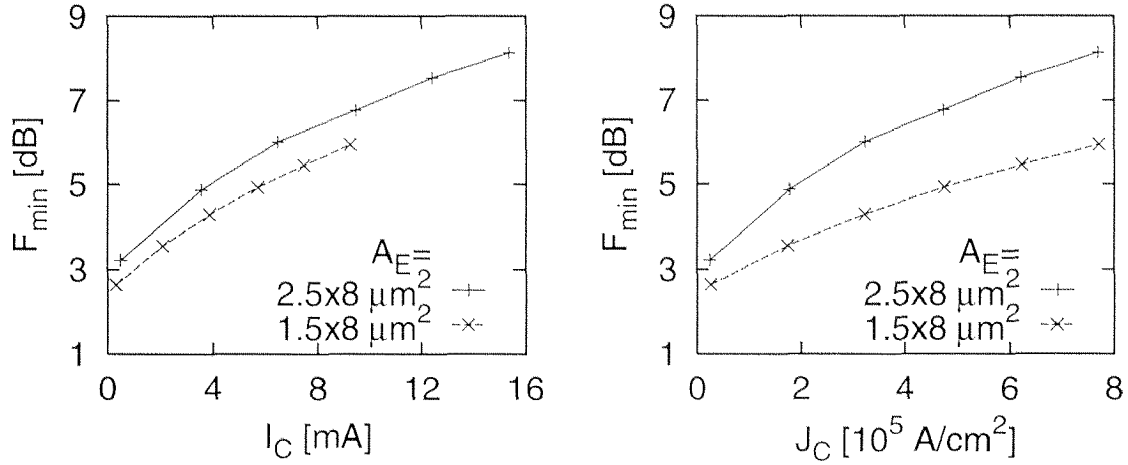
Figure 4.23: *Minimum noise figure F_{min} vs. I_C and J_C at $f = 10\,GHz$; $A_E = 2.5 \times 8\,\mu m^2$ and $1.0 \times 8\,\mu m^2$*

becomes larger with higher currents, the minimum noise figure increases. According to Eq. (4.7), F_{min} rises with the square root of I_C and J_C, respectively. Hence, the transistor should be operated at low current level for low-noise design.

The behavior of the noise resistance depicted in Figure 4.24 is different. Our HBTs show a minimum at a current density of approximately $0.25\,mA/\mu m^2$ and then increases linearly with I_C. At low current, R_n tends towards infinity (kT/I_E). Since the noise resistance is a measure for the sensitivity of the noise figure to deviation of source impedance from its optimum, the current should not be lowered too much due to the resulting noise matching problems. This can be especially important in broadband circuits where the source impedance will not be optimal in the whole frequency range.

4.4.4 Geometry-Dependence

The dependence of the noise properties of an HBT upon the devices geometry is an important issue for choosing the optimal transistor size in a
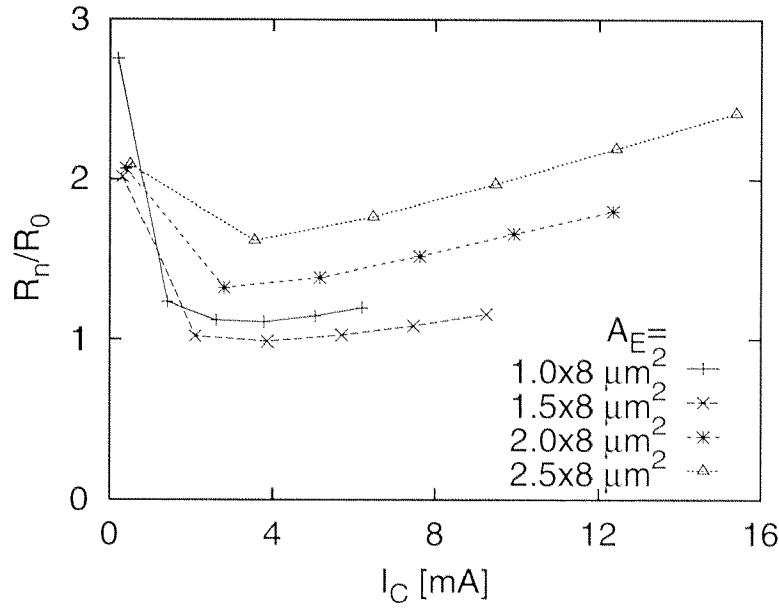
Figure 4.24: *Normalized noise resistance R_n/R_0 versus I_C, where R_0 is the reference impedance of 50 Ω; $L_E = 8\,\mu m$, $W_E = 1.0\ldots 2.5\,\mu m$*

low-noise circuit. Therefore, the noise parameters were measured for HBTs with different emitter areas, respectively emitter width and emitter length. Concerning the biasing of the devices, two different situation were investigated.

- constant collector current I_C

- constant collector current density J_C

At a constant collector current, the influences of the emitter geometry on the noise behavior caused by variation of the base and emitter resistance and of β are considered. When the devices are operated at constant collector current densities J_C, we investigate the noise properties of the transistors showing similar RF performance (the RF performance is dominantly determined by J_C).

Figure 4.25 shows the minimum noise figure F_{min} at 10 GHz versus emitter width W_E and emitter length L_E. The devices were biased at $I_C = 7\,$mA and $J_C = 510^4\,$A/cm^2, respectively. The curve for a constant collector current shows a minimum at an emitter width W_E around 1.5 μm. For wider emitters, R_B becomes larger and the thermal noise of the base resistance is increased which takes the affects F_{min} similarly. The slightly higher current gain β of the wider emitter devices reduces the base current and
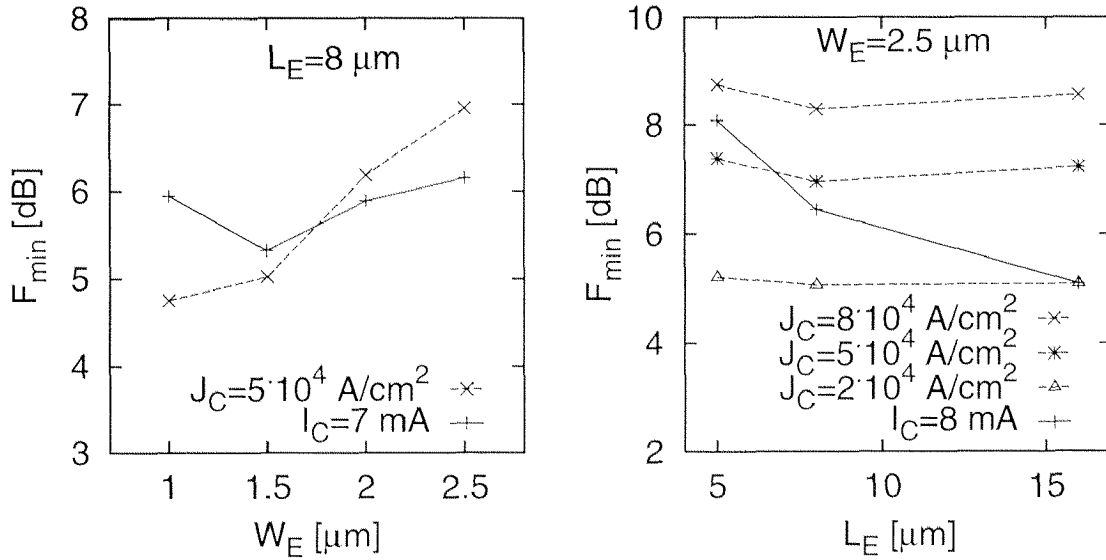
Figure 4.25: *Minimum noise figure F_{min} at 10 GHz versus emitter width W_E and emitter length L_E*

therefore the base current noise but can not compensate for the noise of the base resistance. For an emitter width smaller than 1.5 μm, the situation is quite the contrary. The base resistance is reduced, resulting in a smaller thermal noise, but β drops significantly due to surface recombination. As a consequence, F_{min} increases. Hence, for low-noise operation, the emitter width should only be reduced, as long as the current gain does not decrease.

The curve for a constant collector current density J_C does not show a minimum, but F_{min} becomes larger for wider emitters. This could be expected because all noise powers of the noise sources are larger for larger emitter widths.

In Figure 4.25, the minimum noise figure F_{min} at 10 GHz is depicted as function of the emitter length L_E at a constant collector current $I_C = 8\,\text{mA}$ and at constant collector current densities. For a given collector current, the decrease of the base and emitter resistance for longer emitter devices significantly reduces the minimum noise figure. At a constant collector current density, F_{min} is almost constant for all the investigated emitter lengths. This means that the reduction of the thermal noise of the base resistance is compensated by the increased current noise of the base and collector currents. This can be observed for all current densities. The noise characteristics of the transistor is therefore insensitive to the emitter length.

4.4.5   Temperature-Dependence

The temperature dependence of the noise behavior is mainly determined by the thermal noise of the base resistance. Figure 4.26 shows the minimum noise figure F_{min} and the noise resistance R_n as a function of the temperature. Since the thermal noise increases with rising temperature, both F_{min}
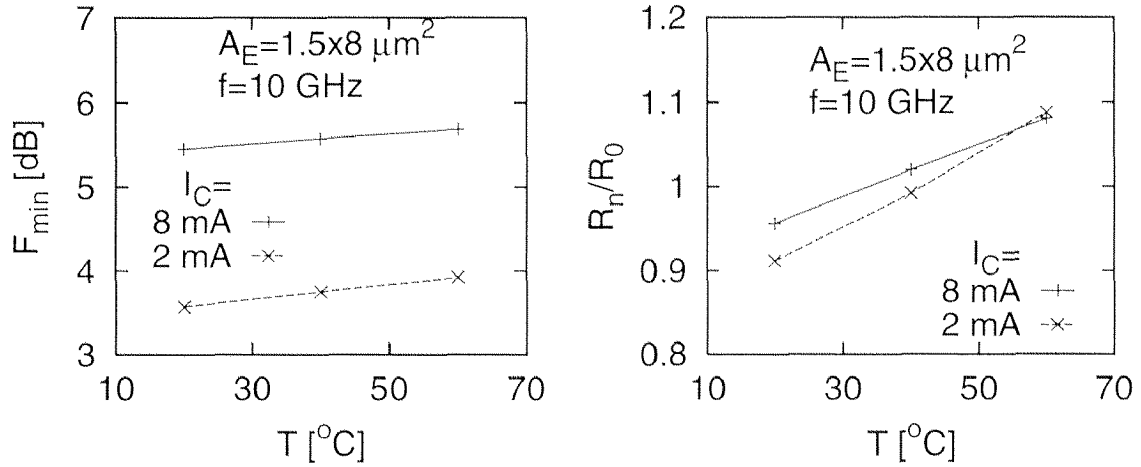
Figure 4.26: *Minimum noise figure F_{min} and noise resistance R_n versus temperature T, $A_E = 1.5 \times 8\,\mu m^2$, $f = 10\,GHz$*

and R_n become larger. The slope of the curve for R_n at $I_C = 2\,mA$ is steeper than the one for $I_C = 8\,mA$. Hence, the sensitivity upon temperature is slightly stronger for a smaller collector current because the term kT/I_E in Eq. (4.8) becomes more dominant.

4.5   Summary

A complete characterization of the DC, RF and noise properties of our InP/InGaAs SHBTs was presented. A peculiarity of these transistors are the different emission coefficients of the base and collector currents which lead the unequal small- and large-signal current gains. Concerning the RF performance, maximum values of 130 GHz and 220 GHz were obtained for f_T and f_{max}, respectively. The dependence upon the layer structure showed the expected reduction of f_T for thicker base and collector layers.

The noise behavior was characterized in the low- and high-frequency range. The low-frequency noise was found to be a superposition of a component showing an $1/f$ spectrum and components with a Lorentzian spectrum which is typical for generation-recombination noise. The fact that the

$1/f$ noise depends linearly upon base current and that it is independent of the perimeter-to-area ratio (P_E/A_E) indicates that this noise component is more likely associated with bulk effects than with surface effects. The low-frequency excess generation-recombination components show a quadratic dependence upon base current and perimeter-to-area ration. This behavior is typical for surface recombination effects.

The high-frequency noise properties were characterized using the noise parameters minimum noise figure F_{min}, noise resistance R_n and optimum source impedance Z_{opt}. The measurement results demonstrated that the devices should be operated at low collector current level. In order not to deteriorate the RF performance, the device size has to be scaled down. Care has to be taken because the base resistance, and therefore its thermal noise increases with a smaller emitter length. A reduced emitter width may diminish the small-signal current gain β which increases the base current noise. Hence, high β values are desired which can be reached with a thin base. The tradeoff constituted by high β value vs. small base resistance has to be taken into account. For our HBTs, the devices with the thinnest base of 50 nm led to the lowest noise figures since they had still a low base resistance due to the high base doping.

Chapter 5

Noise Model

For the design and even more for the optimization of a circuit with respect to noise, we need a noise model of our InP SHBT. Based on device physics and the measurement data presented in the previous chapter, a small-signal noise model was developed and implemented in the design environment HP ADS (Advanced Design System [61]). Since the model will be used for circuit design, it should not be too complex, but its parameters have to be physically reasonable all the same. In the following (Sec. 5.1) the fundamental ideas behind this model are explained. A more detailed analysis is carried out in Section 5.2 where the determination of the elements of the model, i.e. the small-signal parameters and the noise sources, is described. Finally, the simulation results using this model are compared with measurement data of the HBT (Sec. 5.3)

5.1   Model Description

In order to find a model which fits the behavior of the HBT, we investigate the cross-sectional view of the transistor depicted in Figure 5.1. We can divide the device in an intrinsic region which determines the current transport in the device and an extrinsic region which consists of the parasitic elements. In forward active operation, the base-emitter junction is forward biased and the base-collector junction is reverse biased. The base-emitter diode is therefore modeled by its small-signal resistance r_π and capacitance c_π. The base-collector diode is represented by the junction capacitance c_μ
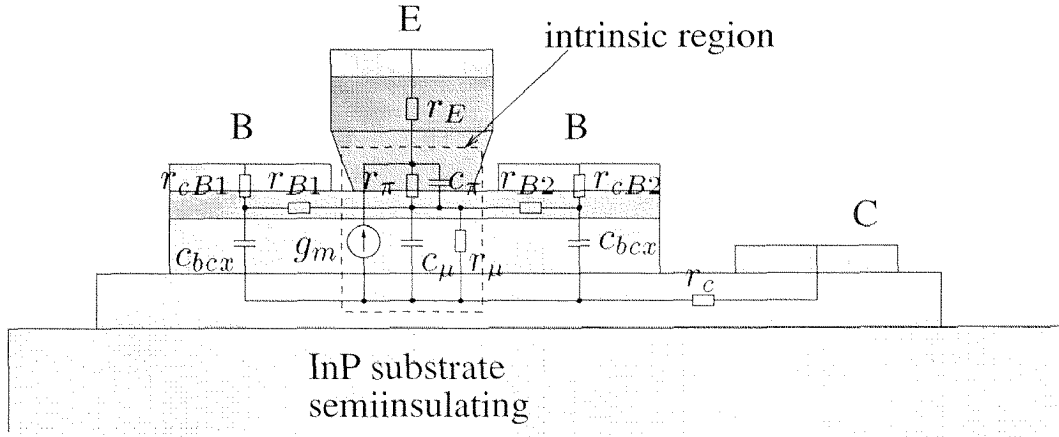
Figure 5.1: *Cross-sectional view of the HBT with the elements of the small-signal model*

and a leakage resistance r_μ. The dominant current flow in the transistor is modeled by a current source i_C which is controlled by the internal base-emitter voltage u_π by the relation $i_c = u_\pi g_m \exp(-j\omega\tau_C)$, where g_m denotes the transconductance and τ_C, the collector delay. The extrinsic region consists of the series resistances form the terminals of the device to the intrinsic region and of the junction capacitance of the extrinsic part of the base collector capacitance. The equivalent electric circuit of the model is shown in Figure 5.2. A hybrid-π model was chosen because this type of model is
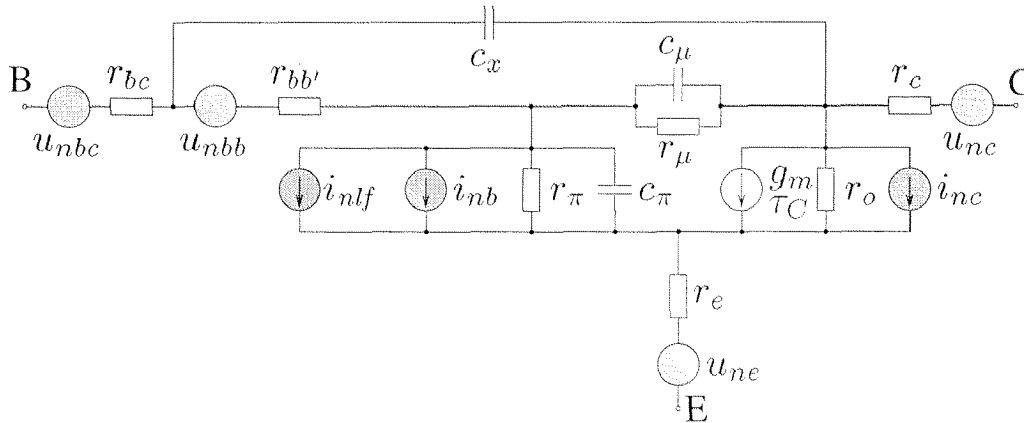
Figure 5.2: *Equivalent small-signal model including the current noise sources i_{nx} and the thermal noise sources u_{nx}*

commonly used for circuit design in contrast to the T-model which better represents the device physics than the π-model. In addition to the small-signal parameters, the noise sources are included in the model.

The model consists of the thermal noise sources (u_{nbc}, u_{nbb}, u_{ne}, u_{nc})

of the series resistances (r_{bc}, r_{bb}, r_e, r_c). In order to calculate the power spectral densities of these noise sources, the values of the resistances have to be determined. According to Eq. (2.20b), the thermal noise sources $u_{nx} = 4kTR_x$, where k is the Boltzmann constant, T the temperature, and R_x denotes the series resistance.

The second type of noise originate from the fluctuations of the base and collector currents. These fluctuations can be caused by fluctuations in the diffusion or generation-recombination processes or from shot noise. For the detailed analysis (see Sec. 5.2), the current transport and the fluctuations of these currents have to be analyzed. We will refer to the theory of homojunction bipolar transistors. Thus, the influence of the heterojunction, which could cause a quasi-ballistic instead of a diffusive transport of the electrons through the base, is not taken into account. This assumption is based on different studies [37, 35]. They suggest that the base transport is diffusive for base thicknesses X_B as small as 20 nm and therefore, ballistics transport effects should not be dominant in our devices which have $X_B > 50$ nm. The diffusive transport-modeling behavior is possible because only a small amount of scattering can produce device characteristics that appear to be diffusive although transport is far from thermal equilibrium [62]. Moreover, ballistic transport mechanism should not strongly influence the noise behavior since no carriers recombine. It may only change the frequency dependence of the noise source because they do not undergo the speed-limiting diffusion and recombination processes.

5.2 Determination of the Model Parameters

Different approaches are used to evaluate the model parameters of the equivalent circuit depicted in Figure 5.2.

We can first rely on numerical optimization techniques, second try to measure the parameters directly, or third determine them from device physics. The numerical optimization methods try to fit the S-parameters of the model to the measured S-parameters. Problems associated with this technique are that the resulting parameters depend on starting values, that the results may not be unique and that it can cost a lot of computation time for the optimization.

Direct measurement techniques of the equivalent circuit parameters are often impossible, e.g. the internal base resistance. An alternative method is to extract the model parameters directly from S-parameter measurements

[63]. This can be a good solution to determine the small-signal parameters only but is problematic for noise sources. Especially, the current noise sources and their correlation can not be determined directly from measurement data.

The third method is to determine the parameters from device physics which has the advantage that one should be able to predict the device characteristics and no time consuming measurements and optimizations would be necessary. Fully physics-based models are often too complex to be used in a circuit simulators. This causes large simulation times which would make up for the time saved for model development. Furthermore, parasitic effects e.g. surface effects are difficult to predict and moreover, differences between the nominal values of the technology parameters and the values of the parameters of the fabricated devices may lead to significant errors.

Hence, the optimal compromise or combination of these methods have to be found. We chose a combination of numerical optimization and device physics. With numerical optimization, we can fit the parameters of our model, which is well suitable for circuit simulation, so that its S-parameters will match the measured data. The device physics is used first to study the devices operation with emphasis to the noise behavior and second to chose the starting values and constraints for the optimization.

5.2.1   Currents in the HBT

Because the base and collector currents are the main variables of our noise model of the HBT, we will investigate the different current components which are illustrated in Figure 5.3 and listed below.

- electron current I_{Cn}, I_{En}

- bulk recombination of the base current I_{Br}

- hole injection current $I_p = I_{Bp} = I_{Ep}$

- space charge recombination current I_{SCR}

These current components are generated in different regions of the transistor and are therefore determined by the physical processes in these regions. The electron currents (I_{Cn}, I_{En}) and the bulk recombination of the base current (I_{Br}) have their origin in the diffusion and generation-recombination processes in the base region (Sec. 5.2.3). The current I_p is caused by holes injected from the base into the emitter (Sec. 5.2.2). Recombination in the
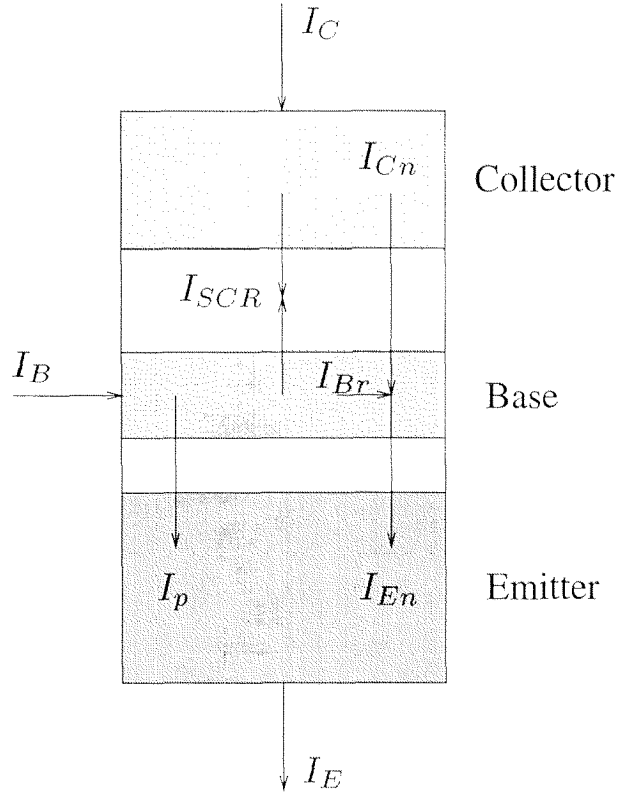
Figure 5.3: *Current components in the HBT*

space charge region of the base-collector junction leads to I_{SCR} (Sec. 5.2.4). Which one of these currents is really relevant will be worked out after the investigation of the individual currents (Sec. 5.2.5).

These current components build the collector, emitter and base terminal currents I_C, I_E, and I_B, respectively.

$$I_C = I_{Cn} + I_{SCR} \tag{5.1}$$

$$I_E = I_{En} + I_p \tag{5.2}$$

$$I_B = I_{Br} + I_p + I_{SCR} \tag{5.3}$$

For the noise consideration, the fluctuations of all these current components are calculated. These calculations are based on a linear approximation which means that the noise current ΔI fluctuates around a DC current I. The microscopic fluctuations of the currents are transformed into the noise sources i_{nx} added to the small-signal model of the transistor. Furthermore, the noise sources u_{nx} of the thermal noise of the series resistors have to be determined.

5.2.2 Noise in the Emitter

Two types of noise, the current noise and the thermal noise of the emitter series resistance, have their origins in the emitter. The current noise is determined by the holes injected from the base and diffusing through the emitter and recombining there. Although this current should be negligible in heterojunction transistors (5.2.5), the noise is calculated here all the same in order to give an introduction to the investigation of noise problems in bipolar transistors. For the calculation of the spectral noise density, the diffusion and recombination processes at the base edge of the emitter are analyzed.

The thermal noise is generated by the series resistance located between the emitter terminal and the base emitter space charge region.

Noise of the Hole Current

In order to calculate the current of the holes injected from the base into the emitter, the minority carrier concentration in the emitter has to be considered. Therefore, the continuity equations for the minority carrier flow of holes in the field-free n-region have to be solved.

$$i_p = -q\,D_p A \frac{\partial p'}{\partial x}, \qquad \frac{\partial p'}{\partial t} = -\frac{p'}{\tau_p} - \frac{1}{A\,q} \frac{\partial i_p}{\partial x} \qquad (5.4)$$

where A is the cross-sectional area through which the holes are flowing, $p' = p - p_{n,E}$ is the excess hole concentration, i_p denotes the hole current, D_p and τ_p are the diffusion constant and the hole lifetime, respectively, and q is the electron charge. Eq. (5.4) is analogous to the differential equations of the lossy transmission line depicted in Figure 5.4. The differential equations
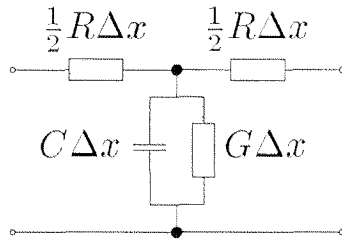
Figure 5.4: *Equivalent circuit of a lossy transmission line segment*

for this transmission line are written as

$$\frac{\partial V}{\partial x} = -R I, \qquad \frac{\partial I}{\partial x} = -G V - C \frac{\partial V}{\partial t} \qquad (5.5)$$

Comparing Eqs. (5.4) and (5.5) we can find the following analogies

$$V \mathrel{\hat=} p', \qquad I \mathrel{\hat=} i_p, \qquad R \mathrel{\hat=} \frac{1}{qD_pA}, \qquad G \mathrel{\hat=} \frac{qA}{\tau_p}, \qquad C \mathrel{\hat=} qA \qquad (5.6)$$

The expressions for the the characteristic impedance Z_0 and the propagation constant γ can be written as

$$Z_0 = \left(\frac{R}{G + j\omega C}\right)^{1/2} \mathrel{\hat=} \frac{\tau_p^{1/2}}{[q^2 D_p A^2 (1 + j\omega\tau_p)]^{1/2}} \qquad (5.7)$$

$$\gamma = [R(G + j\omega C)]^{1/2} \mathrel{\hat=} \frac{(1 + j\omega\tau_p)^{1/2}}{(D_p\tau_p)^{1/2}} \qquad (5.8)$$

For the given electron concentrations $p_{0,B}$ at the base end of the emitter the hole concentration in the emitter region can be calculated as a function of x

$$p'(x) = p'_{0,B} e^{-\gamma_E x} \qquad (5.9)$$

where γ_E is the propagation constant of the hole current in the emitter. At static condition ($\omega = 0$), the propagation constant $\gamma_{0,E} = (D_p\tau_p)^{-1/2} = 1/L_p$, where L_p denote the hole diffusion length. The resulting hole concentration of Eq. (5.9) is depicted in Figure 5.5. Since the finally calculated
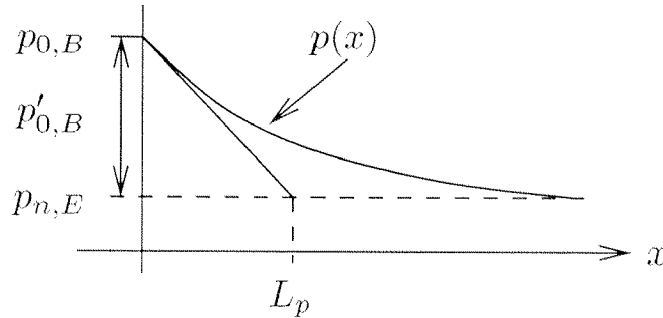
Figure 5.5: *Hole concentration in the n-doped emitter*

noise current will be expressed by the DC current, we determine here the hole current $i_p(x)$ for a carrier distribution $p'(x)$ which is independent of frequency. γ_E in Eq. (5.9) can therefore be substituted by $\gamma_{0,E}$. The resulting hole current can now be derived from the carrier concentration using Eq. (5.4)

$$i_p(x) = p'_{0,B} \, q \, D_p \, A \, \gamma_{0,E} e^{-\gamma_{0,E} x} \qquad (5.10)$$

The DC base and emitter current components which are generated by holes injected from the base into the emitter correspond to the hole current $i_p(x)$ at location $x = 0$.

$$I_p = I_{Bp} = I_{Ep} = p'_{0,B} q D_p A \gamma_{0,E} \qquad (5.11)$$

The noise generated by diffusion and g-r noise can again be considered with the analogy with the transmission line theory [64]. There are microscopic diffusion and g-r processes in the emitter which can be modeled in every element of the length dx, as shown in Figure 5.6. These microscopic noise
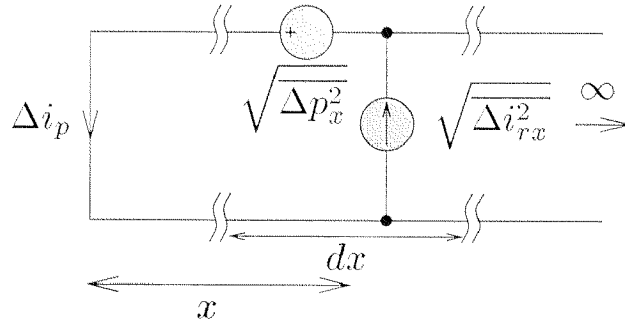
Figure 5.6: *Element of the equivalent distributed noise circuit of the emitter*

sources at location x generate a noise current Δi_p at the base edge of the emitter.

$$\Delta i_p = \Delta i_{bp} = \Delta i_{ep} = \left(\Delta i_{rx} + \frac{\Delta p_x}{Z_0} \right) e^{-\gamma_E x} \qquad (5.12)$$

The current noise of the generation-recombination processes Δi_{grx} originate from a generation current, which is proportional to the equilibrium hole density $p_{n,E}$, and from a recombination current, which is proportional to the total hole density in the base. Both of these currents show full shot noise and are assumed to be independent of each other. Hence, the power spectral density of the generation-recombination noise in the volume element $\Delta Vol = A \Delta x$ is

$$\overline{\Delta i_{grx}^2} = 2q \underbrace{\frac{qp(x) A \Delta x}{\tau_p} \Delta f}_{\overline{\Delta i_{rx}^2},\ \text{recombination}} + 2q \underbrace{\frac{qp_{n,E}(x) A \Delta x}{\tau_p} \Delta f}_{\overline{\Delta i_{gx}^2},\ \text{generation}} \qquad (5.13)$$

The diffusion component Δp_x can be obtained from the fluctuation in x direction of the diffusion current in a volume element $\Delta Vol = A \Delta x$. The

power spectral density of this fluctuation is given by Eq. (2.35)

$$\overline{\Delta i_{dx}^2} = 4q^2 D_p p(x) \frac{A}{\Delta x} \Delta f \tag{5.14}$$

From Eq. (5.14), the fluctuation of the carrier density is $\Delta p = -\frac{\Delta i_p}{qAD_p} \Delta x$ and its power spectral density at location x can be calculated

$$\overline{\Delta p_x^2} = \overline{\Delta i_{dx}^2} \left(\frac{1}{qAD_p} \Delta x \right)^2 = \frac{4p(x)\Delta x \Delta f}{D_p A} \tag{5.15}$$

The mechanisms of fluctuation in the electron concentration due to diffusion and recombination are independent of each other. Thereafter, the noise sources are uncorrelated and the power spectral densities can be added quadratically. We can directly calculate the total power spectral densities of the noise at the base edge of the emitter $\overline{i_p^2}$.

$$\begin{aligned}
\overline{i_p^2} = \overline{i_{bp}^2} = \overline{i_{ep}^2} &= \sum \overline{\Delta i_p^2} \\
&= \frac{4q^2 A}{\tau_p} \left| \frac{\gamma_E}{\gamma_{0,E}} \right|^2 \int_0^\infty (p'(x) + p_{n,E}) e^{-2a_E x} \, dx \\
&\quad + \frac{2q^2 A}{\tau_p} \int_0^\infty (p'(x) + 2p_{n,E}) e^{-2a_E x} \, dx
\end{aligned} \tag{5.16}$$

where $a_E = \Re\{\gamma_E\} = \gamma_{0,E} \sqrt{\left(1 + \sqrt{1 + \omega^2 \tau_p^2} \right)/2}$.
The contribution of the holes injected from the base into the emitter to the noise of the base and emitter current can be calculated

$$\overline{i_p^2} = \overline{i_{bp}^2} = \overline{i_{ep}^2} = 2qI_p \left(\frac{2a_E}{\gamma_{0,E}} - 1 \right) + 2qI_{po} \frac{2a_E}{\gamma_{0,E}} \tag{5.17}$$

where $I_{po} = p_{n,E} q D_p A \gamma_{0,E}$. For the detailed calculation of Eq. (5.17), the reader is referred to Appendix C.1. For low frequencies $\left(f \ll (2\pi\tau_p)^{-1} \right)$ Eq. (5.17) reduces to

$$\overline{i_p^2} = 2q(I_p + 2I_{po}) \tag{5.18}$$

This equation can be interpreted as two currents $(I_p + I_{po})$ and $-I_{po}$ showing full shot noise in a $p-n$ junction. The shot noise model is well suitable for low-frequencies but does not describe the physical mechanism as recombination and diffusion which lead to the frequency-dependent terms in the
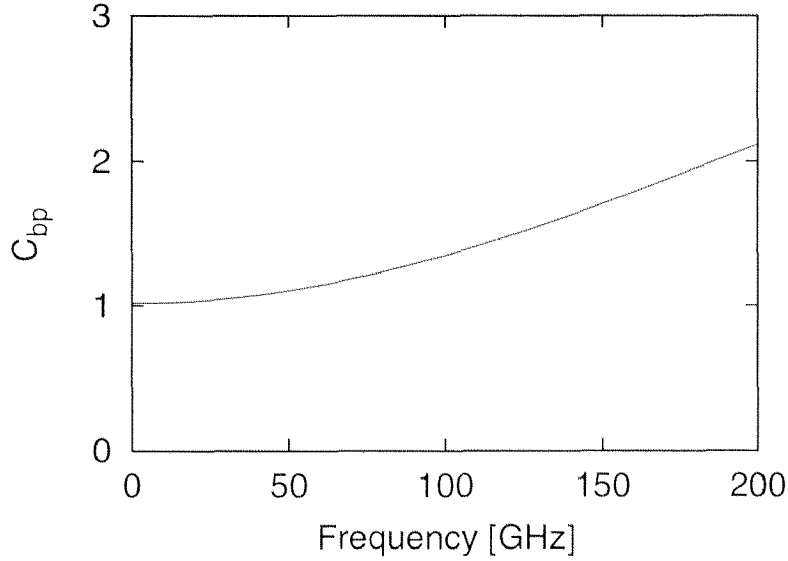
Figure 5.7: *Normalized noise power spectral density $C_{bp} = \overline{i_p^2}/(2qI_p)$ of the hole injection current vs. frequency*

previous equations. This would give incorrect results at higher frequencies. Figure 5.7 shows the normalized power spectral density $C_{bp} = \overline{i_p^2}/(2qI_p)$ of the hole injection current up to 200 GHz. As long as C_{bp} is unity, the noise current shows shot noise. However, an increase of the noise power with frequency is observed and is at 200 GHz more than double than the shot noise level. This increase can be explained by analyzing Eq. (5.12) which describes the influence of the microscopic noise sources on the noise current at the base edge of the emitter. From this equation, we learn that the influence of the diffusion noise source Δp_x becomes stronger at higher frequencies due to the reduced characteristic impedance of the transmission line Z_0. It is true that the absorption of the transmission line is higher as well at higher frequencies. For the noise at the emitter edge, where we have high minority carrier concentration, the stronger absorption does not compensate for the elevated diffusion noise power.

A more physical explanation can be given by investigating the carrier transport. At low frequencies, holes are injected from the base into the emitter and recombine there. At higher frequencies, some holes return to the base without recombining. These additional transits through the base-emitter junction lead to an elevated power spectral density of the noise current [65].

The power spectral density of the hole noise current does of course not increase to infinity. For frequencies $f \gg 1/(2\pi\tau_1)$, where τ_i are the transit

times of the recombination and diffusion processes, the exact power spectral density of the shot noise process (Eq. (2.28)) limits the power spectral density of the emitter noise current. This limiting effect is not taken into account here.

Thermal noise

In addition to the current noise, thermal noise of the series emitter resistance exists as well. This resistance consists of three parts (Fig. 5.8), the contact resistance R_{cE}, the resistance of the InGaAs cap layer R_{cap}, and the resistance of the InP-emitter R_{EE} from the cap layer to the space charge region. For the calculation of the three parts of the emitter resistance, the emitter
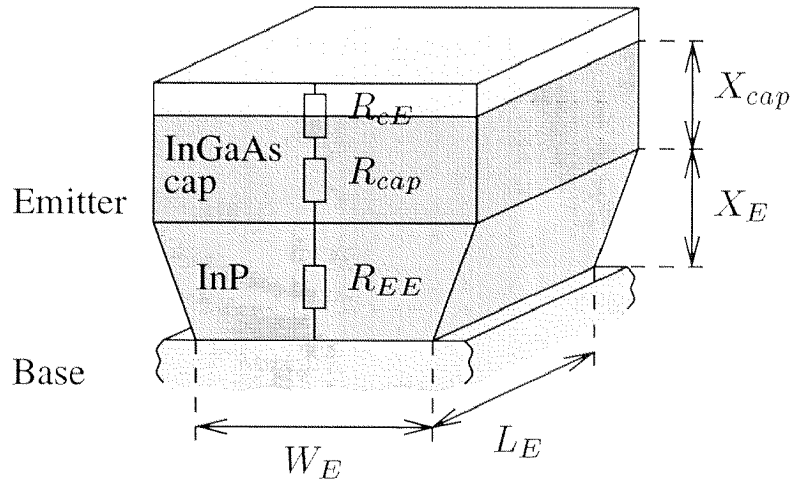
Figure 5.8: *Cross sectional view of the emitter to calculate the emitter series resistance* $R_E = R_{cE} + R_{cap} + R_{EE}$

under-cut is neglected. Thus, the the emitter area $A_E = W_E L_E$ and we obtain

$$R_{cE} = \frac{\rho_{cE}}{A_E} \tag{5.19}$$

$$R_{cap} = \frac{\rho_{b,cap} X_{cap}}{A_E} \tag{5.20}$$

$$R_{EE} = \frac{\rho_{bE} X_E}{A_E} \tag{5.21}$$

$$R_E = R_{cE} + R_{cap} + R_{EE} \tag{5.22}$$

where ρ_{cE} denotes the specific contact resistance, $\rho_{b,cap}$ and ρ_{bE} are the specific resistance of the cap and emitter layer, respectively. X_{cap} and X_E

are the thicknesses of the cap and emitter layer, respectively. The specific resistances can either be determined from measurement data of sheet, respectively contact resistance or from the technology parameters presented in Table 5.1. The measurement method which we have used is based on a

	doping [cm^{-3}]	μ [66] [cm^2/Vs]	ρ [Ωcm]	X [nm]
cap	$2 \cdot 10^{19}$	700	$4.5 \cdot 10^{-4}$	300
emi1	$1 \cdot 10^{19}$	1000	$6.3 \cdot 10^{-4}$	50
emi2	$4 \cdot 10^{17}$	2800	$5.6 \cdot 10^{-3}$	250

Table 5.1: *Experimentally obtained technology parameters used for the calculation of the emitter series resistance*

transmission line model (TLM) [67]. This method is well suited for measuring the contact resistance ρ_{cE}. A typical value of $1 \cdot 10^{-7} \, \Omega \text{cm}^2$ was obtained. A problem occurs for measuring the sheet resistances of all layers. Due to the lateral current flow in the TLM-method and the different specific resistances of the different layers, the current is not homogeneously distributed and the the method is not useful. For the resistances of the layer we therefore rely on technology data (Table 5.1). In order to compare the different components of the emitter resistance, the specific resistances are multiplied by the layer thicknesses. As an example for an emitter area of

	contact	cap	emi1	emi2
ρ [Ωcm^2]	$1 \cdot 10^{-7}$	$1.35 \cdot 10^{-8}$	$0.315 \cdot 10^{-8}$	$1.4 \cdot 10^{-7}$
Rel.	39 %	5 %	1 %	55 %

Table 5.2: *Relative contribution to the total emitter resistance of the contact and the different layer resistances*

$1.5 \times 8 \, \mu\text{m}^2$, the total emitter resistance R_E is $2.1 \, \Omega$.

The power spectral density of the thermal noise associated with the emitter resistance R_E can then be calculated using Eq. (2.20b)

$$\overline{u_{nR_E}^2} = 4kTR_E \tag{5.23}$$

where k is the Boltzmann constant and T, the absolute temperature.

5.2.3 Noise in the Base

As in the emitter, current noise and thermal noise are also generated in the base region. Fluctuations in the diffusion and recombination processes determine the noise currents. In contrast to the homojunction bipolar transistor, recombination cannot be neglected because of the high base doping which is made possible by the heterojunction but leads to a short lifetime of the minority carriers (20 . . . 30 ps). The thermal noise in the base originates from the base series resistance between the base terminal and the intrinsic transistor region.

Noise of the Electron Current

In order to calculate the the power spectral densities of the noise sources in the base, the differential equations governing the electron current flow in the base are solved. Doing this, the noise generated by the recombination and diffusion processes in the base are considered. In analogy to the emitter, the first step is to analyze the differential equation for the electron transport in a p-doped base region.

$$i_n = q\, D_n A \frac{\partial n'}{\partial x}, \qquad \frac{\partial n'}{\partial t} = -\frac{n'}{\tau_n} + \frac{1}{A\,q} \frac{\partial i_n}{\partial x} \qquad (5.24)$$

A is the cross-sectional area where the electrons are injected from the emitter, $n' = n - n_p$ is the excess electron concentration, i_n denotes the electron current in x-direction, D_n and τ_n are the electron diffusion constant and the electron lifetime, respectively, and q ,is the electron charge. The boundary conditions for the calculation of the carrier concentration is different than in the emitter because of the finite thickness X_B of the base. This leads to a different function, with respect to the location x, of electron concentration in the base than the hole concentration in the emitter. For the given electron concentrations $n_{0,E}$ at the emitter end and $n_{0,C}$ at the collector end of the base, respectively, the electron concentration in the base region can be calculated as a function of x

$$n(x) = n_{0,E} \frac{\sinh \gamma_B (X_B - x)}{\sinh \gamma_B X_B} + n_{0,C} \frac{\sinh \gamma_B x}{\sinh \gamma_B X_B} \qquad (5.25)$$

where X_B is the base width, and $\gamma_B = \gamma_{0,B} \sqrt{1 + j\omega\tau_n}$ is the propagation constant with $\gamma_{0,B} = (D_n \tau_n)^{-1/2} = 1/L_n$; L_n is the diffusion length. Figure 5.9 shows the electron concentration in the base. The deviation of
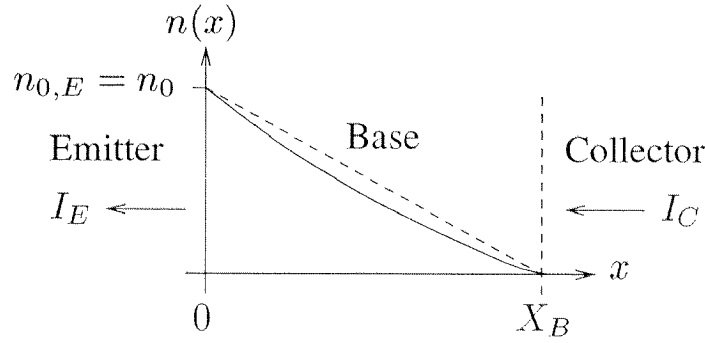
Figure 5.9: *Electron concentration in the p-doped base*

the carrier concentration from a linear decrease (- - -) from the emitter to the collector boundaries of the base is a consequence of recombination.

According to Eq. (5.24), the electron current at the location x becomes

$$i_n(x) = -n_0\, q\, D_n\, A\, \gamma_B\, \frac{\cosh \gamma_B(X_B - x)}{\sinh \gamma_B X_B} \tag{5.26}$$

where $n_0 = n_{0,E}$. The emitter and collector current are $-i_n(x = 0)$ and $-i_n(x = X_B)$, respectively.

$$I_{En} = n_0\, q\, D_n\, A\, \gamma_B \frac{1}{\tanh \gamma_B X_B} \tag{5.27}$$

$$I_{Cn} = n_0\, q\, D_n\, A\, \gamma_B \frac{1}{\sinh \gamma_B X_B} \tag{5.28}$$

The base current due to recombination $I_{Br} = I_{En} - I_{Cn}$ and the current gain $B = I_{Cn}/I_{Br}$ is determined by bulk recombination in the base region, if only the electron transport in the base is considered.

$$I_{Br} = I_{En} - I_{Cn} = n_0\, q\, D_n\, A\, \gamma_B \frac{\cosh \gamma_B X_B - 1}{\sinh \gamma_B X_B} \tag{5.29}$$

$$B = \frac{I_{Cn}}{I_{Br}} = \frac{1}{\cosh \gamma_B X_B - 1} \tag{5.30}$$

This is valid for $X_B \ll L_n$.

For the consideration of the noise in the base region, we can take advantage of the analogy of the diffusion equation and the equation of a transmission line [64] with microscopic generation-recombination and diffusion noise sources, as depicted in Figure 5.10. Using this analogy, we can calcu-
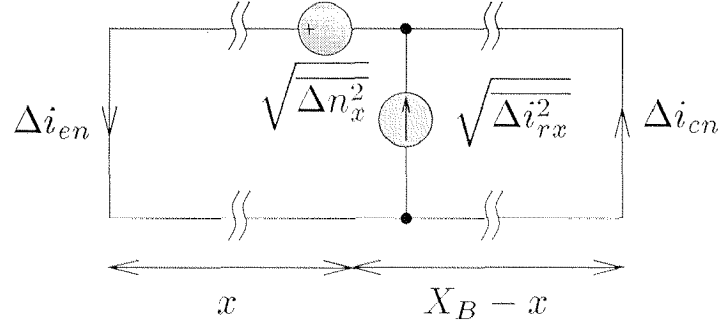
Figure 5.10: *Element of the equivalent distributed noise circuit of the base with base thickness* $X_B \ll L_n$, L_n *electron diffusion length*

lated the fluctuations of the noise currents at the emitter edge (Δi_{en}) and collector edge (Δi_{cn}) of the base, expressed by the microscopic noise sources.

$$\Delta i_{en} = \frac{\Delta n_x}{Z_0} \frac{\cosh \gamma_B (X_B - x)}{\sinh \gamma_B X_B} + \Delta i_{grx} \frac{\sinh \gamma_B (X_B - x)}{\sinh \gamma_B X_B} \quad (5.31)$$

$$\Delta i_{cn} = \frac{\Delta n_x}{Z_0} \frac{\cosh \gamma_B x}{\sinh \gamma_B X_B} - \Delta i_{grx} \frac{\sinh \gamma_B x}{\sinh \gamma_B X_B} \quad (5.32)$$

where $Z_0 = \frac{1}{qA} \sqrt{\tau_n / \left(D_n (1 + j\omega \tau_n) \right)}$ denotes the characteristic impedance. Δn_x and Δi_{grx} represent the microscopic diffusion and generation-recombination noise source, respectively.

In analogy to Eqs. (5.13) and (5.15), the power spectral densities of the diffusion component $\overline{\Delta n_x^2}$ and generation-recombination component $\overline{\Delta i_{grx}^2}$ are

$$\overline{\Delta n_x^2} = \overline{\Delta i_{dx}^2} \left(\frac{1}{qAD_n} \Delta x \right)^2 = \frac{4n(x)\Delta x \Delta f}{D_n A} \quad (5.33)$$

$$\overline{\Delta i_{grx}^2} = \underbrace{2q \frac{qn(x)A\Delta x}{\tau_n} \Delta f}_{\overline{\Delta i_{rx}^2}, \text{ recombination}} + \underbrace{2q \frac{qn_p(x)A\Delta x}{\tau_n} \Delta f}_{\overline{\Delta i_{gx}^2}, \text{ generation}} \quad (5.34)$$

For simplicity, n_p is neglected with respect to n ($n \gg n_p \to n \simeq n'$) and thus, the generation noise can be neglected.

As already assumed for the emitter, the fluctuation in the electron concentration due to diffusion and recombination are independent of each other. Hence, the power spectral densities of the noise at the emitter and collector edge of the base $\overline{i_{en}^2}$ and $\overline{i_{cn}^2}$, respectively, are obtained by a quadratic addi-

tion of the individual noise sources which results in the following integrals.

$$\overline{i_{en}^2} = \sum \overline{\Delta i_{en}^2}$$

$$= \frac{4q^2 A}{\tau_n} \left| \frac{\gamma_B}{\gamma_{0,B}} \right|^2 \int_0^{X_B} n(x) \left| \frac{\cosh \gamma_B (X_B - x)}{\sinh \gamma_B X_B} \right|^2 dx$$

$$+ \frac{2q^2 A}{\tau_n} \int_0^{X_B} n(x) \left| \frac{\sinh \gamma_B (X_B - x)}{\sinh \gamma_B X_B} \right|^2 dx \qquad (5.35)$$

$$\overline{i_{cn}^2} = \sum \overline{\Delta i_{cn}^2}$$

$$= \frac{4q^2 A}{\tau_n} \left| \frac{\gamma_B}{\gamma_{0,B}} \right|^2 \int_0^{X_B} n(x) \left| \frac{\cosh \gamma_B x}{\sinh \gamma_B X_B} \right|^2 dx$$

$$+ \frac{2q^2 A}{\tau_n} \int_0^{X_B} n(x) \left| \frac{\sinh \gamma_B x}{\sinh \gamma_B X_B} \right|^2 dx \qquad (5.36)$$

The correlation between emitter and collector noise currents results in

$$\overline{i_{en}^* i_{cn}} = \sum \overline{\Delta i_{en}^* \Delta i_{cn}}$$

$$= \frac{4q^2 A}{\tau_n} \left| \frac{\gamma_B}{\gamma_{0,B}} \right|^2 \int_0^{X_B} n(x) \frac{\cosh \gamma_B^* (X_B - x) \cosh \gamma_B x}{|\sinh \gamma_B X_B|^2} dx$$

$$- \frac{2q^2 A}{\tau_n} \int_0^{X_B} n(x) \frac{\sinh \gamma_B^* (X_B - x) \sinh \gamma_B x}{|\sinh \gamma_B X_B|^2} dx \qquad (5.37)$$

In each equation of the Eqs. (5.35) to (5.37), the first integral corresponds to the diffusion noise source and the second to the recombination noise source.

For the noise of the base current, its correlation with the collector current and, according to Eq. (2.3), for the correlation coefficient c_{ibic} we obtain

$$\overline{i_{br}^2} = \overline{(i_{en} - i_{cn})(i_{en} - i_{cn})^*}$$

$$= \overline{i_{en}^2} - 2 \Re \left(\overline{i_{en}^* i_{cn}} \right) + \overline{i_{cn}^2} \qquad (5.38)$$

$$\overline{i_{br}^* i_{cn}} = \overline{i_{en}^* i_{cn}} - \overline{i_{cn}^2} \qquad (5.39)$$

$$c_{ibic} = \frac{\overline{i_{br}^* i_{cn}}}{\sqrt{\overline{i_{br}^2} \; \overline{i_{cn}^2}}} \qquad (5.40)$$

The interpretation of these results is carried out by a numerical analysis because the analytic calculation of the the integrals leads to complex expressions. For our model, the noise of the base and collector currents are

of interest. Therefore, the normalized power spectral noise densities $C_{bb} = \overline{i_{br}^2}/(2qI_B)$ and $C_{cc} = \overline{i_{cn}^2}/(2qI_C)$ of the base and collector, respectively, for base thicknesses from 50 to 100 nm are shown in Figure 5.11. Full shot
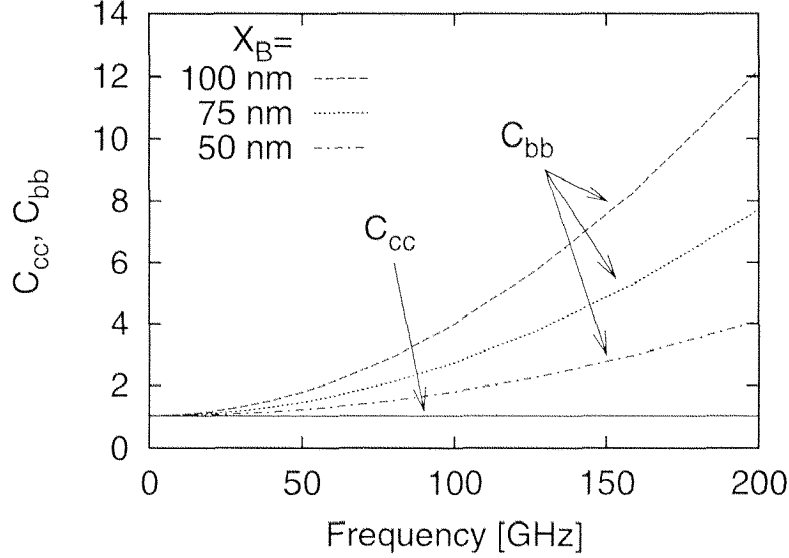
Figure 5.11: *Normalized power spectral densities* $C_{bb} = \overline{i_{br}^2}/(2qI_B)$ *and* $C_{cc} = \overline{i_{cn}^2}/(2qI_C)$ *of the base and collector noise currents for base thicknesses* $X_B = 50, 75,$ *and* $100\,nm$, $\tau_n = 20\,ps$ *and* $D_n = 44\,cm^2/s$

noise, i.e. both C_{bb} and C_{cc} equal unity, can be observed at low frequencies. At higher frequencies, the collector current noise still shows shot noise, whereas the base noise significantly increases. This characteristics of the noise currents can be similarly explained to the noise current in the emitter (Sec. 5.2.2), where an increased diffusion noise was noticed at higher frequencies at locations with high carrier concentration. A high carrier concentration is found at the emitter edge of the base. At a larger distance from the emitter edge where the carrier concentration decreases as well, absorption of the dominant microscopic noise sources becomes stronger. Moving toward the collector edge, where the excess hole concentration is zero, absorption compensates the increase originating from the reduced characteristic impedance and a white spectrum will be found. Hence, the collector noise is constant with frequency.

The physical explanation is also similar to Section 5.2.2 and to [65]. The electrons are injected from the base into the emitter. At lower frequencies, they are either collected by the collector or the recombine. At higher frequencies, some electrons return to the emitter before they recombine or before they reach the collector. These returning electrons lead to an increase

of the base current noise. This increase is again limited by the decay of the power spectral density of the shot noise processes at higher frequencies, which is not taken into account in this model.

For the variation of the base thickness from 50 to 100 nm, the increase is between 10 and 20 % in the frequency range from 2 to 26 GHz, where measurements of the noise parameters are possible. In contrast to this, the enlargement at 50 GHz is already up to a factor 2. This increase makes it unavoidable to take the frequency dependence of the noise sources into account.

In the conventional bipolar transistor noise model, the correlation coefficient c_{ibic} of the base and collector noise currents is often assumed to be zero. As depicted in Figure 5.12 this is only the case at low frequencies. At
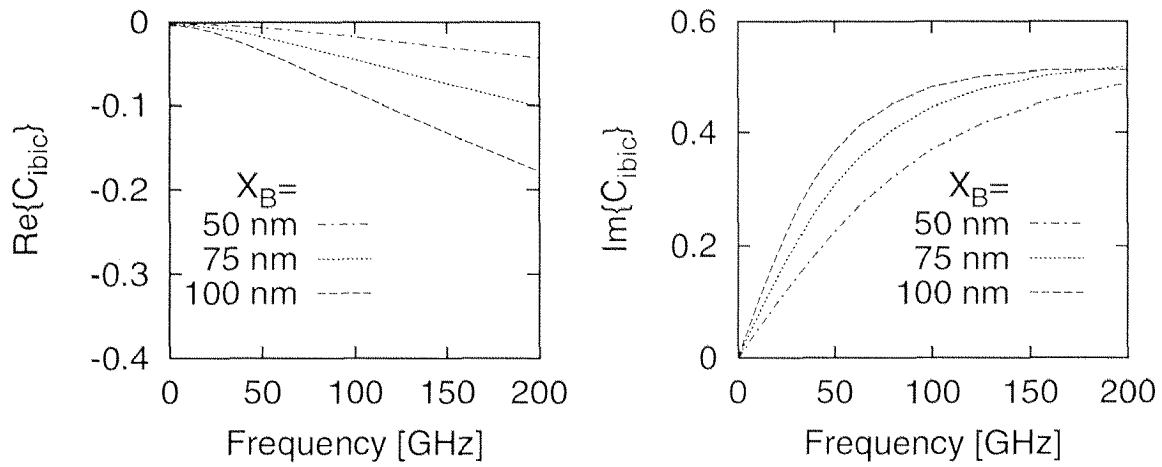
Figure 5.12: *Real and imaginary part of the correlation coefficient c_{ibic} of the base and collector noise currents vs. frequency*

higher frequencies, this is not the case anymore. In Figure 5.12, we observe a negative real part and a positive imaginary part of c_{ibic}. As already for C_{bb} and C_{cc}, the deviation from zero is stronger for larger base thicknesses.

The simulation of the noise generated in the base was carried out for diffusion constant $D_n = 44\,\mathrm{cm^2/s}$ and an electron lifetime $\tau_n = 20\,\mathrm{ps}$, which were measured for a base doping of $3.5 \cdot 10^{19}\,\mathrm{cm^{-3}}$ [6]. Since these two measures are difficult to determine exactly and different values were found in literature [68, 69], their influence on the base and collector noise was investigated and presented in Figure 5.13. Longer electron lifetimes and smaller diffusion constants lead to a stronger frequency dependence base current noise source.

From these simulations, we evaluate the power spectral densities of the
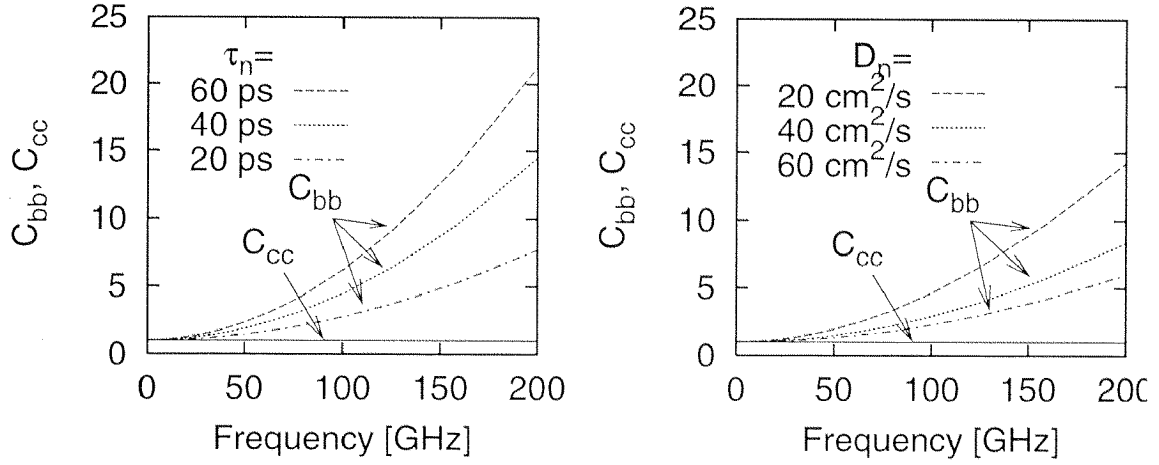
Figure 5.13: *Influence of the diffusion length* D_n *and electron lifetime* τ_n *on the normalized base and collector current noise* $C_{bb} = \overline{i_{br}^2}/(2qI_B)$ *and* $C_{cc} = \overline{i_{cn}^2}/(2qI_C)$, $X_B = 75\,nm$

noise sources incorporated in the model and their correlation as well. We obtain

$$\overline{i_{br}^2} = 2qI_B\left(1 + (\omega\tau_{nb})^2\right) \tag{5.41}$$

$$\overline{i_{cn}^2} = 2qI_C \tag{5.42}$$

$$\overline{i_{br}^* i_{cn}} = 2qI_C(e^{-j\omega\tau_B/3} - 1) \tag{5.43}$$

where $\tau_B = \frac{X_B^2}{2D_n}$ denotes the base delay and $\tau_{nb} = \sqrt{\tau_n \tau_B/3}$. In order to obtain a good agreement between measurement and model in the frequency range from 2 to 26 GHz, it is not absolutely necessary to take the frequency dependence of the base noise current into account. On the other hand, if the model should be extrapolated to higher frequencies, frequency dependent base noise source and correlation current have to be employed.

Not only the frequency dependence of the current noise sources, but also the different emission coefficients of the base and collector currents affect the correlation between the base and collector noise [18]. This influence is not taken into account in the model described before and leads to an additional term in Eq. (5.43). We then obtain for the correlation current

$$\overline{i_{br}^* i_{cn}} = 2qI_C\left(\frac{n_e}{n_F}e^{-j\omega\tau_B/3} - 1\right) \tag{5.44}$$

where $n_e = \frac{\beta n_F + n_B}{1+\beta}$. This influence of the emission coefficients can

roughly be explained by the fact that we express the noise currents by DC currents, but actually, they are small-signal quantities.

Thermal Noise

The thermal noise in the base of the HBT is determined by the base series resistance R_B. Figure 5.14 illustrates the different parts of R_B. The to-
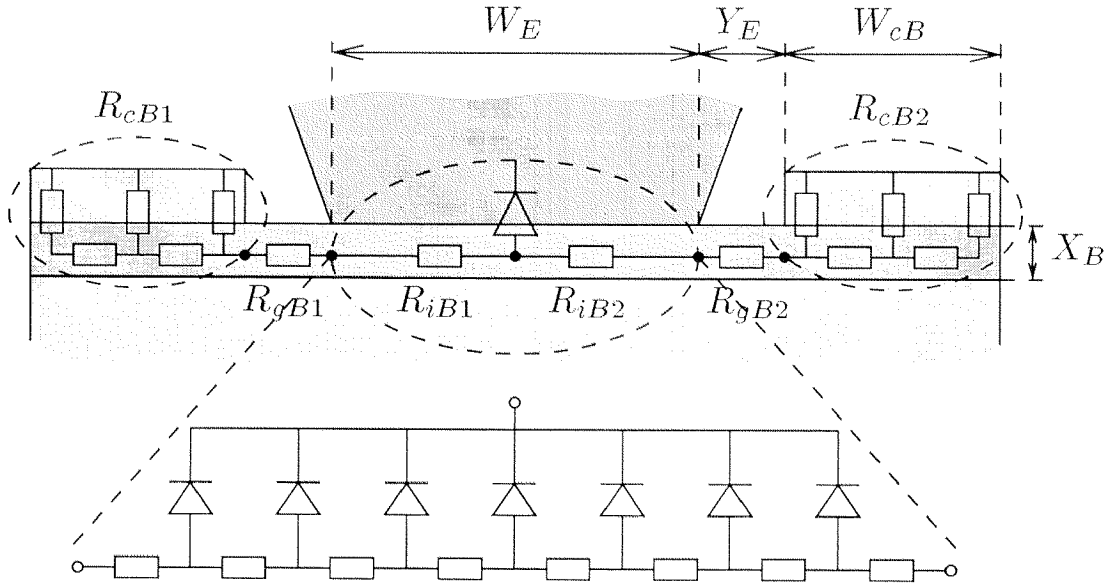
Figure 5.14: *Cross-sectional view of the base to calculate the base resistance $R_B = R_{cB} + R_{gB} + R_{iB}$, distributed internal base resistance R_{iB} and contact resistance R_{cB}*

tal base resistance is formed of a contact resistance $R_{cB} = R_{cB1}||R_{cB2}$, a gap resistance $R_{gB} = R_{gB1}||R_{gB2}$ and an internal base resistance $R_{iB} = R_{iB1}||R_{iB2}$, respectively. The calculation of the resistances is different to the emitter because of the lateral current flow of the base current in contrast to the vertical current flow in the emitter. The base contact resistance and the internal base resistance must be considered as distributed elements. This is necessary because the current flow along the contact or base-emitter junction, respectively, causes a voltage drop leading to a non-uniform current flow.

Berger [67] investigated distributed contact resistances using a transmission line model (TLM). The results of this TLM-method can be adopted for

the calculation of the base contact resistance

$$R_{cB} = R_{cB1} \| R_{cB2} = \frac{1}{2L_E} \sqrt{R_{sB} \rho_{c1B}} \coth\left(W_{cB} \sqrt{\frac{R_{sB}}{\rho_{c1B}}}\right) \quad (5.45)$$

where L_E is the emitter length, R_{sB} the base sheet resistance, ρ_{c1B} the specific contact resistance corrected for the TLM-method, and W_{cB} denotes the base contact width.

The effects of the distributed nature of the internal base resistance R_{iB} was investigated by Hauser [70]. This calculation takes the voltage drop in base along the base-emitter junction into account. This effect reduces the base resistance by about 20 %. For the devices with base contacts on either side of the emitter, we obtain

$$R_{iB} = \rho_{bB} \frac{W_E}{X_B L_E} \frac{\tan z - z}{4z \tan^2 z} \simeq \frac{\rho_{bB}}{12} \frac{W_E}{X_B L_E} \quad (5.46)$$

where W_E is the emitter width and z is given by the following implicit equation

$$z \tan z = \frac{I_B}{X_B L_E} \frac{W_E}{2} \frac{\rho_{bB}}{2V_T} \quad (5.47)$$

The effect of the voltage drop parallel to the junction reduces the effective forward bias applied to region of the emitter junction away from the base contact. As a consequence, the emitter current flow is modified. This modification can be taken into account by a current-dependent correction of the emitter width

$$W_{E,eff} = W_E \frac{\sin z \cos z}{z} \quad (5.48)$$

For an emitter width of 2.5 μm and a base thickness of 75 nm, $W_{E,eff}$ is about 17 % smaller than the nominal W_E at $I_B = 500\,\mu$A than at $I_B = 0$. This reduction of the emitter width gives rise to an increase of the emitter resistance by 20 % in this current range. Hence, the emitter series resistance becomes current-dependent.

The gap resistance R_{gB} can be calculated without including distributed aspects

$$R_{gB} = R_{gB1} \| R_{gB2} = \rho_{bB} \frac{Y_E}{X_B L_E} \quad (5.49)$$

This part of the base resistance has the least significant contribution to the total base resistance because of the small distance of only 50 nm between the base contact and the emitter.

The power spectral voltage density of the noise generated by the total base resistance $R_B = R_{cB} + R_{gB} + R_{iB}$ becomes

$$\overline{u_{nR_B}^2} = 4kTR_B \tag{5.50}$$

which is the conventional formula (Eq. (2.20b)) for thermal noise of an ohmic resistor.

Typical values of sheet and specific contact resistances, which were obtained by TLM-measurements for a base layer thickness of 75 nm, are $390\,\Omega/\square$ and $3 \cdot 10^{-7}\,\Omega\,cm^2$, respectively. The values of the different components of the base resistance are given in Table 5.3 for the emitter widths of 1 and 2.5 μm, an emitter length of 8 μm, a base contact width of 1 μm, and a base-emitter gap Y_E of 50 nm The internal, and therefore the overall, base

W_E	R_{iB}	R_{gB}	R_{cB}	R_B
1 μm	4.1 Ω	1.2 Ω	13.6 Ω	18.9 Ω
	22 %	6 %	72 %	
2.5 μm	10.2 Ω	1.2 Ω	13.6 Ω	25 Ω
	41 %	5 %	54 %	

Table 5.3: *Absolute values and relative contribution of the different components of the base resistance for emitter widths of 1 and 2.5 μm, $L_E = 8\,\mu$m, $W_{cB} = 1\,\mu$m, $Y_E = 50\,nm$, $I_B = 0$*

resistance decreases with smaller emitter width which is advantageous for good high-frequency (Eq. (4.4)) and noise (Eq. (5.50)) behavior. From Eq. (5.47) it becomes obvious that the internal base resistance is a function of the base current. For the two emitter width of 1 and 2.5 μm, R_{iB} is slightly reduced by about 3 and 8 %, respectively, when the base current is increased from 0 to 500 μA.

5.2.4 Noise in the Collector

Since the collector can be assumed as almost completely depleted ($X_C \leq$ 800 nm compared to $X_{depl} \simeq 500\,nm$), the noise originating in the collector can only be due to space charge recombination effects. The number of holes in the collector is very small which makes recombination very improbable.

Thus, space charge recombination current $I_{SCR} \simeq 0$ and does therefore not contribute to the noise.

An influence of the collector on the current transport and thus, on the noise behavior, is a consequence of the time the electrons need to pass the collector region. The transit time can be modeled by a delay in transconductance $g_m = g_{m0} \exp(j\omega\tau_C)$, where τ_C denotes the collector delay (Eq. (3.3)). Considering the possible noise sources, the transport of the electrons through the collector has to be analyzed. The noise generated by the drift process through the space charge region is already taken into account by the shot noise $\overline{i_{nc}^2}$, calculated from the noise in the base. Hence, without recombination in the collector space charge region, no additional noise source is located in the collector. The magnitude of the collector noise remains therefore unchanged. Only the collector delay, which affects the correlation between the base and collector current, has to be taken into account. In order to demonstrate this effect, magnitude and phase of the correlation coefficient c_{ibic} are depicted in Figure 5.15 when adding the collector delay to the collector current. The collector delay τ_C was varied from 0 to 2 ps. As
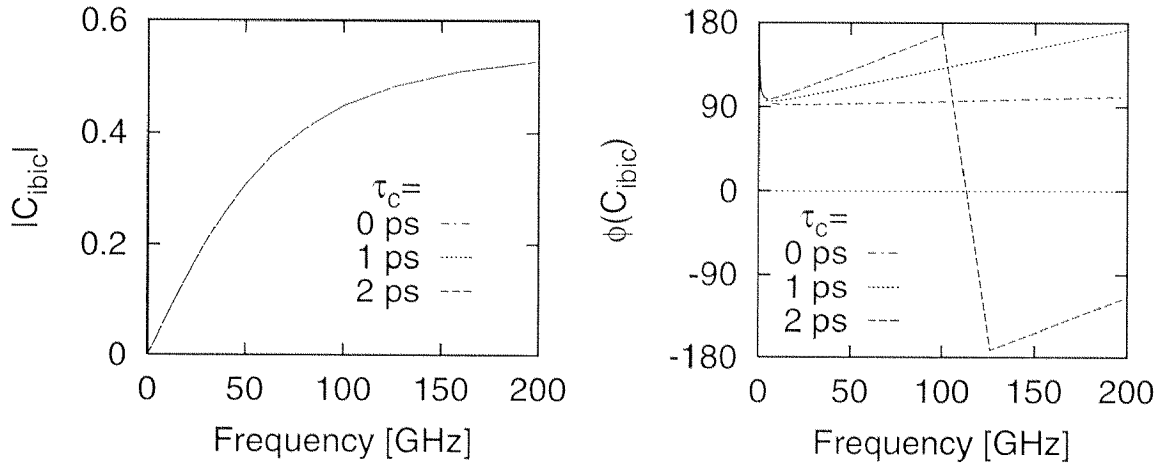
Figure 5.15: *Magnitude and phase of the correlation coefficient c_{ibic} of the base and collector noise currents for different collector delays vs. frequency,* $X_B = 75\,nm$, $\tau_n = 20\,ps$, $D_n = 44\,cm^2/s$

expected, the magnitude of c_{ibic} does not depend on the collector delay τ_C, but the phase is a linear function of τ_C. Hence, the collector noise current has to be additionally multiplied by the term $e^{j\omega\tau_C}$. Based on Eq. 5.39 and 5.43, we finally obtain for the correlation current

$$\overline{i_{br}^* i_{cnC}} = 2qI_C \left(\frac{n_e}{n_F} e^{j\omega(\tau_B/3 + \tau_C)} - 1 \right) \tag{5.51}$$

where i_{cnC} is the collector noise currents at the subcollector edge of the collector and i_{br} denotes the noise current originating from the recombination in the base.

Thermal Noise

The only noise source which is located in the collector is the thermal noise of the collector series resistor. As shown in Figure 5.16, the collector resistance is located in the subcollector and at the collector contact and therefore consists of contact resistance R_{cC}, an external resistance R_{eC}, and an internal resistance R_{iC}. The calculation of the collector contact resistance is
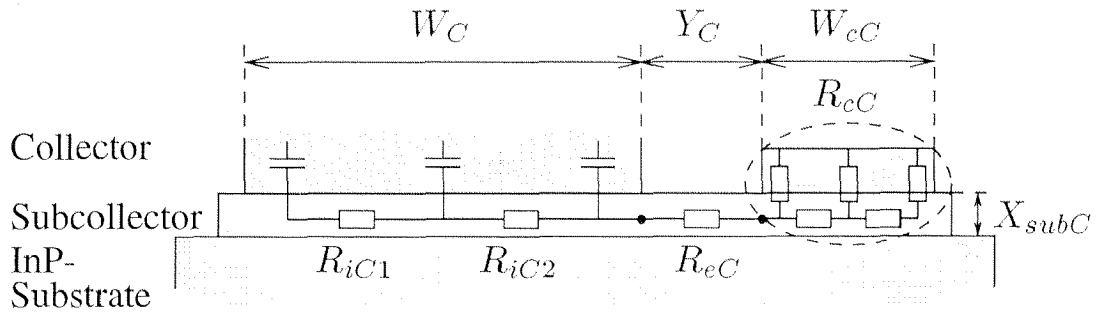
Figure 5.16: *Cross-sectional view of the subcollector to calculate the resistance* $R_C = R_{cC} + R_{eC} + R_{iC}$

similar to the base series resistance calculation. Therefore Eq. (5.45) can be applied.

$$R_{cC} = \frac{1}{2L_E} \sqrt{R_{sC}\rho_{cC}} \coth\left(W_{cC}\sqrt{\frac{R_{sC}}{\rho_{cC}}}\right) \qquad (5.52)$$

where L_E is the emitter length, R_{sC} denotes the sheet resistance of the subcollector, ρ_{cC} is the specific contact resistance corrected for the TLM-method, and W_{cC} is the width of the collector contact.

The external collector resistance for the distance Y_C of the collector contact to the collector is

$$R_{eC} = R_{sC}\frac{Y_C}{L_E} \qquad (5.53)$$

The internal collector resistances (R_{iC1} and R_{iC2}) are difficult to calculate exactly because the distribution of the current flow at the collector-subcollector interface can not be easily determined. However, the collector resistance has not a significant influence on device performance and we

therefore take only the resistor $R_{iC2} = \rho_{bC} W_C / (2 X_{subC} L_E)$ into account. Here, W_C is the collector width and X_{subC} denotes the thickness of the subcollector. The total collector resistance R_C is then $R_{cC} + R_{eC} + R_{iC2}$

For a subcollector thickness of 340 nm, TLM-measurements lead to a sheet resistance of $13\,\Omega/\square$ and the specific contact resistance results in $3.5 \cdot 10^{-7}\,\Omega\text{cm}^2$. The layout data ($W_{cC} = 6.5\,\mu\text{m}$, $Y_C = 3\,\mu\text{m}$, $W_C = $

R_{iC}	R_{eC}	R_{cC}	R_C
$1.4\ldots2.2\,\Omega$	$2.4\,\Omega$	$2.7\,\Omega$	$6.5\ldots7.3\,\Omega$
$22\ldots30\,\%$	$37\ldots33\,\%$	$41\ldots37\,\%$	

Table 5.4: *Absolute values and relative contribution of the different components of the collector resistance, $W_{cC} = 6.5\,\mu m$, $Y_C = 3\,\mu m$, $W_C = 3.5\ldots5.5\,\mu m$,*

$3.5 \ldots 5.5\,\mu\text{m}$) for the calculation of the resistances are taken from a transistor having an emitter area of $1 \ldots 2.5 \times 8\,\mu\text{m}^2$.

5.2.5 Comparison of the Current Noise Sources

In Sections 5.2.2 and 5.2.3 currents and therefore current noise originating in the emitter (I_p) and base (I_{En}, I_{Cn}, I_{Br}) were investigated. There, no information was given which of these currents dominate. The main question is whether the base current is either determined by the recombination current I_{Br} or the hole injection current I_p or whether both of these currents have to be taken into account. In general, I_B is the sum of I_{Br} and I_p calculated in Eqs. (5.29) and (5.11), respectively. This sum is given by

$$I_B = I_{Br} + I_p = n_0\, q\, D_n\, A\, \gamma_B \frac{\cosh\, \gamma_B X_B - 1}{\sinh\, \gamma_B X_B} + p'_{0,B} q D_p A \gamma_{0,E}$$

$$= I_{Br} \left(1 + \underbrace{\frac{p'_{0,B} q D_p A \gamma_{0,E}}{n_{0,E}\, q\, D_n\, A\, \gamma_B}}_{A} \underbrace{\frac{\sinh\, \gamma_B X_B}{\cosh\, \gamma_B X_B - 1}}_{\approx 1} \right) \qquad (5.54)$$

Term A in Eq. (5.54) is most significantly dominated by the ratio of the minority carrier densities in the emitter ($p'_{0,B}$) and the base ($n_{0,E}$) at either side of the base-emitter space charge region. This ratio is given by

$$\frac{p'_{0,B}}{n_{0,E}} = \frac{N_{A,E}}{N_{D,B}} e^{(E_{g,InGaAs} - E_{g,InP})/kT} \qquad (5.55)$$

where $N_{A,E}$ and $N_{D,B}$ are the acceptor and donor doping concentrations in the emitter and base, respectively, E_g, the band gaps of InP and InGaAs, k is the Boltzmann constant, and T, the temperature in Kelvin. For the InP emitter and the InGaAs base, the band gap difference is sufficiently large, so that

$$\underbrace{E_{g,InP} - E_{g,InGaAs}}_{590\,meV} \gg \underbrace{kT}_{25\,meV} \tag{5.56}$$

Thus, the term A in Eq. (5.54) can be neglected and $I_B \approx I_{Br}$. The base current is therefore determined by recombination in the base region and moreover, the base recombination current noise $\overline{i_{br}^2}$ is the dominant base current noise source.

5.2.6   Low-Frequency Noise Source

In Section 4.3.2, we found from the measurements that the power spectral density of the low-frequency noise can be represented by

$$\overline{i_{nlf}^2} = \frac{B_0}{f} + \sum_{i=1}^{3} \frac{B_i}{f_{0,i}} \frac{1}{1 + \left(\frac{f}{f_{0,i}}\right)^2} \tag{5.57}$$

The $1/f$-component B_0 was found to be a linear function of the base current and for a constant base current, B_0 was almost independent of the emitter geometry.

Because of the fact that we could not measure the noise power from 500 kHz to 2 GHz, which is the frequency range where the $1/f$ corner frequency f_c is located, we will use our model to evaluate f_c. Figure 5.17 shows the power spectral density of the collector noise current in a $50\,\Omega$ environment. A $1/f$ corner frequency of 9 MHz can be extrapolated. Compared to values found in the literature (Ch. 4.3.2), this value is quite high for bipolar devices.

5.2.7   Small-Signal Parameters

In the previous sections, we calculated the model elements which include a noise generator. These are all the series resistances (r_{bb}, r_{bc}, r_e, and r_c) and the noise sources (i_{nb}, i_{nlf}, i_{nc}). We now have to determine the remaining
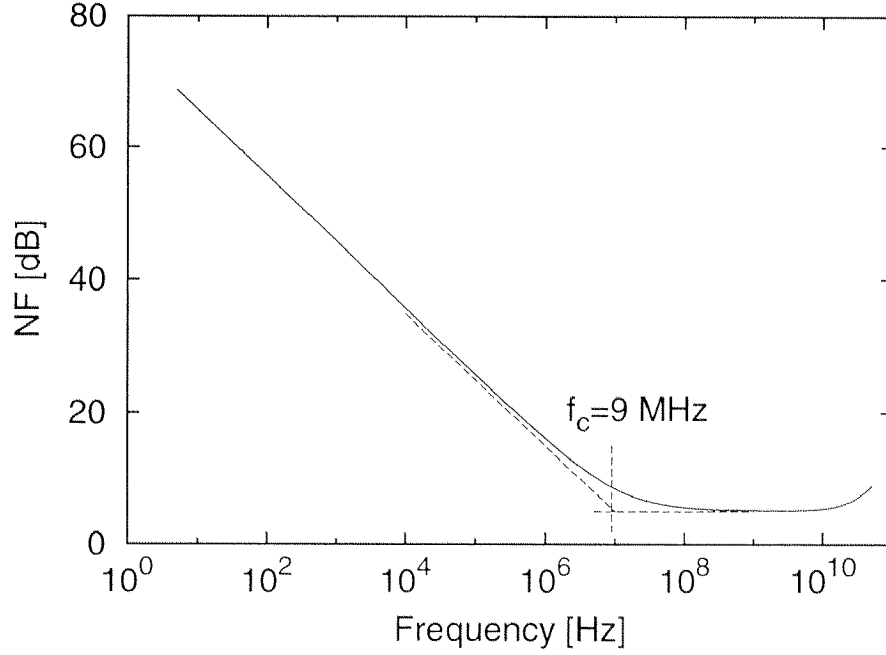
Figure 5.17: *Noise figure of an HBT with* $A_E = 1.5 \times 8\,\mu m^2$ *operated at* $I_C = 5.7\,mA$ *in a* $50\,\Omega$ *environment*

small-signal parameters (r_π, c_π, g_{m0}, c_μ, c_x, and r_μ) of the model depicted in Figure 5.2.

For the intrinsic parameters (r_π, c_π, g_{m0}) the equations derived in the previous sections can be used and these parameters are then given by

$$r_\pi = \left(\frac{\partial i_B}{\partial v_{BE}}\right)^{-1} \simeq \frac{n_B V_T}{I_B} \tag{5.58}$$

$$c_\pi = \left(\frac{\partial Q_B}{\partial v_{BE}}\right) + c_{jE} \simeq \underbrace{\frac{\tau_n I_B}{n_B V_T}}_{C_d} + \underbrace{c_{jAE} W_E L_E}_{c_{je}} \tag{5.59}$$

$$g_{m0} = \left(\frac{\partial i_C}{\partial v_{BE}}\right) \simeq \frac{I_C}{n_F V_T} \tag{5.60}$$

where $V_T = kT/q$ is the thermal voltage. In our model, the temperature is given by $T = T_C + \Delta T$, T_C is the ambient temperature and ΔT is caused by the heating of the device due to the dissipated power P_{diss}. Hence, $\Delta T = K_C \cdot P_{diss}$. The temperature coefficient K_C is assumed to be equal for all devices. The temperature T naturally influences the thermal noise of the series resistances. The emission coefficients n_B and n_F of the base and collector currents, respectively, are determined from Gummel-plot data

(Sec. 4.1.2). Thus, r_π and g_m are given by the Gummel-characteristics. The capacitance c_π consists of the diffusion capacitance C_d and the base-emitter junction capacitance. C_d is related to the electron lifetime τ_n in the base. The lifetime τ_n depends on the base doping. Values between 20 and 40 ps were found in literature for base dopings of $2 \cdot 10^{19} \, \text{cm}^{-3}$ to $4 \cdot 10^{19} \, \text{cm}^{-3}$ [71]. Since value τ_n is uncertain, τ_n is a fitting parameter in the range from 20 to 40 ps, but the value must be the same for all devices on the same wafer. Furthermore, the specific junction capacitance c_{jAE} of the base-emitter junction is a fitting parameter because the capacitance of a forward biased junction cannot be easily calculated.

In Section 5.2.3, the base series resistance was derived. Due to the distributed nature of the lateral device structure, which is modeled by a circuit with lumped elements, the two small-signal resistors r_{cB} and $r_{bb'}$ do not directly correspond to R_{cB} and $R_{gB} + R_{iB}$, respectively. But the sum of small-signal resistors should approximately be equal to the sum of the parameters calculated in Section 5.2.3. This means that

$$r_{bb'} + r_{bc} = R_{cB} + R_{gB} + R_{iB} = R_B \qquad (5.61)$$

The partition between r_{cB} and $r_{bb'}$ is determined by the fitting procedure. Because the layout of the base metalization of the HBT is not exactly the same as assumed in Section 5.2.3, the effective value of the total base resistance R_B may be smaller than the value which is calculated. Hence, R_B cannot be fixed for fitting.

For the calculation of the base-collector capacitances, the lateral dimension of the collector is divided into three parts. There is the intrinsic part forming C_{BCi}, a collector which is limited by the emitter edge and base contact (C_{BCg}) and the region under the base contact (C_{BCx}). The values are calculated as follows

$$c_\mu + c_x = C_{BCi} + C_{BCe} + C_{BCx} = \frac{L_E \varepsilon_0 \varepsilon_{InGaAs}}{X_{depl}}(W_E + Y_E + W_{cB})$$

$$(5.62)$$

where W_E and L_E are the emitter width and length, respectively, Y_E denotes the distance between emitter edge and base contact, and W_{cB} the base contact width (Fig. 5.14). The extraction of the model parameters c_μ and c_x leads to the problem of modeling a distributed structure by lumped elements as we already met when determining the base resistance. The base undercut may further lead to uncertainties in the base-collector capacitance. We therefore only calculate the sum of all base-collector capacitance values and obtain the partition between c_μ and c_x from fitting.

The value of the emitter series resistance r_e should be equal to the calculated R_E in Section 5.2.2 if, additionally, the reduction of the effective emitter width due to the non-uniformly distributed emitter current (Eq. (5.48)) is taken into account.

As already mentioned in Section 4.1.1, the output resistance r_0 can be determined from the output characteristics, but thermal effects give rise to a lower output resistance (steeper slope in the output characteristics). In the high-frequency range, the change of signal level is faster than the thermal time constant. Hence, the device temperature should not be changed by the RF signal which will lead to a higher output resistance r_0 than extracted from the output characteristics. The latter value can be taken as lower limit during fitting.

The remaining parameter, which has to be determined, is the leakage resistance r_μ. This resistor models the collector-base leakage currents of the reverse biased base-collector diode. Leakage currents can also originate form damages near the semiconductor surface or on the mesa sidewall [72].

5.2.8 Modeling Procedure

Here, we describe the specific way how each model parameter is determined. First, the two parameters, the dynamic resistance of the base-emitter diode r_π and the transconductance g_m are set to the value given by the bias point and the DC characteristic (Eqs. (5.58), (5.60)). Then, numerical optimization is carried out for one transistor size ($A_E = 2.0 \times 8\,\mu\text{m}^2$) and one bias point ($J_C = 5 \cdot 10^4\,\text{A/cm}^2$, $V_{CE} = 1.5\,\text{V}$) in order to fit the simulated and measured S-parameters and noise parameters. This optimization yields the values for electron lifetime in the base ($\tau_n = 30\,\text{ps}$) and the specific emitter junction capacitance per area ($c_{jAE} = 3.9\,\text{fF}/\mu\text{m}^2$). Thus, c_π (Eq. (5.59)), $\tau_B = \tau_n/\beta$, the power spectral densities of the current noise sources $\overline{i_{nb}^2}$ (Eq. (5.41)), and $\overline{i_{nc}^2}$ (Eq. (5.42)) with their correlation $\overline{i_{nbc}^2}$ (Eq. (5.51)) can now be calculated from the bias point and emitter geometry. Two parameters, r_μ and r_o can be determined by the DC-values of S_{12} and S_{22}, respectively. The remaining model elements (r_{bb}, r_e, r_c, c_μ, and c_x) are obtained by numerical optimization. The parameter range is limited by the equations derived in the previous sections.

5.3   Comparison of the Measurements vs. Simulations

In order to investigate the quality of the noise and small-signal model, the data from noise parameter and S-parameter measurements are compared with the results from the simulation using this model. The data shown here are from devices of a wafer with a base thickness of 80 nm, a collector thickness of 600 nm, and a subcollector thickness of 1100 nm (W_1 in Table 4.1). The thicknesses of the other layer are given in Table 3.1. The devices which are available on this wafer have emitter areas from $1.0 \times 8 \,\mu m^2$ to $2.5 \times 16 \,\mu m^2$. In Figure 5.18, the simulated and measured S-parameters are compared for an HBT having an emitter area of $1.5 \times 8 \,\mu m^2$ which was biased at $I_C = 9.25 \,\text{mA}$ and $V_{CE} = 1.5 \,\text{V}$. The data show very good agree-
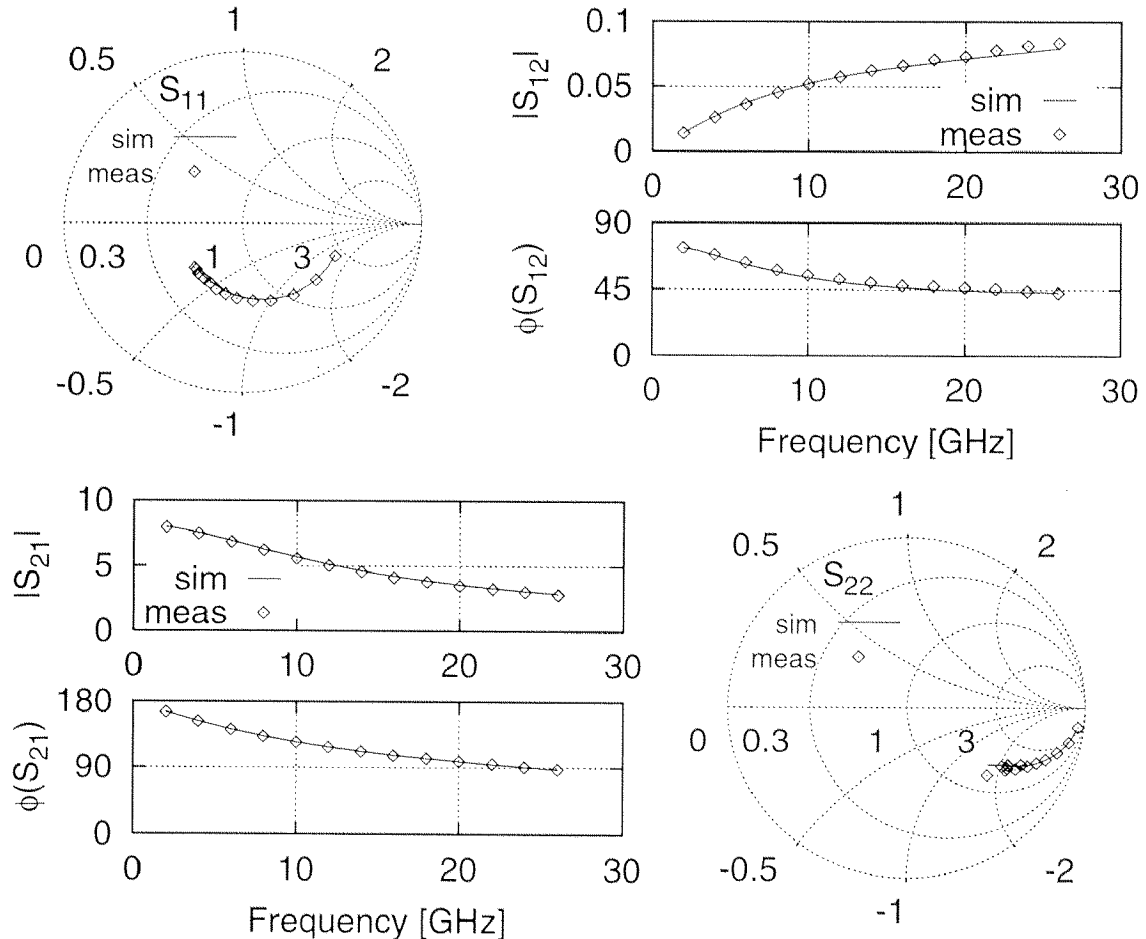
Figure 5.18: *Measured (◇) and simulated (–) S-parameters of an HBT with $A_E = 1.5 \times 8 \,\mu m^2$, $I_C = 9.25 \,mA$*

ment in the whole frequency range from 2 to 26 GHz.

The noise parameters minimum noise figure F_{min}, noise resistance R_n, optimum source reflection factor Γ_{opt} are given in Figures 5.19, 5.20, and 5.21, respectively. Not only the S-parameters, but also the noise param-
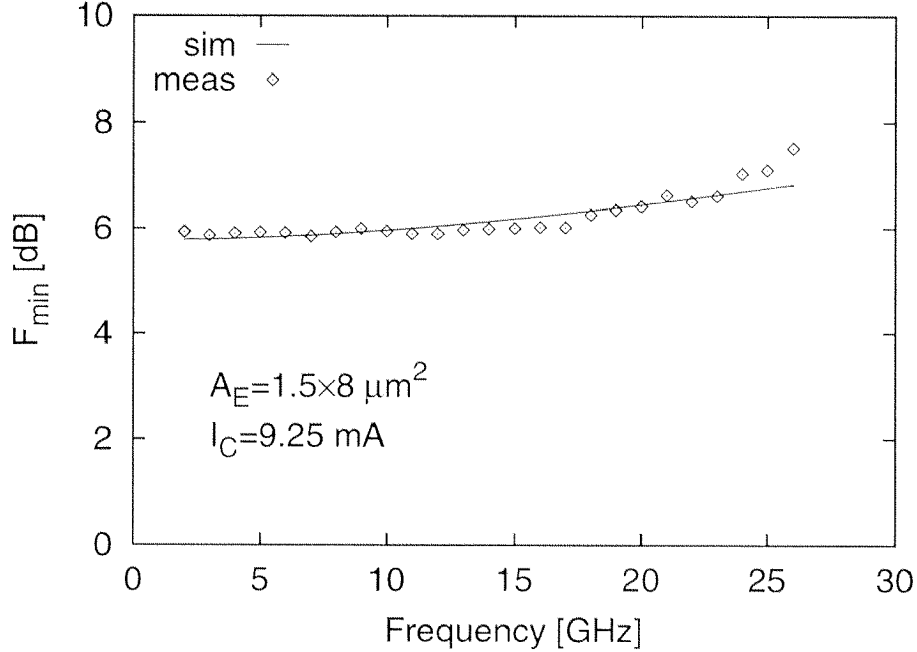
Figure 5.19: *Measured ($\diamond$) and simulated (–) minimum noise figure F_{min} of an HBT with $A_E = 1.5 \times 8\,\mu m^2$, $I_C = 9.25\,mA$ from 2 to 26 GHz*

eter data of the model correspond very well with the measurements which demonstrated that this model is well suitable for small-signal and noise modeling. The values of the small-signal parameters are given in Table 5.5. The table compares the calculated values and the values after fitting of the parameters. The differences between to calculated and fitted values are small enough to say that the final parameters are reasonable.

From the good agreement between measured and simulated S-parameters, we expect that the f_T extrapolated from the measured h_{21} corresponds well with the simulated data. To verify this statement and to extract the base and collector delay times, the total transistor delay ($\tau_{EC} = 1/(2\pi f_T)$) is plotted versus $1/I_C$ in Figure 5.22 for an HBT with base and collector thicknesses of 80 nm and 600 nm, respectively, and an emitter area of $1.5 \times 8\,\mu m^2$. A maximal deviation of τ_{EC} between model and simulation of 0.2 ps is found. According to Eq. (4.3), f_T tends toward $(\tau_B + \tau_C)^{-1}$ for $I_C \to \infty$ respectively $1/I_C \to 0$. The extrapolated value for the sum of the base and collector delays is 1.65 ps. From Eq. (3.1), a base delay of 0.72 ps is obtained, which leads to a collector delay of 0.93 ps. This means that the
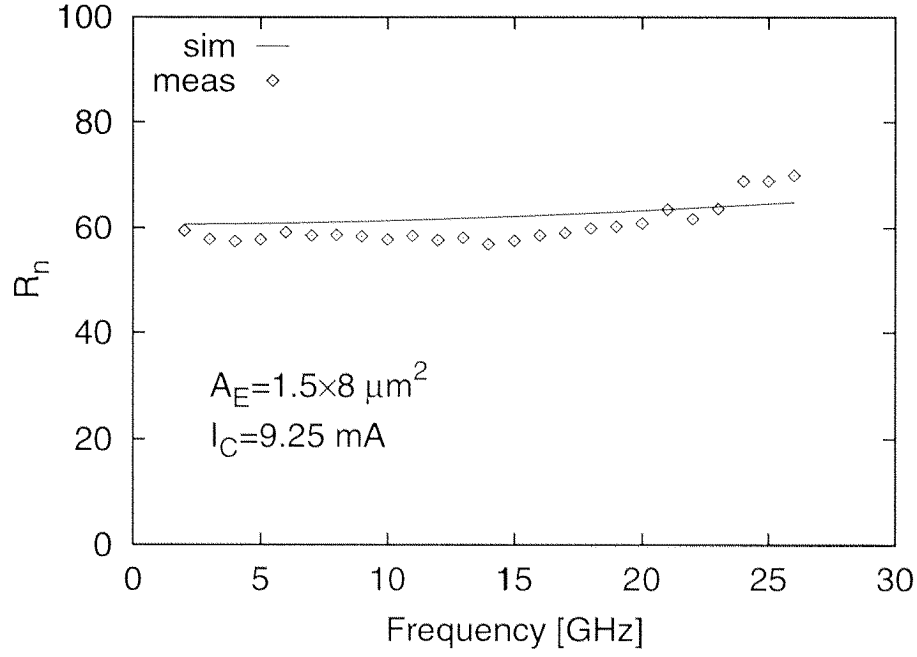
Figure 5.20: *Measured (◊) and simulated (–) noise resistance R_n of an HBT with $A_E = 1.5 \times 8\,\mu m^2$, $I_C = 9.25\,mA$*
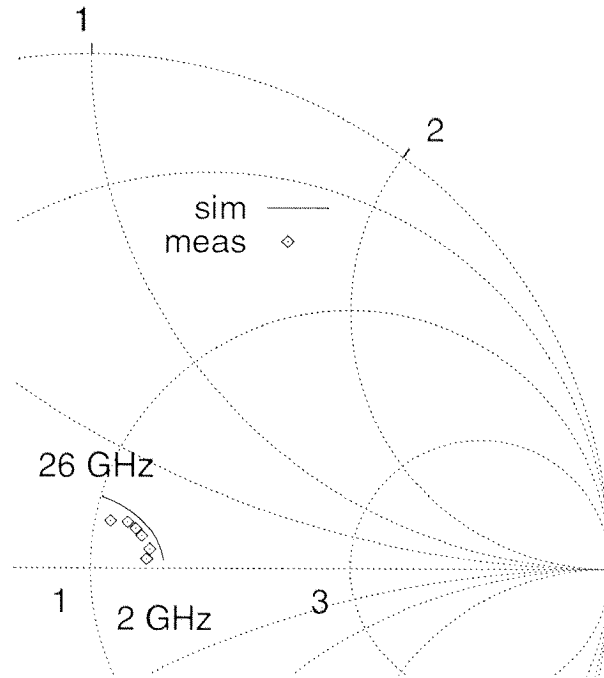
Figure 5.21: *Optimum source reflection factor Γ_{opt} at $I_C = 9.25\,mA$, $A_E = 1.5 \times 8\,\mu m^2$*

velocity of the carriers in the collector is in the overshoot regime ($v_{eff} \simeq 3 \cdot 10^7$ cm/s).

parameter	fit	calc	unit
$r_{bb'}$	28.8	$R_B = 30.1$	$[\Omega]$
r_{bc}	0		$[\Omega]$
r_E	3.8	2.7	$[\Omega]$
r_C	4.1	5.5	$[\Omega]$
r_π	74.9	74.9	$[\Omega]$
c_π	407	$c_d = 347$	$[fF]$
c_{je}	60		$[fF]$
g_m	255	255	$[mS]$
c_μ	5.5	$C_{BC} = 12.4$	$[fF]$
c_{bcx}	8.4		$[fF]$
r_μ	40		$[k\Omega]$
r_0	10		$[k\Omega]$

Table 5.5: *Equivalent circuit parameters of the model for an HBT with* $A_E = 1.5 \times 8\,\mu m^2$, *at* $I_C = 9.25\,mA$ *and* $V_C = 1.5\,V$
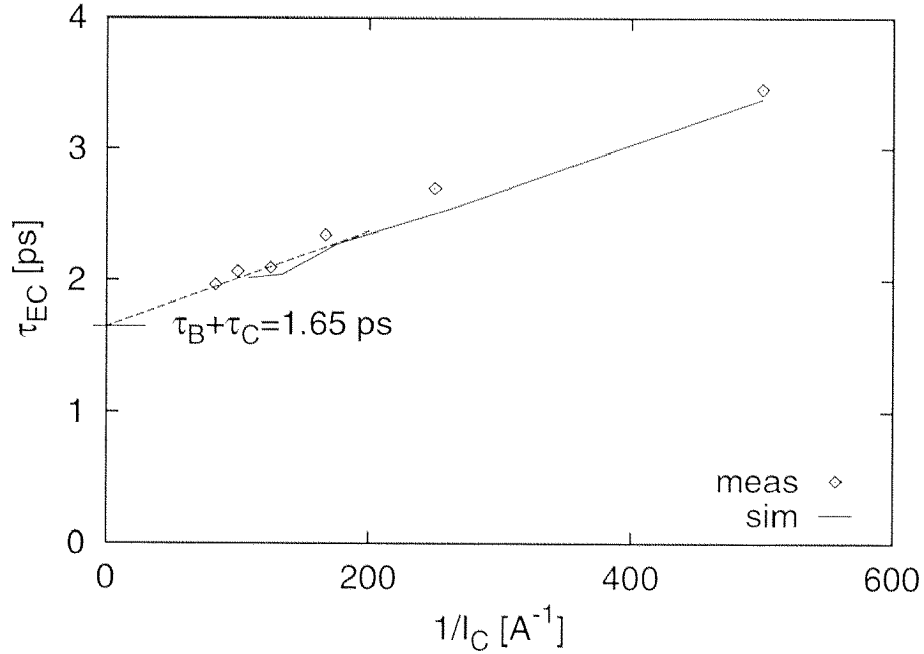
Figure 5.22: *Total emitter-to-collector delay time* $\tau_{EC} = 1/(2\pi f_T)$ *vs.* $1/I_C$, $X_B = 800\,nm$, $X_C = 600\,nm$, $A_E = 1.5 \times 8\,\mu m^2$

In order to investigate the dependences of the noise parameters upon frequency and small-signal parameters, the equivalent model circuit of Figure 5.2 is transformed into conventional representation of a two-port to analyze

noise problems (Fig. 2.2). The HBT can then be considered as a noiseless two-port with two correlated voltage $(\overline{e_n^2})$ and current noise sources $(\overline{i_n^2})$ at its input. The power spectral densities of these noise sources and the correlation result then in [7]

$$\overline{i_n^2} = \overline{i_{nb}^2} + \frac{1}{\beta}\left(1 + \frac{f^2}{f_\pi^2}\right)\overline{i_{nc}^2} - \frac{2}{\beta}\Re\{\overline{i_{nb}^* i_{nc}}\} \tag{5.63}$$

$$\overline{e_n^2} = 4kT(r_{bb'} + r_e) + (r_{bb'} + r_e)^2\overline{i_n^2} + \frac{r_\pi^2}{\beta^2}\overline{i_{nc}^2} \tag{5.64}$$

$$+ \frac{2(r_{bb'} + r_e)r_\pi}{\beta}\left(\frac{1}{\beta}\overline{i_{nc}^2} - \Re\{\overline{i_{nb}^* i_{nc}}\}\right) \tag{5.65}$$

$$\overline{e_n i_n^*} = (r_{bb'} + r_e)\overline{i_n^2} + \frac{r_\pi}{\beta^2}\left(1 - j\frac{f}{f_\pi}\right)\overline{i_{nc}^2} - \frac{r_\pi}{\beta}\overline{i_{nb}^* i_{nc}} \tag{5.66}$$

where $\Re$ and $\Im$ denote the real and imaginary parts, respectively, and f_π is the 3 dB cut-off frequency of the intrinsic current gain which is defined by the differential base-emitter resistance r_π and capacitance c_π

$$f_\pi = \frac{1}{2\pi r_\pi c_\pi} \tag{5.67}$$

The noise parameters F_{min}, R_n, $Y_{opt} = G_{opt} + jB_{opt}$ can be calculated using Eq. (2.6) to (2.9)

$$F_{min}(f) = 1 + \frac{1}{2kT_0}\left(\Re\{\overline{e_n i_n^*}\} + \sqrt{\overline{e_n^2 i_n^2} - \Im\{\overline{e_n i_n^*}\}^2}\right) \tag{5.68}$$

$$R_n(f) = \frac{\overline{e_n^2}}{4kT_0} \tag{5.69}$$

$$G_{opt}(f) = \sqrt{\frac{\overline{i_n^2}}{\overline{e_n^2}} - \left(\frac{\Im\{\overline{e_n i_n^*}\}}{\overline{e_n^2}}\right)^2} \tag{5.70}$$

$$B_{opt}(f) = \frac{\Im\{\overline{e_n i_n^*}\}}{\overline{e_n^2}} \tag{5.71}$$

The power spectral densities of the base and collector noise sources and the correlation between these sources are derived in equations 5.41 to 5.43.

The small-signal parameters depend directly on the conditions as bias point, emitter geometry, and temperature These dependences are investigated in the next sections.

5.3.1 Bias Dependence of the Parameters

A bias dependent noise model is advantageous for LNA applications because the designer can optimize the noise performance of a circuit with respect to the bias conditions. This bias-tuning can be used in conjunction with the traditional input circuit tuning. We have therefore included current-dependent small-signal elements and noise sources. Figures 5.23 and 5.24 the measured and simulated noise parameters at 10 GHz are compared for a device having an emitter area of $1.5 \times 8 \,\mu\mathrm{m}^2$. Besides the bias-dependent
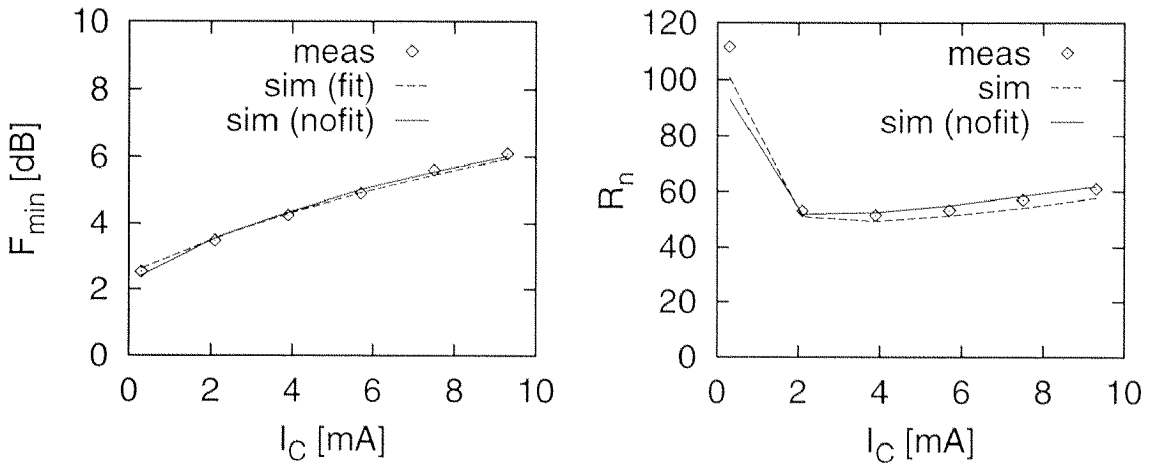
Figure 5.23: *Comparison between the simulated and measured F_{min} and R_n vs. I_C of a device with $A_E = 1.5 \times 8 \,\mu m^2$ at 10 GHz*

model parameters, they have the same values as in Table 5.5. To verify the validity formulas describing the bias dependence of the model, the model elements were fitted only at one bias point ($I_C = 2\,\mathrm{mA}$). Then the base and collector currents, which were obtained from DC measurements, were varied. The dashed curve shows the simulated noise parameters without any further numerical fitting. The good agreement between simulation and measurement proves the quality of our model. We further observe that additional fitting does not improve the correspondence between measurement and simulation.

5.3.2 Geometry Dependence of the Parameters

One of the most difficult task of modeling is to develop a model which is scalable with geometry because parasitic capacitances or an inhomogeneous field distribution do not scale properly with the emitter area. In the Figures 5.25 to 5.28, the simulated and measured noise parameters for different
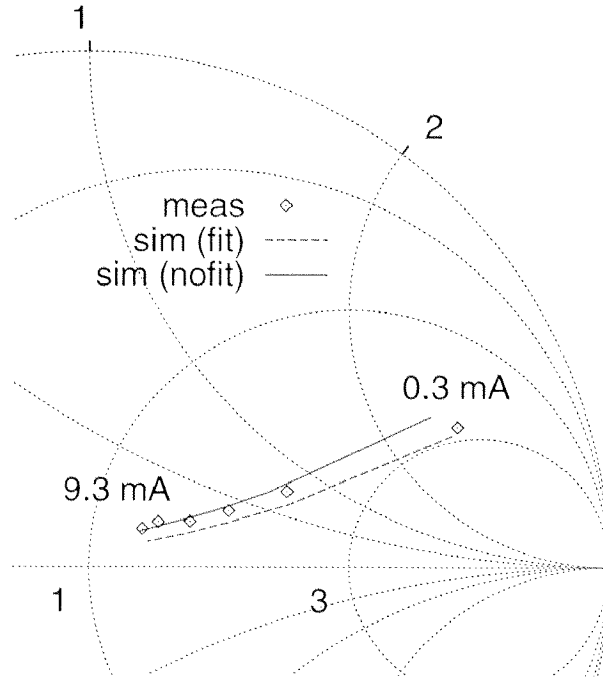
Figure 5.24: *Comparison between the simulated and measured* Γ_{opt} *for* $I_C = 0.3 \dots 9.3\, mA$ *of a device with* $A_E = 1.5 \times 8\,\mu m^2$ *at 10 GHz*

emitter width W_E and emitter length L_E are shown.   We observe good
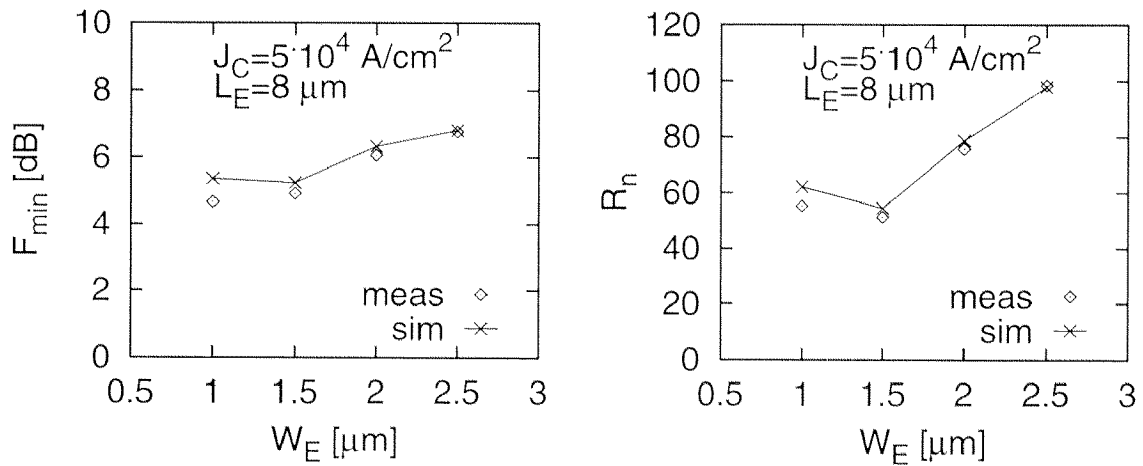
Figure 5.25: *Simulated and measured* F_{min} *and* R_n *vs. emitter width* W_E *of devices with* $L_E = 8\,\mu m$ *at* $J_C = 5 \cdot 10^4\, A/cm^2$ *and* $f = 10\, GHz$

agreement especially for large devices. For smaller device structures, the difference between measurement and simulation become more pronounced. E.g. for a $1.0 \times 8\,\mu m^2$ HBT, the simulated minimum noise figure is 20% higher than the measured. The larger disagreement for smaller devices can
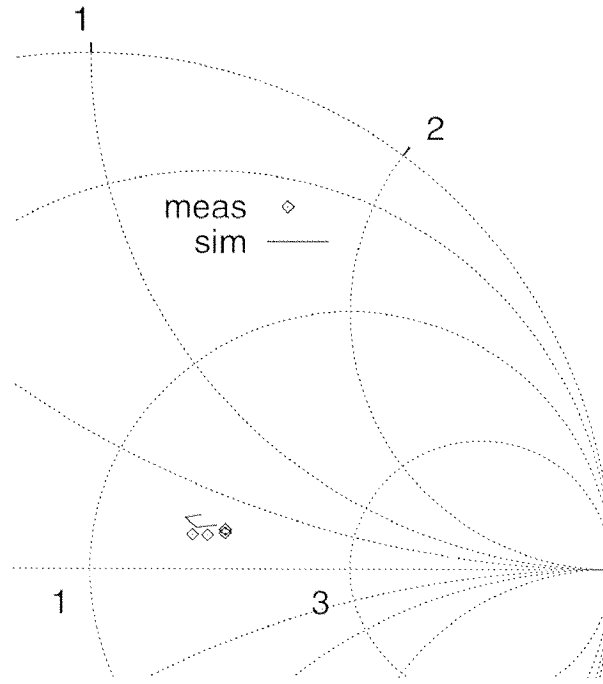
Figure 5.26: *Comparison between the measured and simulated* Γ_{opt} *for emitter widths* $W_E = 0.5\ldots2.5\,\mu m$ *of devices with* $L_E = 8\,\mu m$ *at* $J_C = 5\cdot10^4\,A/cm^2$ *and* $f = 10\,GHz$
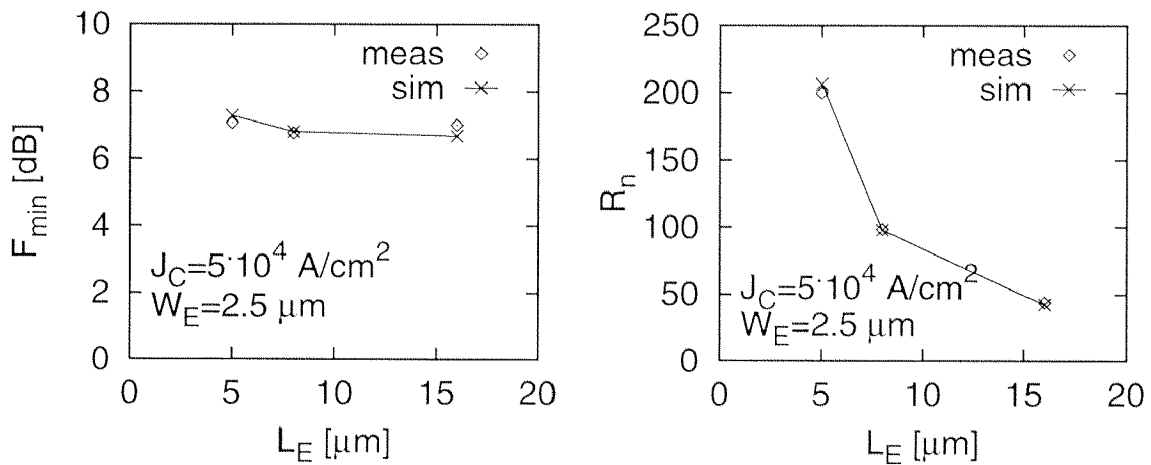
Figure 5.27: *Simulated and measured* F_{min} *and* R_n *vs. emitter length* L_E *of devices with* $W_E = 2.5\,\mu m$ *at* $J_C = 5\cdot10^4\,A/cm^2$ *and* $f = 10\,GHz$

be explained by the fact that influences of parasitics or fabrication tolerances cannot be modeled exactly.

For the selection of the device size and bias point, it can be helpful to investigate the relative contribution of each noise source to the overall noise power. The results for different device sizes operated at two differ-
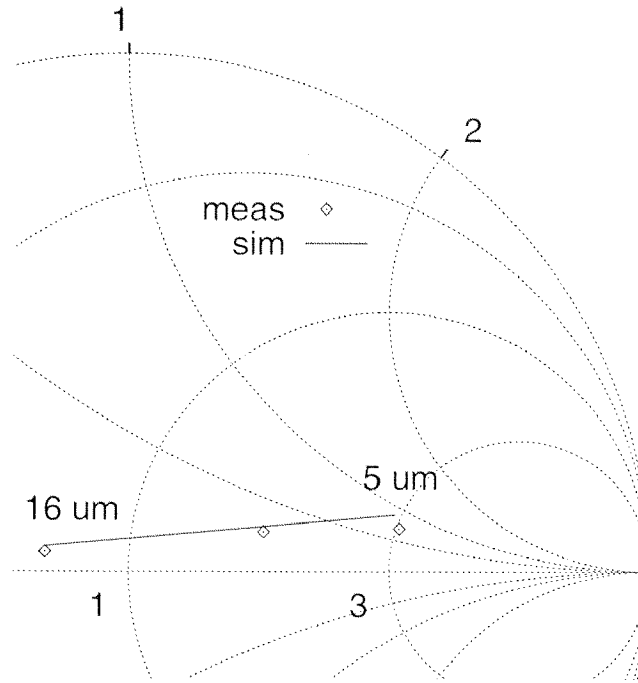
Figure 5.28: *Comparison between the simulated and measured Γ_{opt} for the emitter lengths $L_E = 5 \ldots 16 \, \mu m$ of devices with $W_E = 2.5 \, \mu m$ at $J_C = 5 \cdot 10^4 \, A/cm^2$ and $f = 10 \, GHz$*

ent collector current densities are presented in Table 5.6. At small currents

A_E [μm^2]	J_C [A/cm^2]	u_{nb}	u_{ne}	u_{nc}	i_{nb}	i_{nc}
1.0×8	$1.75 \cdot 10^4$	28 %	15 %	0 %	30 %	27 %
	$7.75 \cdot 10^4$	16 %	5 %	0 %	63 %	16 %
1.5×8	$1.75 \cdot 10^4$	32 %	10 %	0 %	31 %	27 %
	$7.75 \cdot 10^4$	21 %	5 %	0 %	57 %	17 %
2.5×8	$1.75 \cdot 10^4$	37 %	4 %	0 %	40 %	19 %
	$7.75 \cdot 10^4$	17 %	1 %	0 %	61 %	21 %

Table 5.6: *Relative noise contribution of the noise sources to the output noise power at 10 GHz*

($J_C = 1.75 \cdot 10^4$ A/cm^2), the thermal noise sources of the series resistances constitutes 40 % and the current noise sources 60 % of the total noise power. At higher currents ($J_C = 7.75 \cdot 10^4$ A/cm^2) the current noise, above all the base noise current, becomes more and more dominant. Transistors with high current gain are therefore required for low-noise designs.

5.3.3 Temperature Dependence of the Parameters

The device temperature primarily affects the thermal noise of the series resistances of the transistor and the thermal voltage, which modifies the base-emitter characteristics. The former leads to an elevated noise level which can be observed in Figure 5.29. Because the temperature of the substrate is
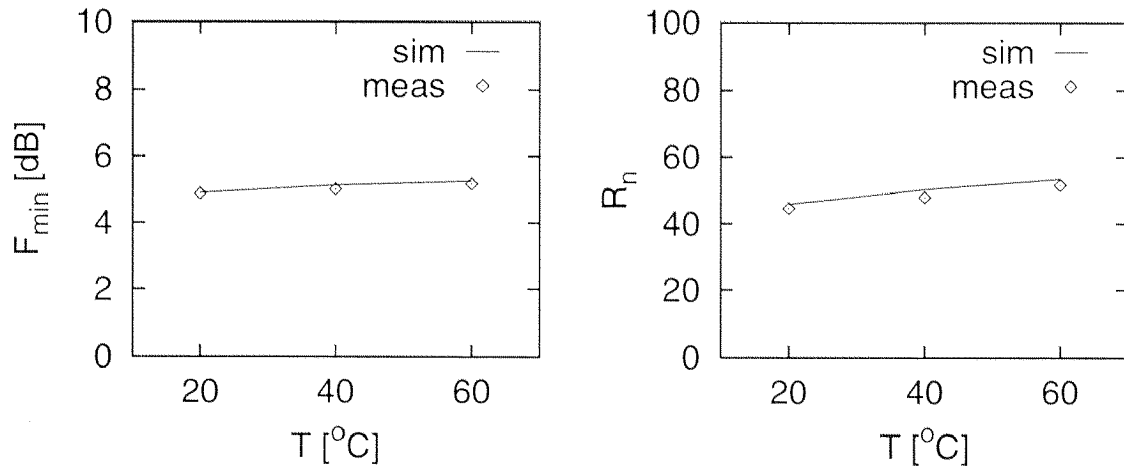
Figure 5.29: *Simulated and measured minimum noise figure* F_{min} *vs. temperature* T *of a device with* $A_E = 1.5 \times 8\,\mu m^2$ *at* $I_C = 6\,mA$ *and* $f = 10\,GHz$

only varied from 20 to 60 °C corresponding to a change of about 14 % in absolute temperature, the increase in noise figure as well as noise resistance is quite small. Our noise model is still valid in this temperature range and can therefore be used for circuit design at slightly elevated temperatures.

5.4 Summary

A scalable noise model which is based on the hybrid-π small-signal model was presented. The thermal noise sources of the base, emitter, and collector series resistance and the low- as well as the high-frequency noise sources are included in the model. We analyzed the high-frequency noise behavior using the analogy between a lossy transmission line and the two processes of diffusion and generation-recombination in the base. An increase with frequency of the spectral noise power of the base current noise can be observed. This frequency dependence should be taken into account in the noise model which will be used for circuit design above $\simeq 40\,GHz$. Above this frequency, the power spectral density of the base noise current is more than

50 % higher than its DC value. The spectrum of the collector current noise remains 'white'. Moreover, the base and collector noise currents show a frequency-dependent correlation. At 40 GHz the magnitude of the correlation factor is 0.25.

The model elements were calculated from technology parameters. The values obtained from these calculations were either directly used in our model or numerical optimization was used to find the final values. The optimization was necessary to take account of influences which are difficult to calculate such as inhomogeneous field distribution in the device, base undercut, distributed resistances or capacitances.

The simulation results are compared with the measurement in the frequency range from 2 to 26 GHz. Moreover, bias point, emitter geometry, and temperature variations of our model were investigated. Good agreement between measurement and simulation results could be observed. Only at small currents and for small device sizes, the model shows differences from the measurement, which proves the potential of our model to be used for RF circuit design.

Chapter 6

Circuit Design

In application such as measurement equipments as well as optical and wireless transmission systems, broadband amplifiers, optical receivers, and oscillators are needed which operate at frequencies higher than 40 GHz. This chapter describes the designs, simulations, and measurement results of a 50 GHz broadband amplifier (Sec. 6.1), a differential 40 Gb/s photoreceiver (Sec. 6.2), and 40 and 60 GHz oscillators (Sec. 6.3) implemented with our InP/InGaAs HBTs. The devices used for the design have a base and collector thickness of 50 nm and 400 nm, respectively (Wafer W_3 in Chapter 4). For more detailed information about the layer structure see Table 3.1. The circuits additionally serve to verify the noise model developed in Chapter 5 in the frequency range (> 26 GHz), where no noise parameter measurements were carried out. Moreover, we investigated the influences of the layout on the circuit performance since they are significant at these high frequencies.

6.1 Broadband Amplifier

The main design goals for broadband amplifiers in communication systems are high gain and large bandwidth. Furthermore, good matching properties to the preceding and following circuits should be provided. For front-end amplifier circuits low-noise behavior is additionally required.

There are mainly two ways to implement broadband amplifiers. They can either be designed as feedback amplifiers or as distributed circuits which

are called traveling wave amplifiers (TWA). In the latter, the transistors are incorporated into an artificial transmission line structures which makes it possible to reach high bandwidths up to the cut-off frequency of the line structure [73]. TWAs using a HEMT technology achieved bandwidths up to 180 GHz [74]. The major drawback of this type of circuits is the large chip area consumption. From the electrical point of view, it is disadvantageous that distributed amplifiers do not operate from DC. Furthermore, bipolar devices are not suitable for TWAs due to the resistive characteristic of their base-emitter junction and the therewith related losses. Thus, we decided to design a feedback amplifier. In these circuits, the feedbacks serve to trade gain for bandwidth. The intended specifications are listed in Table 6.1. The

gain (S_{21})	$> 10\,\mathrm{dB}$
$-3\,\mathrm{dB}$ bandwidth	$> 50\,\mathrm{GHz}$
return losses (S_{11}, S_{22})	$< -10\,\mathrm{dB}$

Table 6.1: *Intended specification for the amplifier design*

gain and bandwidth specifications are state-of-the-art values for broadband amplifiers using HBT-technologies [75, 76, 77], but specifications for the return losses are seldomly reached by those circuits.

6.1.1 Design

We investigated four different topologies of feedback amplifier stages to find a satisfactory solution for our design. As shown in Figure 6.1, these topologies are a common emitter (CE), a Darlington, a common collector common emitter (CC-CE), and a cascode stage. The selection of the amplifier topology is primarily based on the following criteria. The amplifying stage, without the feedback resistor R_f, should inherently have a high gain-bandwidth product (GBW) in order to be more flexible for finding the optimal gain-bandwidth characteristics. The common emitter stage has a smaller gain than e.g the Darlington stage and smaller bandwidth than the Cascode and will therefore not be suitable for our purpose. Circuits with the remaining three topologies were designed and fabricated. An unacceptable overshoot in the frequency response of the gain curve ($>$ 3 dB) was observed the CC-CE and the cascode stage. This behavior can be explained as follows. The base of the cascode stage, respectively the collector of the common collector stage should be properly grounded. If this is not the case, the circuits tend to be instable. A further problem of the cascode stage arises

CE   Darlington   CC-CE   Cascode
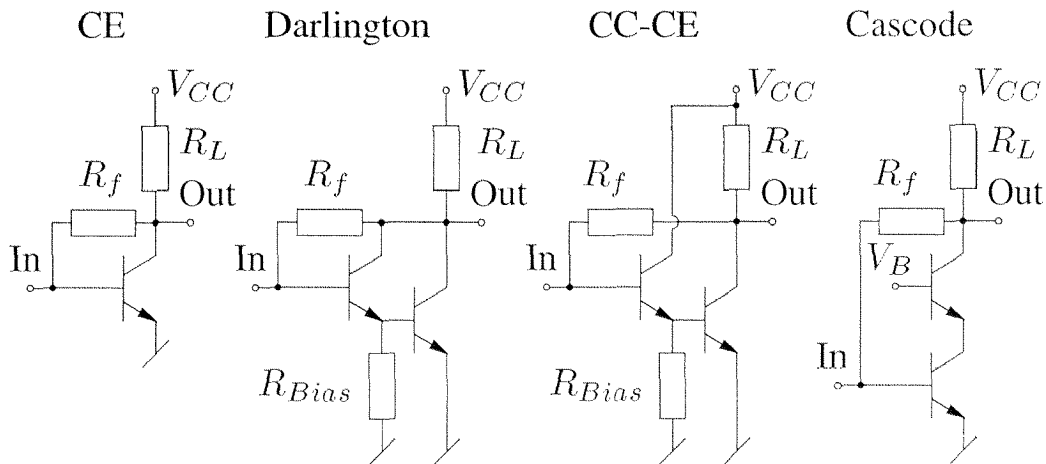
Figure 6.1: *Basic feedback amplifier stages which were investigated: common emitter (CE) stage, Darlington stage, common collector common emitter (CC-CE) stage, Cascode stage*

from the feedback R_F in parallel with the common base and common emitter stages because both stages introduce a phase shift. The sum of these two phase shifts, together with the parallel feedback, leads to stability problems. The Darlington stage does not have these difficulties and also provides high open loop gain. This topology is therefore optimal for our design.

In addition to the gain-bandwidth performance, the circuit should show good input and output matching properties in combination with a good input noise match. An additional feedback path will make this requirement achievable. A schematic of the circuit is depicted in Figure 6.2. This topol-
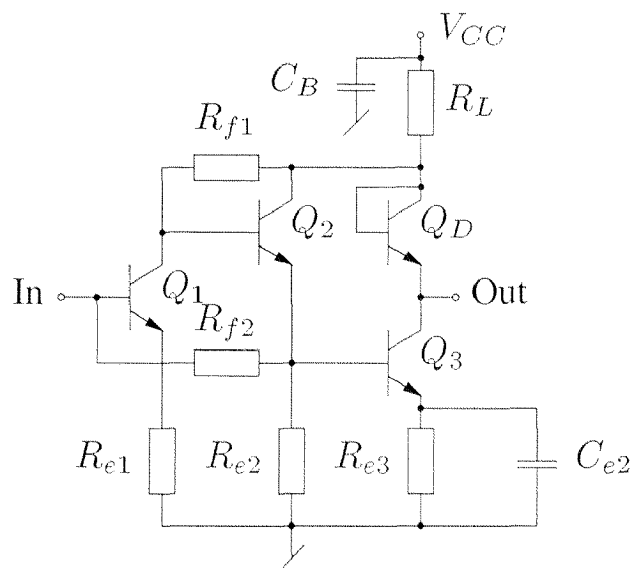
Figure 6.2: *Schematic of the multiple feedback Darlington amplifier*

ogy has originally been demonstrated in [78] for Si-BJT and in [79] for GaAs HBT low-noise amplifiers. The first stage (Q_1) acts as low-noise common emitter amplifier stage which determines most significantly the overall noise figure of the amplifier. The second stage (Q_2 and Q_3), the Darlington feedback amplifier, provides wideband gain and output drive capability. The bandwidth characteristic of the Darlington feedback stage can therefore be optimized by changing the series and parallel feedback resistors without degrading the noise of the overall amplifier. The shunt feedback resistor R_{f1} of the Darlington stage can be adjusted for gain-bandwidth performance. R_{f1} also provides a current path for biasing the HBT Q_1 of the first stage. The shunt feedback resistor R_{f2}, connected between the emitter of transistor Q_2 and the base of transistor Q_1, can be adjusted to change the effective impedance looking out of the base of transistor Q_1 toward the source, and therefore, optimized for minimum noise match. In addition, R_{f2} provides RF shunt feedback which impacts the gain-bandwidth response and determines the input impedance match of the amplifier to $50\,\Omega$. Thus, the feedback resistor R_{f2} can be adjusted to obtain an optimal noise figure as well as an optimal input return loss performance. All transistors are connected to emitter series resistors which are used for further tuning of the frequency response. Moreover, resistor R_{e2} serves as current path for the biasing the transistor Q_2. The resistors R_{e1} and R_{e3} provide a stabilization of the bias point of the transistors Q_1 and Q_3, respectively.

The design of the amplifier is carried out with measured S-parameters files of the devices. The S-parameter data of the HBTs have to be available for all bias point which the transistors are operated at. For simplicity, only transistors with an emitter area of $1.0 \times 8\,\mu m^2$ were used. The determination of the bias points was carried out by simulations using a SPICE-model of these transistors. The SPICE-models could not be used for the simulation of the RF behavior of the amplifier because the models available at this time were not accurate enough at high frequencies. The tool which was used for all the simulations was HP ADS [61]. The influence of the layout was taken into account by introducing microstrip lines as connections between the circuit elements. Critical part of the layout were simulated using Sonnet [80], a method of moments simulator. Figure 6.3 shows a chip photograph of the amplifier.

The complete area of $550 \times 640\,\mu m^2$ is determined by the pad frame which is given by the probe tips for the measurement. The circuit itself only occupies a small part of the total area. A large on-wafer blocking capacitor of $14\,pF$ serves to provide a stable power supply voltage.
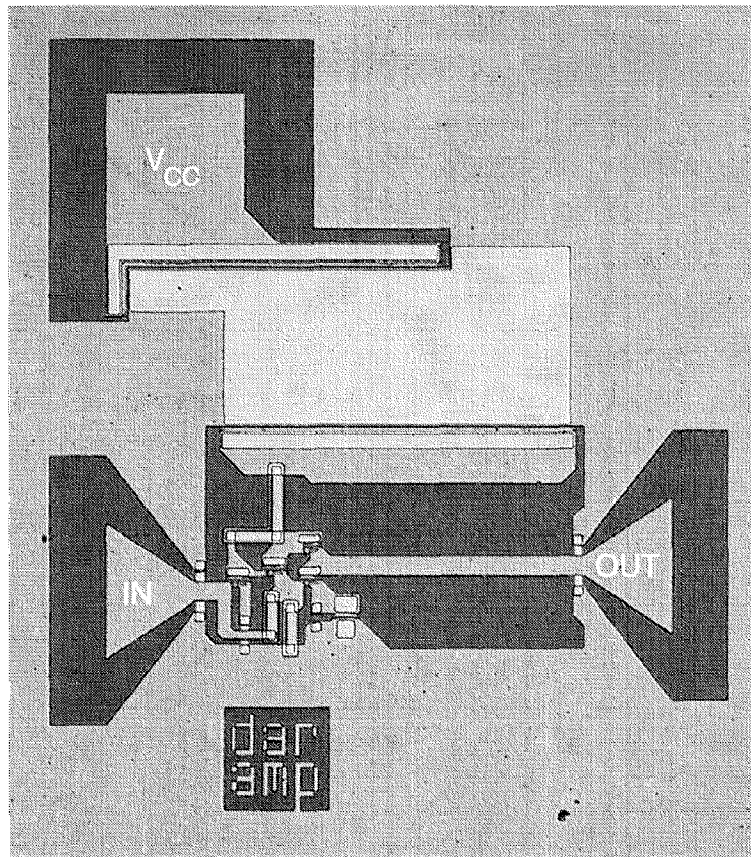
Figure 6.3: *Chip photograph of the amplifier occupying a chip area of* $550 \times 640 \, \mu m^2$

6.1.2 Simulation and Measurement Results

An analysis of the gain, matching, noise, and linearity characteristics is carried out. The RF S-Parameters were measured on-wafer from 0.045 to 75 GHz. The amplitude and phase of S_{21} as well as the group delay are depicted in Figure 6.4. The amplifier reaches a gain of 9.8 dB and a −3 dB-bandwidth of 50 GHz at a supply voltage of 10 V. These results are comparable with amplifier circuits using more complex device structures and technologies [77, 81]. A problem which often occurs using feedback amplifiers is a gain peak in the frequency response. In our design, this peak could almost be avoided. The gain-peaking remains below 1.2 dB which is considerably lower than in other works [76, 75] with similar gain-bandwidth performances.

Especially for the transmission of digital or pulse signals, a linear phase characteristic, corresponding to a constant group delay, is required. The
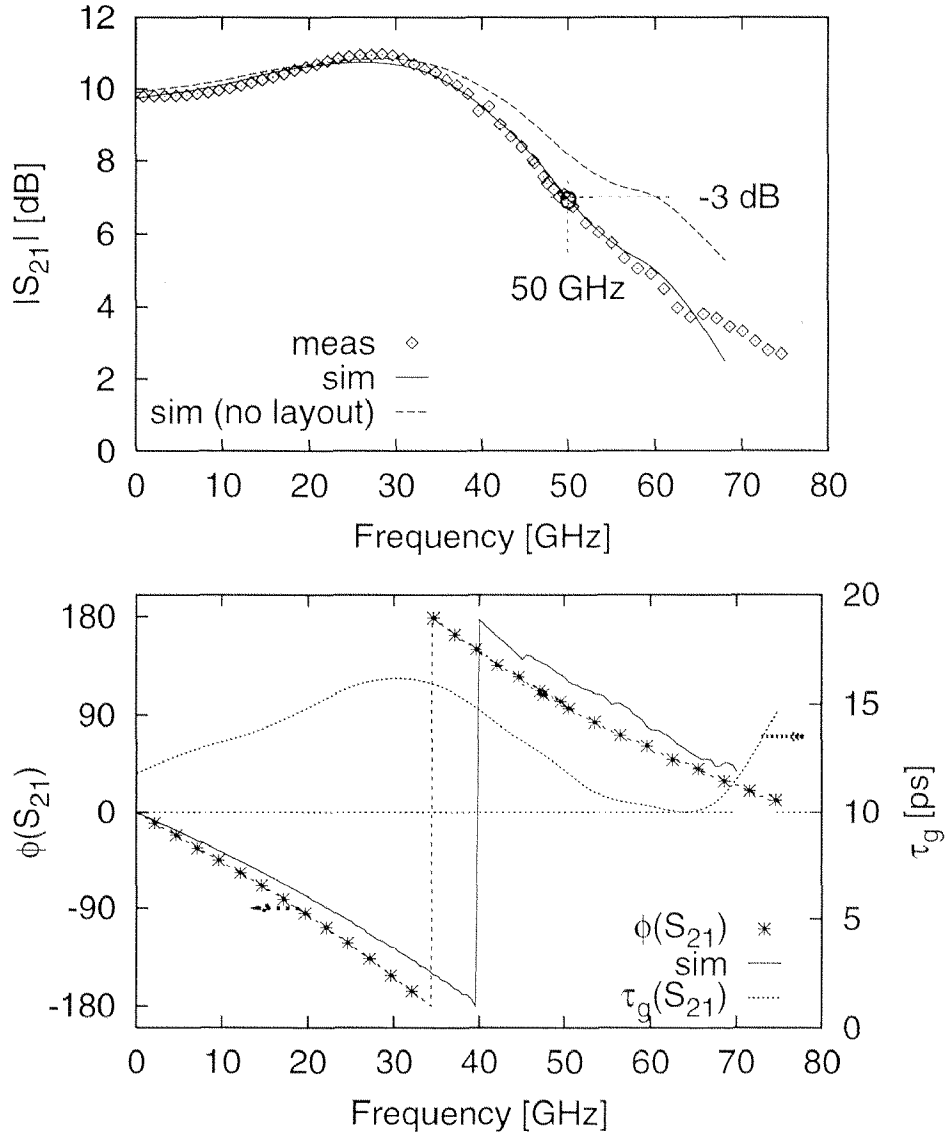
Figure 6.4: *Measured and simulated amplitude, phase ϕ, and group delay τ_g of the gain S_{21} of the multiple feedback amplifier*

group delay which is defined as

$$\tau_g = \frac{d\phi}{d\omega} \tag{6.1}$$

indicates how much the signals of different frequency components are delayed when passing through the amplifier. The group delay of the this circuit is almost constant, resulting in a value of 12.5 ps with a variation of only ±2.5 ps. Using the S-parameter measurement data, time domain simulations lead to an overshoot in the step response of about 7 %.

We further compared the measurement and simulation results and inves-

tigated the influence of the layout. A very good agreement is obtained if all the layout influences are taken into account. Without considering the layout an over-estimation of the bandwidth of more than 10 GHz is observed which demonstrates the importance of including the layout influences when designing high-frequency circuits.

The input and output return losses S_{11} and S_{22} are presented in the Figures 6.5 and 6.6. In the frequency range up to 50 GHz, their magnitudes
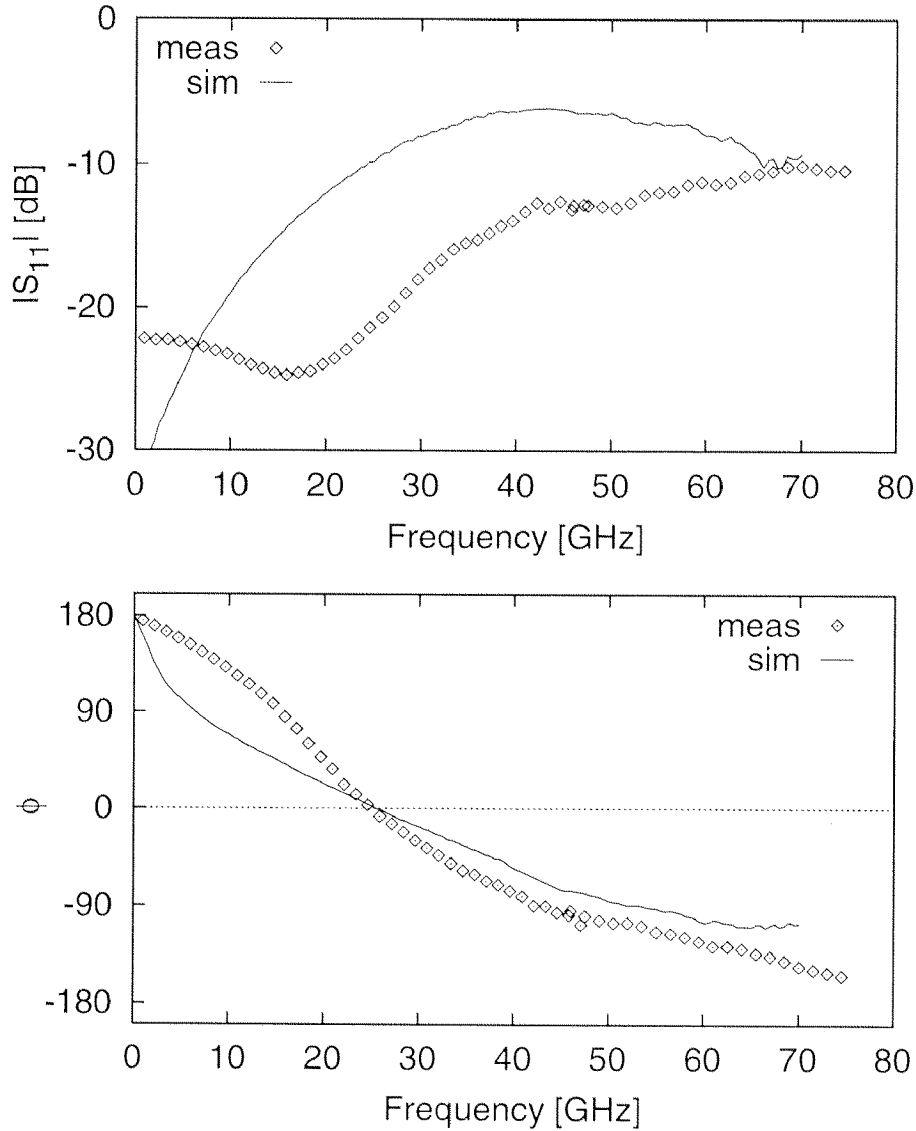
Figure 6.5: *Measured and simulated amplitude, phase of the input return loss S_{11} of the multiple feedback amplifier*

are below -12 dB and -13 dB. Up to 25 GHz the return losses are even better than -20 dB. These are very good values and therefore, the amplifier is well suitable to be used in a 50 Ω system. For the return losses, the accor-
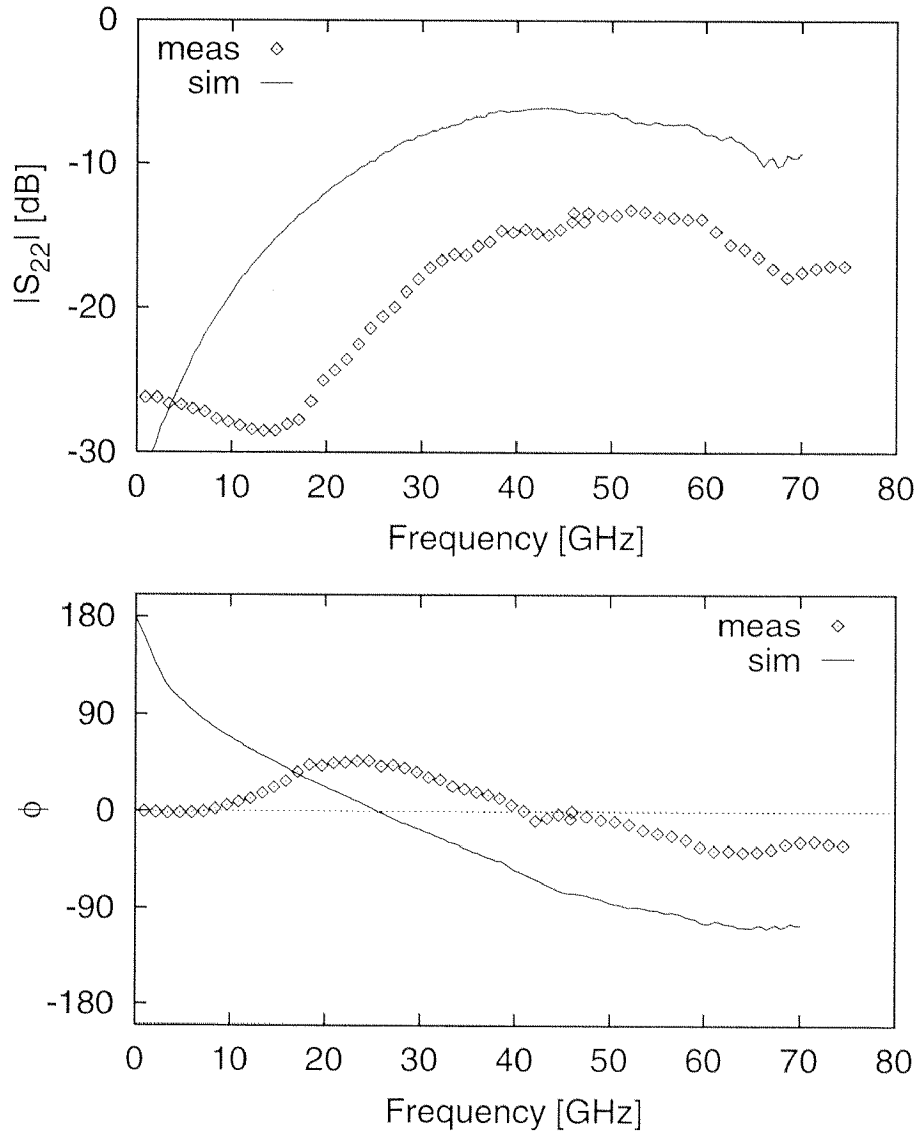
Figure 6.6: *Measured and simulated amplitude, phase of the output return loss S_{22} of the multiple feedback amplifier*

dance between measurement and simulation is not as perfect as for the gain characteristic S_{21}. This may be caused by inaccuracies in the measurements of the phases of the S-parameters. This assumption is based on the fact that when we simulated the amplifier with a line element of 100 μm connected to the input and the output of the amplifier, the discrepancies between the measured and simulated return losses was reduced. Furthermore, the agreement between the measured and simulated phase of S_{21} was improved, which is another indication for inaccurate measurements of the phase.

In Figure 6.7, the measured and simulated noise figures are shown in the frequency range from 2 to 41 GHz, which is a frequency range where

accurate (± 0.3 dB) measurement results can be expected. In this range, the
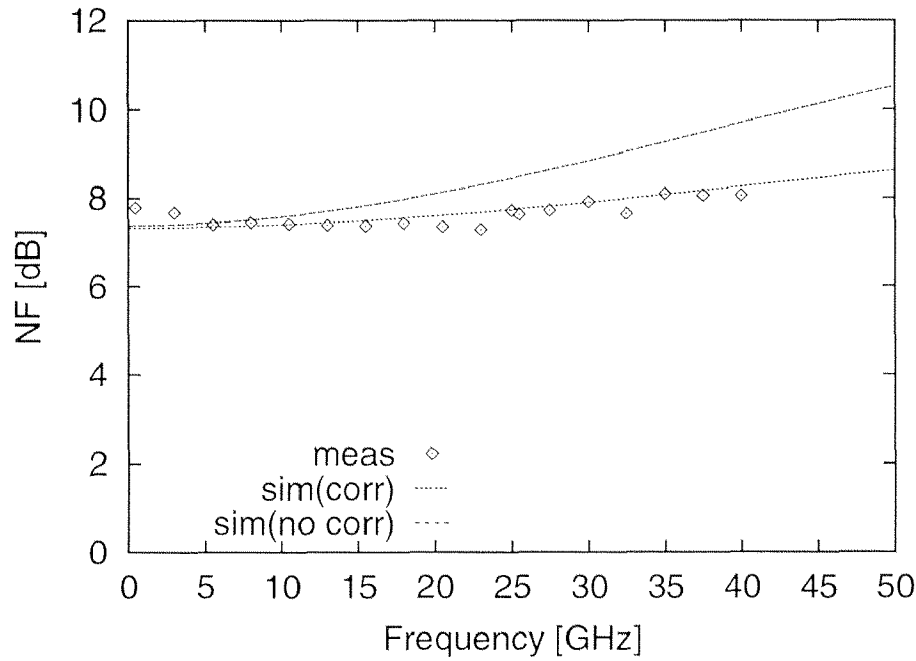
Figure 6.7: *Measured and simulated noise figure of the multiple feedback amplifier, sim_1: with correlation, sim_2: without correlation*

measured noise figure remains between 7.5 and 8 dB. In order to examine the quality of our model, two types of simulation were carried out, one with correlation between base and collector noise currents and the other without. At 40 GHz, a model which does not take account of the correlation predict a noise figure which is 1.5 dB above the measured value, whereas the model with correlation agrees well with the measurement.

For the optimization of the amplifier with respect to noise, the relative contributions of the different noise sources to the overall noise figure F. These contributions can be calculated using an analytic formula for F. For this circuit, a simplified expression for the noise figure F can be derived [79]

$$F(f) = \frac{1}{R_S}\left(R_S + r_b + \frac{1}{2g_m} + r_e\right) \cdot \left(1 + \frac{R_S^2}{R_{f2}^2}\right)$$
$$+ \frac{R_S}{4kT}\left(2qI_B + \frac{2qI_C}{|\beta(f)|^2} + \frac{4kT}{(R_{f1} + R_S)|\beta(f)|^2} + \frac{4kT}{R_{f2}}\right) \quad (6.2)$$

where R_S is the source resistance (50 Ω), r_b, g_m, r_e, and β are the total base resistance, the transconductance, the emitter series resistance, and the small-signal current gain of transistor Q_1, respectively. I_B and I_C are the

base and collector currents of the input transistor and R_{f1} and R_{f2} denote the two feedback resistors of the amplifier. We neglect the correlation between the base and collector noise sources which limits the investigation to lower frequencies. Table 6.2 shows relative noise contributions of the dominant noise sources in the Darlington amplifier. We can see that more

HBTs	Q_1	r_b	16 %	54 %	69 %
		r_e	4 %		
		$2qI_B$	29 %		
		$2qI_C$	5 %		
	Q_2		10 %		
	rest		5 %		
passive network	R_{e1}		13 %		31 %
	R_{f1}		6 %		
	R_{f2}		4 %		
	rest		8 %		

Table 6.2: *Relative noise contribution of the different noise sources in the Darlington amplifier*

than two third (69 %) of the noise originates from the active elements in the circuit and the rest (31 %) from the passive network. We further observe that the dominant noise contributions (54 %) come from the noise sources of the first HBT Q_1. This result corresponds with Friis' formula Eq. (2.11) which says that the first amplifying stage contributes most dominantly to the overall noise. The main noise source of Q_1 is the base current noise source, which makes up 29 % of the overall noise. Hence, for low-noise amplifiers, transistors with high current gains are required, which reduce the base current.

The noise contribution of the amplifier in a 40 Gb/s data transmission can be observed, comparing the input and output eye diagram in Figure 6.8. The setup for the eye diagram measurement is similar to the one described in [82] where the electrical 40 Gb/s NRZ signal was generated by electrical multiplexing 10 Gb/s signals. The opened eye diagram for a PRBS of the length $2^{31} - 1$ at a data rate of 40 Gb/s demonstrates the successful operation of the amplifier in a high speed data transmission system.

The linearity of the amplifier is of great importance as well. Therefore, we measured the third-order intercept point IP_3 and the output power at the 1 dB gain-compression point at different frequency points. Figure 6.9 demonstrates how these two parameters are determined. The 1 dB gain com-

input

38 mV

output

114 mV

12.5 ps
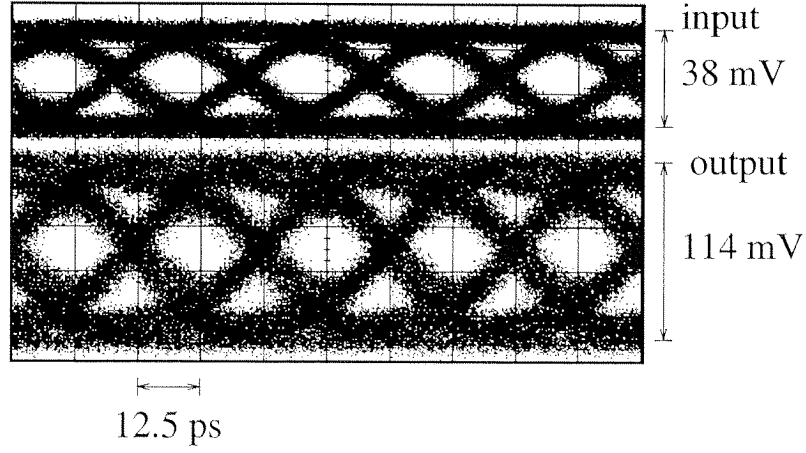
Figure 6.8: *Eye diagrams at the input and output of the amplifier for a 40 Gb/s PRBS of the length $2^{31} - 1$*

$$IP_3 = P_1 + \frac{\Delta}{2}$$
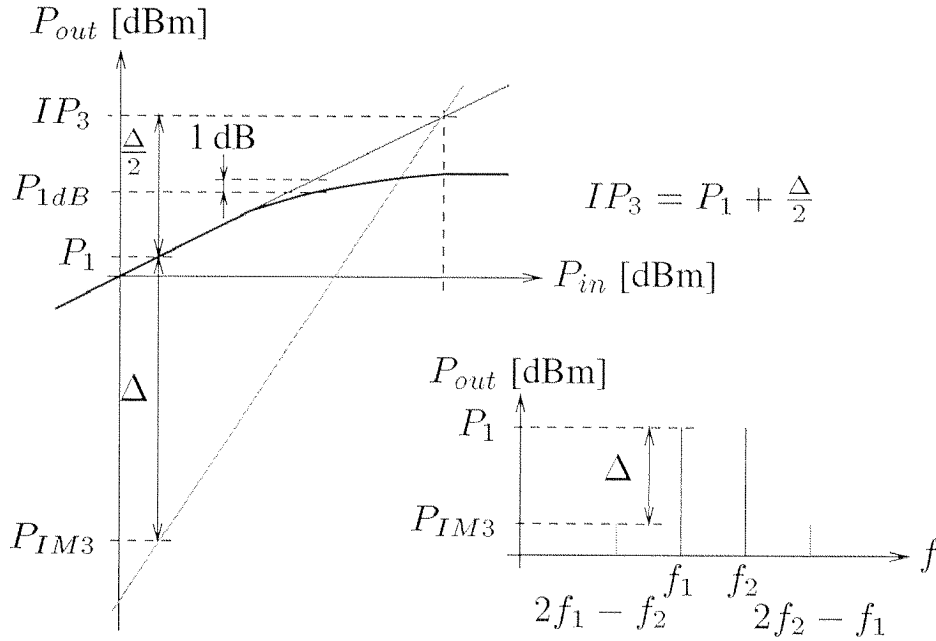
Figure 6.9: *Determination of the 1 dB gain compression point P_{1dB} and the third-order intercept point IP_3*

pression point is the output power P_{out} at which the P_{out} is 1 dB less than for a linear characteristic of $P_{out} = G_P P_{in}$, where G_P is the power gain. The third-order intercept point IP_3 is a measure for the suppression of the intermodulation products. Intermodulation signals with frequencies located near the frequency of the signal of interest are of main importance. To determine the IP_3, we apply a two-tone signal with the frequencies f_1 and f_2 to the input and measure the spectrum at the output. Signals at frequencies of $2f_1 - f_2$ and $2f_2 - f_1$ can be detected. The IP_3 is the output power at which

the power of these intermodulation products (P_{IM3}) equal the power of the signals with the frequencies f_1 and f_2 (P_1). As shown Figure n 6.9, IP_3 can be calculated from the difference of the output powers ($P_1 - P_{IM3}$). When we compare the output power IP_3 with the characteristic of P_{out} vs. P_{in}, we find out the power of IP_3 can not be reached.

Figure 6.10 shows that the IP_3 varies from 17 dBm at 2 GHz to 10 dBm at 50 GHz. In the same frequency range, the 1 dB compression at the output
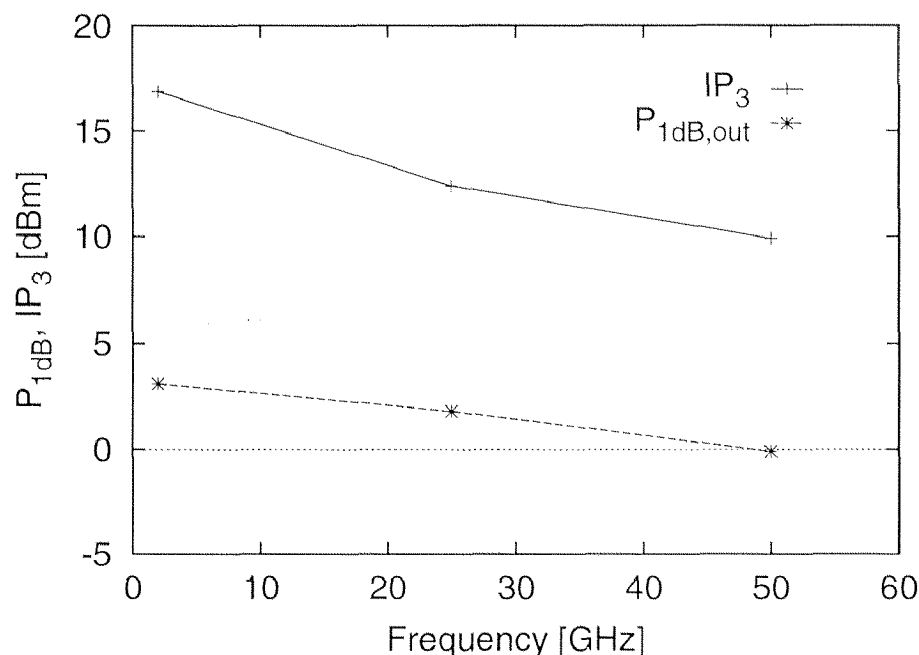
Figure 6.10: *Measured output powers of the third-order intercept point and the 1 dB gain compression point of the multiple feedback amplifier*

changes from 3 dBm to 0 dBm corresponding to an output voltage swing of 890 mV$_{p-p}$ and 630 mV$_{p-p}$, respectively.

6.2 Differential Photoreceiver

Next generations of fiber-optical transmission systems require high gain and high bandwidth photoreceivers. Approaches using packaged modules for 40 Gb/s [83] and monolithic OEICs for 20 Gb/s [84] were already reported for high-gain photoreceivers in HEMT technologies.

Previous investigations in the fields of photoreceiver design [42] and differential amplifier circuits [85] demonstrated the potential of our HBT

technology for the realization of a high-gain photoreceiver with differential outputs.

6.2.1 Design

The block diagram of the differential photoreceiver consisting of a photodiode, a transimpedance amplifier and a post-amplifier is depicted in Figure 6.11. The topology of the implemented transimpedance pre-amplifier
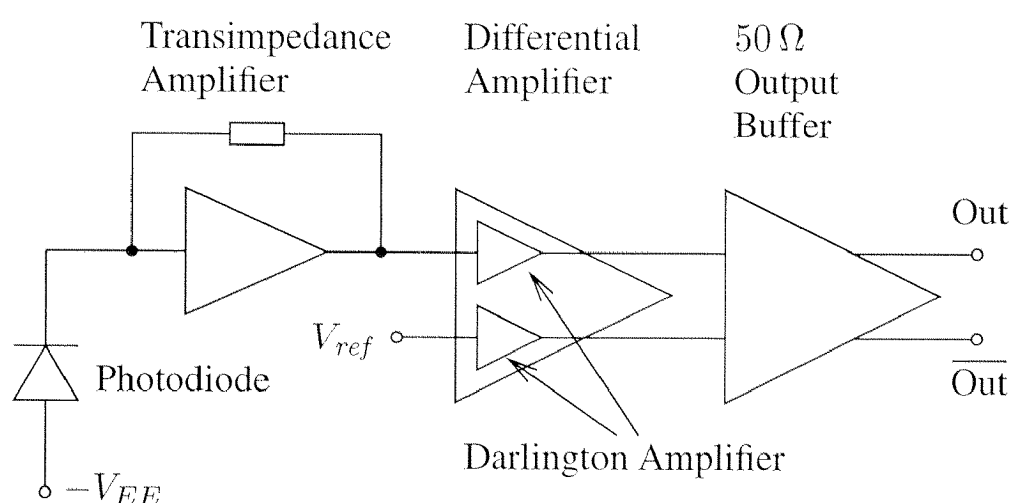
Figure 6.11: *Block diagram of the differential photoreceiver consisting of a photodiode, a transimpedance pre-amplifier, and a differential post-amplifier with a 50 Ω output buffer*

has originally been published in [86] and the capability as a high-frequency photoreceiver was demonstrated up to a bandwidth of 46 GHz in [42, 87]. One major advantage of this concept used in this circuit is the low input impedance ($|Z| < 30\,\Omega$) of the common base input stage which relaxes the problem of the RC speed limitation caused by the depletion capacitance of the photodiode and the input impedance of the pre-amplifier.

The differential post-amplifier consists of an amplifying stage and a 50 Ω output buffer. This output buffer is a differential stage with emitter feedback resistors, whereby the amplifying stage uses a multiple feedback topology in each branch, as described in Section 6.1. The chip photograph of the monolithic integrated photoreceiver consisting of photodiode, pre-amplifier and post-amplifier is shown in Fig. 6.12.
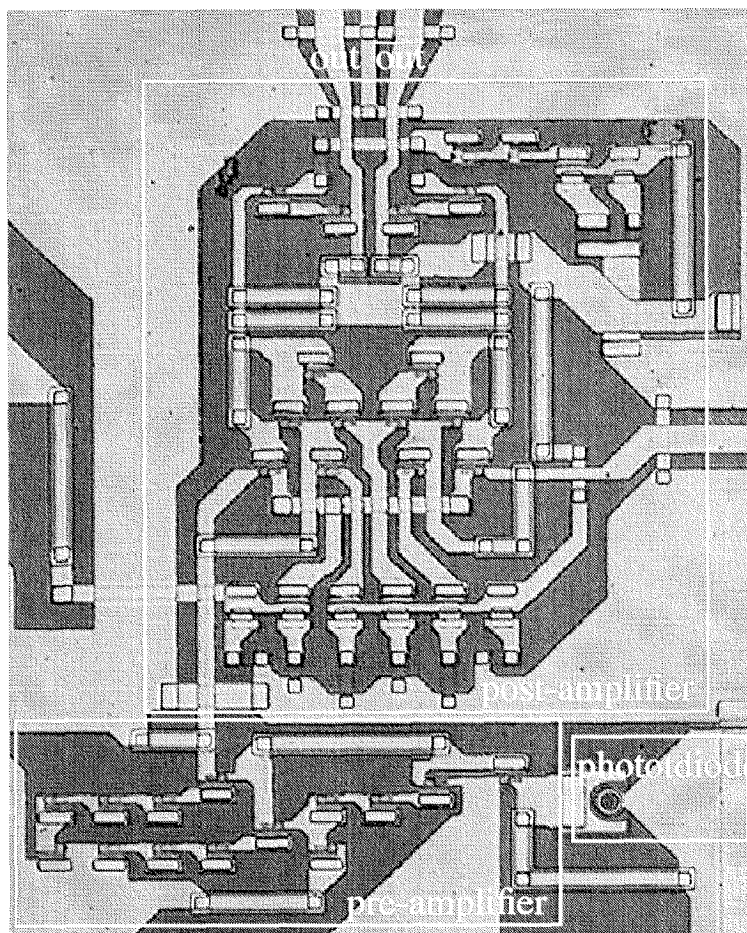
Figure 6.12: *Chip photograph of the differential photoreceiver*

6.2.2   Simulation and Measurement Results

The total transimpedance of the photoreceiver was determined from on-wafer electrical/electrical S-parameter measurements in single-ended mode. Differential-mode operation doubles the transimpedance gain measured in the single-ended mode and results in 3.3 kΩ. For the optical characterization, we used a lensed single-mode fiber for top illumination of the photodiode with light of the wavelength of 1.55 μm.

We determined the optical/electrical frequency response of the photoreceiver from fs-pulse response measurements. The output signal shown in Figure 6.13 exhibits a full width half maximum (FWHM) pulse width of 19.7 ps. To obtain the gain bandwidth characteristic, the pulse response is Fourier-transformed. Deconvolution of the response of the measurement setup is used to cancel its influence. This procedure leads to the optical/electrical frequency response depicted in Figure 6.14. We derive a -3 dB bandwidth of 28 GHz, resulting in a gain-bandwidth product of 92 THzΩ.
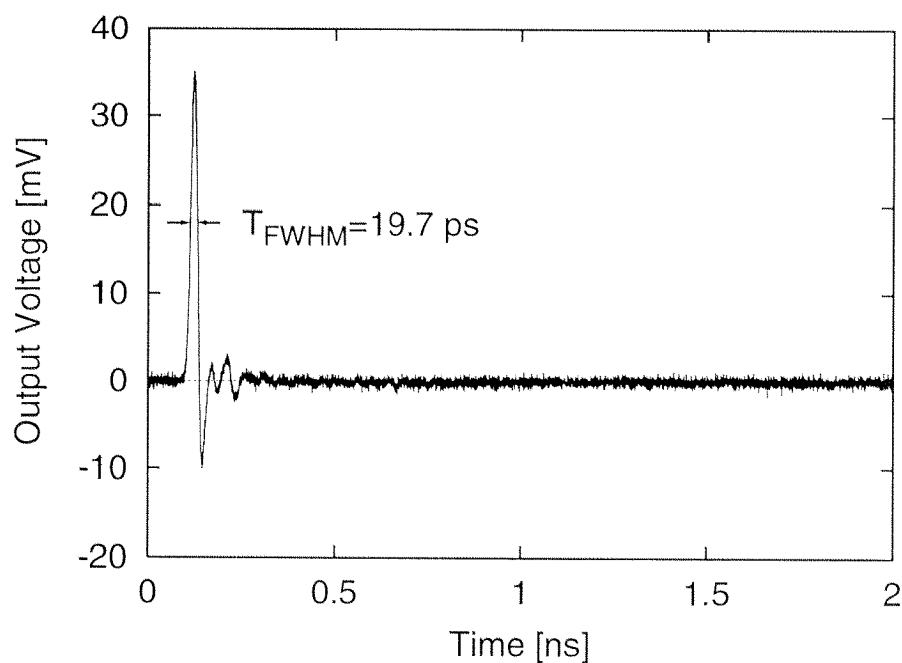
Figure 6.13: *Measured impulse response of the receiver, not corrected for the measurement setup*
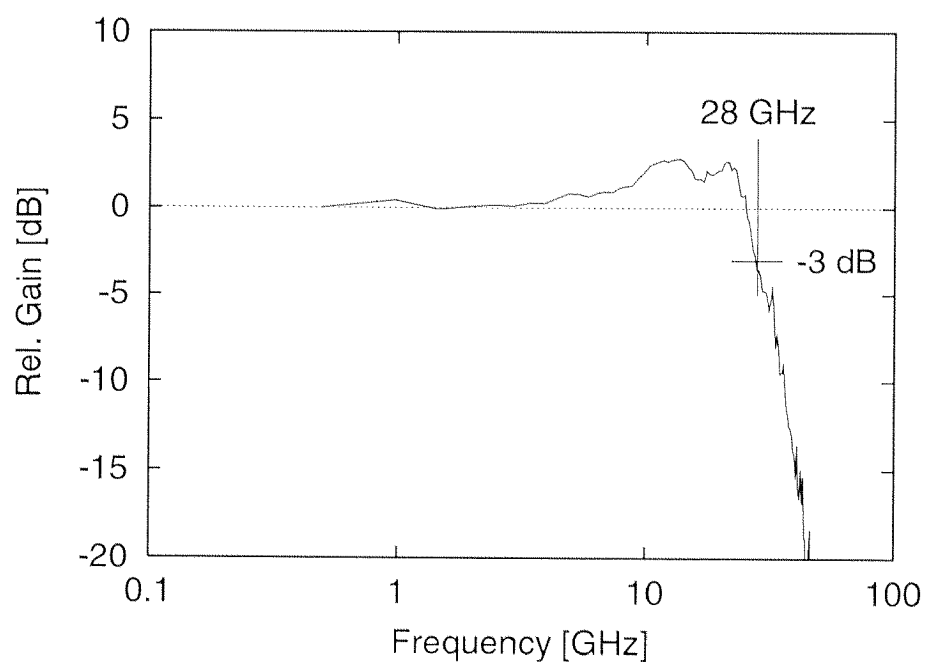
Figure 6.14: *Calculated optical/electrical frequency response of the receiver, corrected for the measurement setup*

Eye diagram measurements were carried out at a data rate of 40 Gb/s with a measurement setup similar to the one described in [82]. The electrical

40 Gb/s NRZ signal was generated by an electrically multiplexed pseudo-random 10 Gb/s signals. As optical source, a DFB diode laser followed by an external Mach-Zehnder modulator and an Er-doped fiber amplifier was used. The eye diagrams of the two differential output voltages of the photoreceiver for a 40 Gb/s pseudo-random bit sequence (PRBS) of the length of $2^{31} - 1$ at an optical power of $500 \, \mu$W are depicted in Figure 6.15. The

T Out
| 250 mV

T $\overline{\text{Out}}$
| 250 mV

12.5 ps
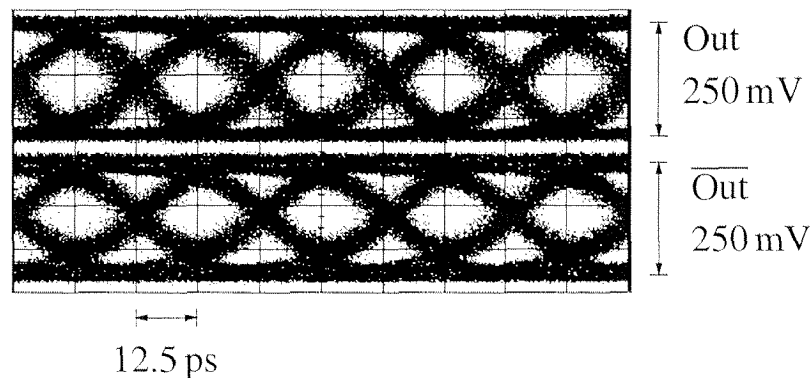
Figure 6.15: *40 Gb/s eye diagram at the inverting ($\overline{Out}$) and non-inverting (Out) outputs of the differential photoreceiver measured for a PRBS of the length of $2^{31} - 1$*

clearly open eyes show the successful operation at this high data rate. Since no bit error rate (BER) tester for 40 Gb/s is currently available, we roughly estimated the sensitivity of our photoreceiver by measuring the output noise for the logical levels '1' and '0'. Using the formula for the BER in presence of Gaussian noise in [40], we can expect, as zero-order estimation, a sensitivity of -14 dBm at a BER of 10^{-9}.

6.3 Oscillator

Oscillators are mainly used in communication systems to generate the carrier signal for the transmission. They are also key-components in clock- and data-regeneration circuits. There exist different principles for the implementation of oscillators. In the lower frequency range, relaxation type oscillators can be used. This circuit type consists of a Schmitt-trigger and of a capacitor which is charged and discharged. The capacitor is charged until the voltage drop over the capacitor reaches the switching-level of a Schmitt-trigger. At this moment, the discharging phase of the capacitor begins until the other switching level is reached. Then, the charging process restarts. This oscillator principle only works up to a few GHz.

At higher frequencies, the oscillation is generated by destabilizing an active device or circuit. RC- or LC- feedback networks connected from the output to the input of the active circuit can be used for the destabilization. The Colpitts and Hartley oscillators are examples for LC-feedback oscillators. For oscillators at highest frequencies, the structure of the circuit should be as simple as possible in order to minimize the influence of parasitic elements in the layout. Negative impedance type oscillators fulfill this requirement optimally and are therefore the type of oscillators we selected for our design.

In this oscillators type, the transistor is connected to a passive circuit element in a way that a negative impedance is generated at one port of the device which becomes unstable. There are two possibilities to reach this situation. A capacitive impedance connected between the emitter and ground generates a negative impedance at the base of the transistor, whereas an inductive impedance between base and ground leads to a negative impedance at the emitter. The circuit connected to the port of negative impedance determines the oscillation frequency.

6.3.1 Design

Two different oscillators with different design principles were implemented. One with a target center frequency of 40 GHz uses lumped elements for the determination of the center frequency, and the other one at 60 GHz is designed with coplanar waveguides.

In the 40 GHz oscillator shown in Figure 6.16, the capacitance C_E of 20 fF connected between the emitter and ground generates the negative impedance at the base. The impedance Z_{in} seen into the base for this configuration can be approximated by (Appendix D.1)

$$Z_{in} \simeq r_{bb'} - \frac{\dfrac{\beta \omega_\beta}{C_E}}{1 + \left(\dfrac{\omega}{\omega_\beta}\right)^2} + \frac{1}{j\omega C_E} \frac{1 + \left(\dfrac{\omega}{\omega_\beta}\right)^2 \dfrac{1}{\beta}\left(1 + \dfrac{C_E}{c_\pi}\right)}{1 + \left(\dfrac{\omega}{\omega_\beta}\right)^2} \tag{6.3}$$

where $r_{bb'}$ is the base series resistance, β denotes the small-signal current gain with its -3 dB frequency ω_β. c_π is the total base-emitter capacitance. In order to enable an oscillation, the real part of the impedance Z_{in} must be at least negative enough to compensate for the base series resistance and the resistive losses in the resonator circuit. This may be more easily achieved if
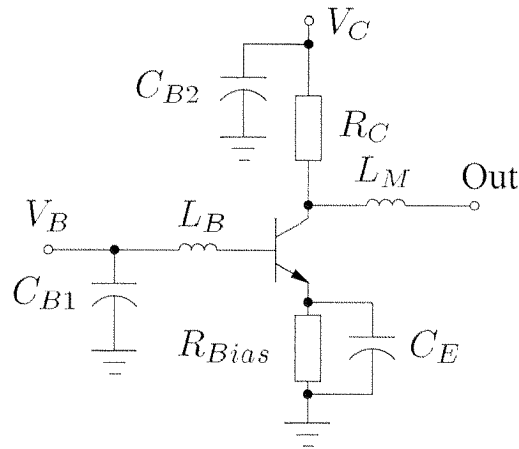
Figure 6.16: *Schematic of the 40 GHz oscillator*

the transistor shows a high β value and high -3 dB frequency of the small-signal current gain which is directly related to the cut-off $(2\pi f_T \simeq \beta\omega_\beta)$. The inductor L_B connected to the base of the HBT and the capacitive part of Z_{in} build the resonator. At the frequency of oscillation, L_B must cancel the imaginary part of Z_{in}. The resistor R_{Bias} connected in parallel to C_E provides a DC path for the bias current of the HBT. The load resistor $R_C = 125\,\Omega$ and the inductor $L_M = 430$ pH serve as output matching circuit. Two capacitors C_{B1} and C_{B2} are the on-chip blocking capacitors for stable power supply voltages.

The 60 GHz oscillator depicted in Figure 6.17 was designed using coplanar waveguides as frequency selecting elements because the parasitics of lumped elements start to dominate at these frequencies. Line elements such
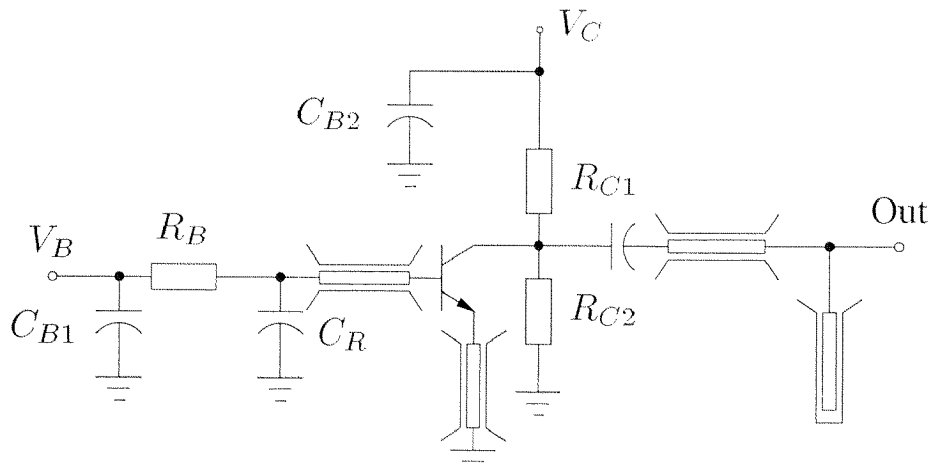
Figure 6.17: *Schematic of the 60 GHz oscillator*

as waveguides and microstrip lines transform at one frequency point either a short or an open into the capacitance or inductance values needed to fulfill the oscillation condition. Coplanar wave guides had to be chosen because no microstrip lines were available in our process although the microstrip lines would provide lower losses. For microstrip lines, an additional metalization layer would have to be introduced.

The negative impedance oscillator can be designed using small-signal analysis. We do therefore not need a large-signal model of our devices. As a consequence of the small-signal design, non-linear effects, as for example amplitude regulation and phase noise, are not considered. For the design we used measured S-parameters of the transistors and inductors because this method should lead to the most accurate simulation results with respect to oscillation condition and frequency. For the coplanar waveguides of the 60 GHz oscillator, models are available in HP ADS. More complex structures as e.g. T-junctions were simulated using Sonnet [80] which calculate the S-parameters of the structure. These S-parameters are then used in the small-signal simulation. Since the layout significantly influences or even determines the circuit performances, the layout had to be created simultaneously with the simulations. The final layouts of the two oscillators are shown in Figures 6.18 and 6.19.
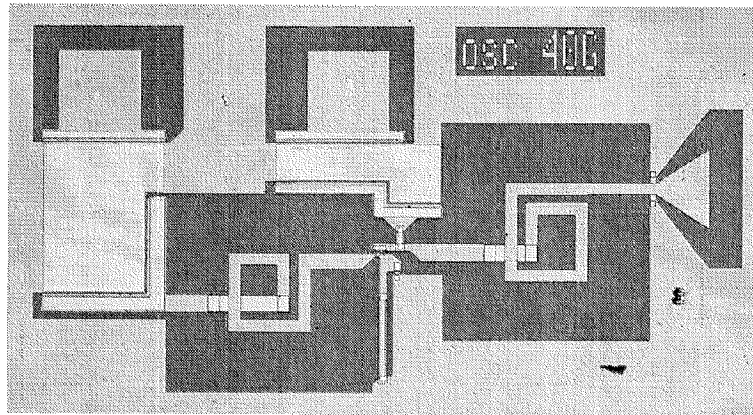
Figure 6.18: *Chip photograph of the 40 GHz oscillator having a chip area of* $0.92 \times 0.52\,mm^2$

6.3.2 Measurements

The spectrum of the 40 GHz oscillator, measured with a HP 8665E spectrum analyzer, is shown in Figure 6.20 A center frequency of 35.55 GHz was
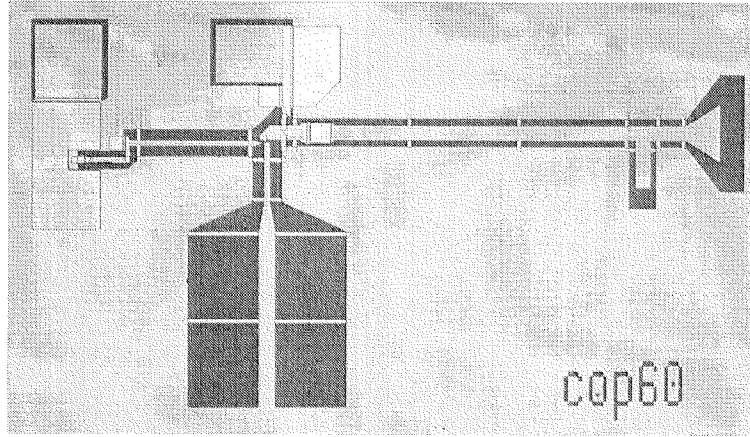
Figure 6.19: *Chip photograph of the 60 GHz oscillator consuming a chip area of* 1.24 × 0.8 mm²
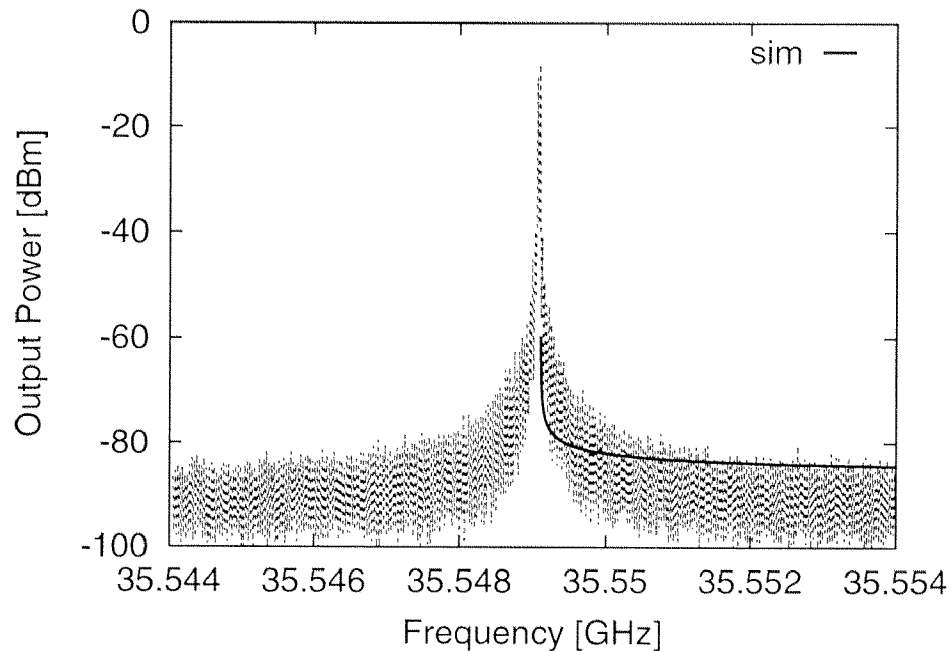
Figure 6.20: *Measured and simulated spectrum of the 40 GHz oscillator, resolution bandwidth: 3 kHz*

measured, instead of the 40 GHz the circuit was designed for. This discrepancy most probably originates from parasitics of the inductors as well as of the resistor which were not taken into account during design. Furthermore, the design method using S-parameters does not include non-linear effects. These effects can modify bias point of the transistor during operation, which potentially leads to a shift in the oscillation frequency. The measured output power of −7.8 dBm had to be corrected due to cable losses which are 7.4 dB

at the oscillation frequency. The resulting value of –0.3 dBm corresponds to a voltage swing of $610\,mV_{p-p}$.

For the measurement of the spectrum of the 60 GHz oscillator depicted in Figure 6.21, we used a pre-selected mixer (HP 11974V) together with the spectrum analyzer HP 8563E. The measured center frequency of 58.18 GHz
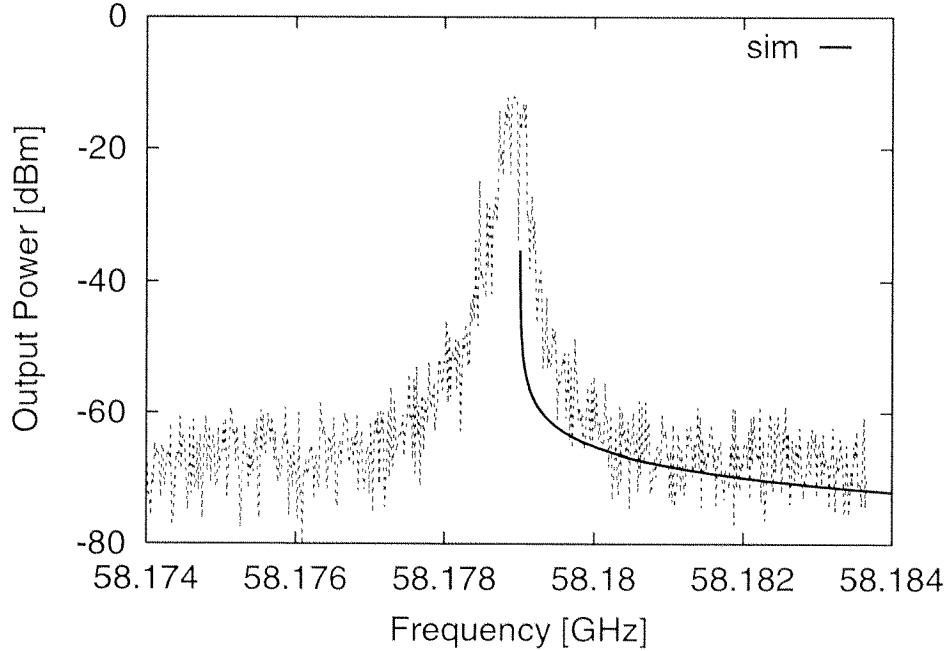
Figure 6.21: *Measured and simulated spectrum of the 60 GHz oscillator, resolution bandwidth: 100 kHz*

corresponds very well with the design frequency, which indicates that the model of the coplanar waveguides are still accurate at these frequencies. The measured output power at the oscillation frequency is –12.2 dBm. Taking the losses of 7.3 dBm of the measurement setup into account, we obtain an effective value of –4.9 dBm ($360\,mV_{p-p}$).

The single-side-band (SSB) phase noise was determined from the spectrum. A value of –112 dBc/Hz at 1 MHz offset was obtained for the 40 GHz oscillator. This phase noise value is comparable with dielectric resonator oscillators (DRO) in this frequency range [88]. The 60 GHz circuit shows a SSB phase noise of –97 dBc/Hz at 1 MHz offset, which is similar to phase noise data of coplanar waveguide oscillators reported in literature [89]. Better values are found for DROs at these frequencies [90].

For the simulation of the phase noise non-linearities of the circuit have to be taken into account. We could therefore not directly use our linear noise model. Hence, we had to include the parameters of the low-frequency noise

sources into a non-linear Gummel-Poon model. In this way, it was possible to use harmonic balance simulations for the phases noise consideration. The curves of the simulation of both oscillators demonstrate that our model predicts the phase noise with an accuracy of about 10 dB.

6.4 Summary

In order to demonstrate the potential of our InP/InGaAs heterojunction bipolar technology for microwave and millimeter applications, three different circuits types were implemented.

A monolithic, direct-coupled feedback amplifier was designed and fabricated using InP/InGaAs SHBT technology. A very flat gain of 9.8 dB and a bandwidth of 50 GHz were achieved. With the input and output return losses being better than −12 dB and −13 dB, respectively, the amplifier provides very good power matching properties. Very good agreement between measurement and simulation can be observed. We demonstrated the operation of the amplifier at 40 Gb/s, whereas the bandwidth, in combination with the linear phase up to 75 GHz, should be sufficient for > 60 Gb/s data transmission.

Based on the successfully designed 50 GHz broadband amplifier and a previously implemented photoreceiver front-end [42], we have designed and fabricated a monolithically integrated 40 Gb/s photoreceiver consisting of a PIN photodiode, a transimpedance pre-amplifier and a differential post-amplifier. The measured optical/electrical −3 dB-bandwidth of 28 GHz allowed a clearly opened eye diagram for 1.55 μm light at 40 Gb/s with a transimpedance of 3.3 kΩ. To the best of our knowledge, our circuit represents the first monolithic 40 Gb/s photoreceivers with differential outputs. Moreover, the high transimpedance is a record value for a receiver operating at this data rate. Simulations showed that our integration concept allows to add a further amplifier stage to fulfill the requirements of any practical 40 Gb/s fiber-optical system.

Oscillator circuits operating at the frequencies of 36 and 58 GHz have been designed. These oscillators show an output power of 0 dBm and − 5 dBm, respectively. The single side band phase noise at 1 MHz offset frequency is −112 dBc/Hz for the 36 GHz oscillator and −97 dBc/Hz for the 58 GHz circuit, respectively.

Chapter 7

Conclusion and Outlook

In this work, we developed a scalable small-signal and noise model of our in-house InP single heterojunction bipolar transistor (SHBT) technology. Furthermore, we demonstrated the potential of this technology for multi-ten gigabit per second circuits and that the behaviors of these circuits are well described by our model.

7.1 Key Issues

In this thesis, the following issues were discussed:

- Development of a model which is scalable with respect to emitter area and can be employed at different bias points and ambient temperatures.

- Including the low-frequency and high-frequency noise sources into one model.

- Implementation of noise sources which can be extrapolated to frequencies above the measurement range of the noise parameters which is limited to 26 GHz. At those frequencies the frequency dependence of the base current noise sources and the correlation between the base and collector current noise sources become relevant.

- Determination of model parameters which are physically reasonable.

- Development of a small-signal and noise model of the HBT which is simple enough for the design of microwave circuits.

- Realization of state-of-the-art amplifiers and oscillators which are additionally used to investigate the quality of our model above 26 GHz.

7.2 Major Developments

In order to analyze the key issues, the following investigation steps were necessary:

- Introduction of frequency-dependent base and collector current noise sources which are determined using the analogy between the diffusion and recombination processes in the base and the signal propagation on a transmission line.

- Consideration of the frequency-dependent correlation of the base and collector current noise sources which become important at higher frequencies.

- Identification of the dominant noise sources of the HBT. This is important for the optimization of the device structure with respect to its noise performance.

- Introduction of the low-frequency noise sources consisting of different components, whereas each of them shows its particular dependence upon emitter geometry, bias point and temperature.

In order to elaborate the background knowledge and measurement data for the development of the model, the following studies had to be carried out. An introduction to the noise theory was given which has addressed the issues of noisy two-ports as well as the physical origin of the fundamental noise sources. The SHBT technology, which was roughly presented, has been completely characterized, i.e. the DC-characteristics, the RF-performance and the low- and high-frequency noise behavior were determined. For the development of the model, it was necessary to carry out all the measurements on devices with different emitter geometries which were operated at different bias points and temperatures. The values of the model parameters were based on physical data obtained from the device layer structures. For a number of parameters, additional numerical optimization had to be used to adjust the parameter values.

7.3 Main Achievements

The principal results can be summarized as follows:

- The simulations with the small-signal and noise model we developed agree well with the measured S-parameters and noise parameters, whereas the values of the model parameters are physically reasonable.

- The model can be extrapolated to higher frequencies than the measurement range, thanks to the inclusion of correlated and frequency-dependent base and collector current noise sources.

- A monolithically integrated broadband amplifier was implemented with very good gain-bandwidth performance and input and output matching properties, i.e. a -3 dB bandwidth of 50 GHz, a gain of 9.8 dB, and $|S_{11}|$, $|S_{22}| < 12$ dB. This circuit was also used to verify the noise model up to 40 GHz.

- Design and fabrication of a monolithically integrated 40 Gb/s photoreceiver consisting of a photodiode, a transimpedance pre-amplifier, and a differential post-amplifier was carried out. The optical/electrical -3 dB bandwidth of 28 GHz together with the total transimpedance gain of 3.3 kΩ result in a record gain-bandwidth product of 92 THzΩ.

During this thesis a detailed investigation of the noise behavior of our in-house InP SHBT technology was carried out. The development of our model is a contribution in terms of describing the noise properties of HBTs in the low-frequency as well as in the microwave range. The results achieved with respect to the agreement between measurement and simulation are excellent and prove therefore that our model is an optimal candidate to be employed for the design and optimization of RF circuits.

7.4 Outlook

The noise model developed in this work has been demonstrated to be very useful for small-signal design methods, but we cannot describe non-linear effects. It is therefore highly desirable to implement the correlated and frequency-dependent base and collector current noise sources in a non-linear model. At present, no non-linear model, such as SPICE Gummel-Poon, Mextram, or VBIC, offers the possibility to include this feature.

Although very good agreement between simulation and measurement has been achieved, further refinements of the model are desirable. Especially, a more detailed investigation of the influence on the noise behavior caused by the heterojunction as well as the base transport are interesting issues. Moreover, detailed studies of the low-frequency noise, e.g using un-passivated devices and devices with a larger range of the emitter areas, can serve to locate the noise sources more precisely as well as to determine their physical origin more exactly.

An issue which has not been addressed in this thesis was the optimization of the vertical device layer structure with respect to noise in order to find the optimal tradeoff between low base resistance and high current gain. However, we found that the base current noise is dominant at current levels where the device shows good RF performance. This indicates, that the devices can be designed with a larger current gain at a cost of an increased base resistance. Further investigations have to show how this can be realized without degrading other device performances.

In the field of circuit design, we obtained good performances with our amplifiers and oscillators. However, all the results were obtained from on-wafer measurements. For most practical applications, packaged modules are necessary. Therefore, investigations of high-frequency packaging technologies are required.

The demand for higher data rates, e.g. 80 Gb/s can only be satisfied if the bandwidths of the amplifiers are extended to 60 GHz and higher. Other applications, such as automotive radar, require oscillators in the W-band (94 GHz). To reach these higher frequencies, models of the layout elements are needed in order to be able to optimize and reduce the parasitics of the layout.

Appendix A

Noise Theory

A.1 Thermal Noise

A.1.1 Time distribution between two collisions

Assumptions:

- number of charge carriers which suffer impacts at $t = 0$ is C
- impacts are independent of each other

$\implies$ change in the number of charge carriers which have not suffered impacts between t and $t + dt$ is

$$dC(t) = \frac{C(t)dt}{\theta} \tag{A.1}$$

where θ is the average time between impacts. Solving this differential equation, the density function of the time distribution between two impacts may be determined:

$$f(t) = \frac{1}{\theta} e^{-t/\theta} \tag{A.2}$$

The first and second moments of this distribution are $M(t) = \theta$, $M(t^2) = 2\theta^2$, respectively.

A.1.2   Conductivity

The conductivity σ can be defined using the following equation:

$$J_x = \sigma \mathcal{E}_x = -qn\overline{v_d} \tag{A.3}$$

where n denotes the carrier density, $\overline{v_d}$ the average drift velocity, and $\mathcal{E}_x$ the electric field in x-direction. In order to calculate the conductivity σ, we have to be able to express the average drift velocity $\overline{v_d}$ by the electric field in x-direction $\mathcal{E}_x$. Therefore, the following calculation steps are necessary.

Acceleration of the electrons:

$$a_x = -\frac{q}{m^*}\mathcal{E}_x \tag{A.4}$$

where m^* is the effective mass of the electron in the crystal.

Total distance x_K covered during a large number of impacts K

$$x_K = \frac{a}{2}\sum_{i=1}^{K} t_i^2 = \frac{a}{2}KM(t^2) = aK\theta^2 \tag{A.5}$$

Total time t_k needed to cover this distance

$$t_k = \sum_{i=1}^{K} t_i = KM(t) = K\theta \tag{A.6}$$

Average drift velocity:

$$\overline{v_d} = \frac{x_K}{t_K} = a\theta = -\frac{q}{m^*}\mathcal{E}_x\theta \tag{A.7}$$

The current density can now be calculated:

$$J_x = -qn\overline{v_d} = \frac{q^2}{m^*}n\theta\mathcal{E}_x \tag{A.8}$$

We then have for the conductivity

$$\sigma = \frac{J_x}{\mathcal{E}_x} = \frac{q^2}{m^*}n\theta \tag{A.9}$$

A.2   G-R noise

A.2.1   Master Equation

The master equation is the differential equation for the probability $P(N)$ of finding N electrons in the conduction band. The equation is derived as follows: Let $g(N)dt$ be the probability that an electron is generated in the sample during the interval dt, and let $r(N)dt$ be the probability that an electron recombines during the interval dt. The master equation may then be written as

$$\frac{dP(N)}{dt} = r(N+1)P(N+1) + g(N-1)P(N-1)$$
$$- P(N)g(N) - P(N)r(N) \tag{A.10}$$

from the known rates of the transitions $N+1 \rightleftharpoons N$ and $N-1 \rightleftharpoons N$. Since $dP(N)/dt = 0$ for equilibrium, one finds by substitution that the equilibrium distribution may be written

$$P(N) \prod_{v=1}^{N} r(v) = P(0) \prod_{v=0}^{N-1} g(v) \tag{A.11}$$

According to Eq. (A.11) and with $\ln(P(N+1)r(N+1)) = \ln(P(N)g(N))$

$$\frac{d\ln P(N)}{dN} = \frac{\ln P(N+1) - \ln P(N)}{1} = \ln g(N) - \ln r(N+1) \tag{A.12}$$

The most probable value N_0 of N is found be setting Eq. (A.12) equal to zero. Hence $\ln g(N_0) = \ln r(N_0 + 1)$ or, if N_0 is large,

$$g(N_0) = r(N_0) \tag{A.13}$$

so that generation and recombination balance. Moreover,

$$\frac{d^2 \ln P(N)}{dN^2}\bigg|_{N_0} = \frac{g'(N_0)}{g(N_0)} - \frac{r'(N_0+1)}{r(N_0+1)} = \frac{g'(N_0) - r'(N_0)}{g(N_0)} \tag{A.14}$$

where g' and r' denote the derivates with respect to N.

We now find $\overline{(N-N_0)^2}$ by observing that $P(N)$ can be approximated by a normal law for N close to N_0:

$$P(N) = P(N_0) \exp\left[-\frac{(N-N_0)^2}{2\overline{(N-N_0)^2}}\right] \tag{A.15}$$

By combining Eqs. (A.14) and (A.15), we obtain

$$\frac{d^2}{dN^2}[\ln P(N)]_{N=N_0} = \frac{g'(N_0) - r'(N_0)}{g(N_0)} = \frac{1}{(N - N_0)^2} \qquad (A.16)$$

Hence

$$\overline{\Delta N^2} = \overline{(N - N_0)^2} = \frac{g(N_0)}{r'(N_0) - g'(N_0)} \qquad (A.17)$$

The differential equation for the decay of the excess concentration $\Delta N = N - N_0$ is

$$\frac{d}{dt}(\Delta N) = g(N) - r(N) = -[r'(N_0) - g'(N_0)]\Delta N \qquad (A.18)$$

From Eq. (A.18), we obtain for the time constant τ of the added carriers

$$\tau = \frac{1}{r'(N_0) - g'(N_0)} \qquad (A.19)$$

so that

$$\overline{\Delta N^2} = g_0 \tau \qquad (A.20)$$

Eq. (A.20) can be used to evaluate the spectrum of the g-r noise when we set the time constant τ equal to the carrier lifetime τ_{gr}

$$S_{NN} = 4\overline{\Delta N^2}\frac{1}{1 + \omega^2 \tau_{gr}^2} = 4g_0 \frac{\tau_{gr}^2}{1 + \omega^2 \tau_{gr}^2} \qquad (A.21)$$

A.2.2 Trap Distribution

Here, we calculate the distribution of the time constants for the recombination of charge carriers with traps located e.g. in a oxide at a distance between 0 and y_1 from the semiconductor surface.
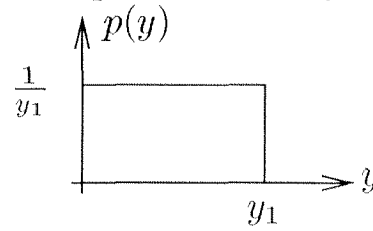
Assumptions:

- the carriers reach the trap by tunneling

$$\tau = \tau_0 \exp(\gamma y) \qquad \tau_1 = \tau_0 \exp(\gamma y_1) \qquad (A.22)$$

where τ and γ are the tunneling time and constant, respectively.

- the traps are uniformly distributed

$$f(y) = \begin{cases} \dfrac{1}{y_1} & \text{for } 0 < y < y_1 \\ 0 & \text{elsewhere} \end{cases} \quad \text{(A.23)}$$

The distribution of the locations of the traps y can be transformed into the distribution of their time constants

$$p(\tau)d\tau = p(y)dy \qquad \Rightarrow p(\tau) = p(y)\frac{dy}{d\tau} \qquad \text{(A.24)}$$

$$y = \frac{1}{\gamma}\ln \tau/\tau_0 \qquad \text{(A.25)}$$

We now can calculate the distribution of the time constants $p(\tau)$

$$p(\tau) = \begin{cases} \dfrac{1}{\gamma \tau_0}\dfrac{1}{\tau/\tau_0}\dfrac{1}{y_1} = \dfrac{1}{\ln \tau_1/\tau_0}\dfrac{1}{\tau} & \text{for } \tau_0 < \tau < \tau_1 \\ 0 & \text{elsewhere} \end{cases} \quad \text{(A.26)}$$

which is a continuous distribution of the time constants τ with the statistical weights proportional to τ^{-1}

Seite Leer /
Blank leaf

Appendix B

Measurements

B.1 De-Embedding

In order to determine the S-parameters of the transistor, the influence of the pads have to be eliminated in the measured noise and S-parameter. This so-called de-embedding is explained here for the S-parameters. For the noise parameters, the reader is referred to the literature [59, 91].

The calculations are based on the model of the pads connected to the transistor, shown in Figure B.1. The S-parameters S_m are measured at the
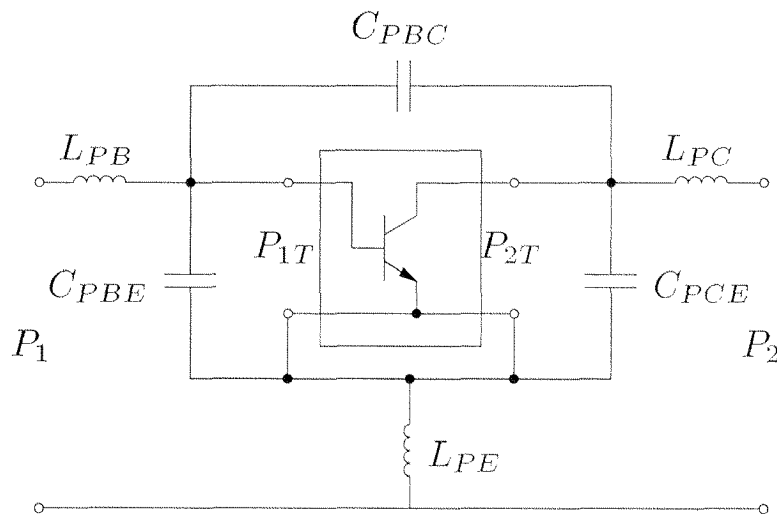
Figure B.1: *Equivalent model of the measurement pads connected to the transistor*

ports P_1 and P_2 but we intend to obtain the S-Parameters S_T at the ports P_{1T} and P_{2T}. If all pad inductances (L_{PB}, L_{PC}, L_{PE}) and capacitances (C_{PBE}, C_{PCE}, C_{PBC}) are known S_T can be calculated. The pad inductances are obtained from measured S-parameters of a shorted pad structure, which are transformed into the Z-parameters $\Rightarrow YZ_{Lp}$. In order to determine the pad capacitances, we have to transform the measured S-parameters of an open pad structure into the Y-parameters $\Rightarrow Y_{Cp}$. The de-embedding procedure is as follows:

1. Transformation of the measured S-parameters S_m into Z-parameters: $S_m \to Z_m$

2. Subtraction of the influence of the pad inductances: $Z_1 = Z_m - Z_{Lp}$

3. Matrix transformation: $Z_1 \to Y_1$

4. Elimination the influence of the pad capacitance: $Y_T = Y_1 - Y_{Cp}$

5. Final transformation: $Y_T \to S_T$

B.2 Low-Frequency Noise

For the calculation of the noise current i_{nlf} at the base from the measured noise voltage u_{nc} at the collector, u_{nc} has to be transformed to the base. We use the simplified model depicted in Figure B.2.
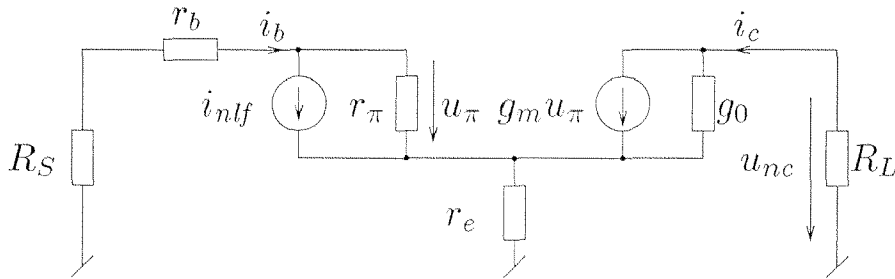
Figure B.2: *Simplified low-frequency noise model*

$$0 = (r_b + R_S)i_b + u_\pi + (i_b + i_c)r_e \tag{B.1}$$

$$u_\pi = (i_b - i_{nlf})r_\pi \tag{B.2}$$

$$i_c = g_m u_\pi + g_o(u_{nc} - (i_b + i_c)r_e)) \tag{B.3}$$

$$i_c = -u_{nc}/R_L \tag{B.4}$$

Combining Eqs. (B.1), (B.2), and (B.4), we obtain

$$0 = i_b(r_b + R_S + r_\pi + r_e) - r_\pi i_{nlf} - u_{nc} r_e / R_L \qquad (\text{B.5})$$

From Eqs. (B.2), (B.3), and (B.4) result

$$\frac{-u_{nc}}{R_L} = u_{nc} g_o - i_b r_e g_o + \frac{r_e g_o u_{nc}}{R_L} + g_m r_\pi i_b - g_m r_\pi i_{nlf} \qquad (\text{B.6})$$

$$i_b = \frac{1 + g_o r_e + g_o R_L}{R_L(r_e g_o - g_m r_\pi)} u_{nc} - \frac{g_m r_\pi R_L}{R_L(r_e g_o - g_m r_\pi)} i_{nlf} \qquad (\text{B.7})$$

Eqs. (B.5) and (B.7) lead to the following expressions

$$\frac{(1 + g_o r_e + g_o R_L)(r_b + R_S + r_\pi + r_e)}{R_L(r_e g_o - g_m r_\pi)} u_{nc} - \frac{r_e}{R_L} u_{nc}$$
$$= r_\pi i_{nlf} + \frac{g_m r_\pi R_L(r_b + R_S + r_\pi + r_e)}{R_L(r_e g_o - g_m r_\pi)} \qquad (\text{B.8})$$

$$((1 + g_o r_e + g_o R_L)(r_b + R_S + r_\pi + r_e) - r_e(r_e g_o - g_m r_\pi)) u_{nc}$$
$$= (g_m r_\pi R_L(r_b + R_S + r_e) + R_L r_\pi r_e g_o) \qquad (\text{B.9})$$

Assuming that $\beta = r_\pi g_m$, $R_S \gg r_b$, $R_S \gg \beta r_e$, and $g_m \gg g_o$, $R_L \gg r_e$ we obtain

$$u_{nc}((1 + g_o R_L)R_S + \beta r_e) = i_{nlf}(\beta R_L R_S) \qquad (\text{B.10})$$

$$u_{nc} = \frac{\beta R_L R_S}{(1 + g_o R_L)R_S + \beta r_e} i_{nlf} \simeq \beta R_L i_{nlf} \qquad (\text{B.11})$$

Appendix C

Model Equations

C.1 Emitter Noise Current

From the analogy between the carrier transport in the emitter and the wave propagation on a lossy transmission line, we obtain for the hole injection from the base into the emitter

$$
\begin{aligned}
\overline{i_p^2} = \overline{i_{Bp}^2} = \overline{i_{Ep}^2} = \sum \overline{\Delta i_p^2} \\
= \frac{4q^2 A}{\tau_p} \left| \frac{\gamma_E}{\gamma_{0,E}} \right|^2 \int_0^\infty (p'(x) + p_{n,E}) e^{-2a_E x} \, dx \\
+ \frac{2q^2 A}{\tau_p} \int_0^\infty (p'(x) + 2p_{n,E}) e^{-2a_E x} \, dx
\end{aligned}
\tag{C.1}
$$

where $a_E = \Re\{\gamma_E\} = \gamma_{0,E} \sqrt{\left(1 + \sqrt{1 + \omega^2 \tau_p^2}\right)/2}$

Since $p'(x) = p'_{0,B} e^{-\gamma_{0,E} x}$ we can write

$$
\begin{aligned}
\overline{i_p^2} = \frac{4q^2 A}{\tau_p} \left| \frac{\gamma_E}{\gamma_{0,E}} \right|^2 \int_0^\infty (p'_{0,B} e^{-\gamma_{0,E} x} + p_{n,E}) e^{-2a_E x} \, dx \\
+ \frac{2q^2 A}{\tau_p} \int_0^\infty (p'_{0,B} e^{-\gamma_{0,E} x} + 2p_{n,E}) e^{-2a_E x} \, dx
\end{aligned}
\tag{C.2}
$$

Solving the integrals leads to

$$
\overline{i_p^2} = \frac{4q^2 A}{\tau_p} \sqrt{1 + \omega^2 \tau_p^2}
$$

$$
\cdot \left(\frac{p'_{0,B}}{-(\gamma_{0,E} + 2a_E)} e^{-(\gamma_{0,E}+2a_E)x} \Big|_0^\infty + \frac{p_{n,E}}{-2a_E} e^{-2a_E x} \Big|_0^\infty \right)
$$

$$
+ \frac{2q^2 A}{\tau_p} \left(\frac{p'_{0,B}}{-(\gamma_{0,E} + 2a_E)} e^{-(\gamma_{0,E}+2a_E)x} \Big|_0^\infty \frac{2p_{n,E}}{-2a_E} e^{-2a_E x} \Big|_0^\infty \right)
$$

$$\tag{C.3}$$

For the integration between 0 and ∞ results

$$
\overline{i_p^2} = \frac{4q^2 A}{\tau_p} \sqrt{1 + \omega^2 \tau_p^2} \left(\frac{p'_{0,B}}{\gamma_{0,E} + 2a_E} + \frac{p_{n,E}}{2a_E} \right)
$$

$$
+ \frac{2q^2 A}{\tau_p} \left(\frac{p'_{0,B}}{\gamma_{0,E} + 2a_E} + \frac{2p_{n,E}}{2a_E} \right)
$$

$$\tag{C.4}$$

Rearranging the equations leads to

$$
\overline{i_p^2} = \frac{2q^2 A p'_{0,B}}{\tau_p \underbrace{(\gamma_{0,E} + 2a_E)}_{\gamma_{0,E}\left(\frac{2a_E}{\gamma_{0,E}}+1\right)}} \underbrace{\left(1 + 2\sqrt{1 + \omega^2 \tau_p^2}\right)}_{\left(\frac{2a_E}{\gamma_{0,E}}\right)^2 - 1}
$$

$$
+ \frac{4q^2 A p_{n,E}}{\tau_p 2a_E} \underbrace{\left(1 + \sqrt{1 + \omega^2 \tau_p^2}\right)}_{\frac{2a_E^2}{\gamma_{0,E}^2}}
$$

$$\tag{C.5}$$

We finally obtain

$$
\overline{i_p^2} = \frac{2q^2 A p'_{0,B}}{\tau_p \gamma_{0,E}} \left(\frac{2a_E}{\gamma_{0,E}} - 1 \right) + \frac{2q^2 A p_{n,E}}{\tau_p \gamma_{0,E}} \frac{2a_E}{\gamma_{0,E}}
$$

$$\tag{C.6}$$

With $1/(\tau_p \gamma_{0,E}) = D_p \gamma_{0,E}$, this result can be written as

$$
\overline{i_p^2} = 2q \left[\underbrace{q A p'_{0,B} D_p \gamma_{0,E}}_{I_p} \left(\frac{2a_E}{\gamma_{0,E}} - 1 \right) + \underbrace{q A p_{n,E} D_p \gamma_{0,E}}_{I_{p,0}} \frac{2a_E}{\gamma_{0,E}} \right] \tag{C.7}
$$

$$
= 2q \left[I_p \left(\frac{2a_E}{\gamma_{0,E}} - 1 \right) + I_{p,0} \frac{2a_E}{\gamma_{0,E}} \right] \tag{C.8}
$$

where $\frac{2a_E}{\gamma_{0,E}} = \sqrt{2\left(1 + \sqrt{1 + \omega^2\tau_p^2}\right)}$ describes the frequency dependence of the power spectral density of the noise. I_p and I_{p0} can be interpreted as a current through a junction and as the inverse current, respectively. For frequencies $f \ll (2\pi\tau_p)$, Eq. C.8 reduces to

$$\overline{i_p^2} = 2q(I_p + 2I_{p0}) \tag{C.9}$$

C.2 Noise Parameters

Alternative formulas to [7] for F_{min} and Z_{opt} are found in citechen89

$$F_{min} = a(r_b + r_e + R_{opt})g_m + \left(1 + \frac{f^2}{f_F^2}\right)\frac{\beta}{1 + \beta} \tag{C.10}$$

$$R_{opt} = \sqrt{(r_b + r_e)^2 - X_{opt}^2 + \left(1 + \frac{f^2}{f_F^2}\right)\frac{2r_b + 1/g_m}{ag_m}\frac{\beta}{1 + \beta}} \tag{C.11}$$

$$X_{opt} = \left(1 + \frac{f^2}{f_F^2}\right)\frac{2\pi f C_{je}}{ag_m^2}\frac{beta}{1 + \beta} \tag{C.12}$$

$$Z_{opt} = R_{opt} + jX_{opt} \tag{C.13}$$

$$a = \frac{\beta}{1 + \beta}\left(1 + \frac{f^2}{f_F^2}\right)\left(1 + \frac{f^2}{f_e^2}\right) - 1 \tag{C.14}$$

C.3 Device Physics

Calculation of the depletion width X_{depl} and depletion capacitance C_{depl} of a $p - n$ junction with two different materials having the dielectric constants ε_1 (n-material) and ε_2 (p-material):

$$X_{depl1} = \sqrt{\frac{2N_{A2}\varepsilon_1\varepsilon_2(V_{bi} - V)}{qN_{D1}(\varepsilon_1 N_{D1} + \varepsilon_2 N_{A2})}} \tag{C.15}$$

$$X_{depl2} = \sqrt{\frac{2N_{D1}\varepsilon_1\varepsilon_2(V_{bi} - V)}{qN_{A2}(\varepsilon_1 N_{D1} + \varepsilon_2 N_{A2})}} \tag{C.16}$$

$$X_{depl} = X_{depl1} + X_{depl2} \tag{C.17}$$

$$C_{depl} = \sqrt{\frac{qN_{D1}N_{A2}\varepsilon_1\varepsilon_2}{2(\varepsilon_1 N_{D1} + \varepsilon_2 N_{A2})(V_{bi} - V)}} \tag{C.18}$$

where N_{A1} and N_{D2} are the acceptor concentration in the p-material and the donor concentration in the n-material. V_{bi} is the total built-in voltage which is related to the partial built-in voltages V_{b1} and V_{b2} as follows:

$$\frac{V_{b1} - V_1}{V_{b2} - V2} = \frac{N_{A2}\varepsilon_2}{N_{D1}\varepsilon_1} \tag{C.19}$$

where $V = V_1 + V_2$ denotes the applied total voltage.

Appendix D

Circuit Design

D.1 Oscillator

Calculation of the input impedance Z_{in} of an HBT connected via a capacitance C_E to ground

$$Z_{in} = r_b - r_\pi \frac{1 + r_\pi g_m \frac{c_\pi}{C_E}}{1 + (\omega r_\pi c_\pi)^2}$$

$$+ \frac{1}{j\omega C_E} \cdot \frac{1 + r_\pi g_m + (\omega r_\pi c_\pi)^2 \left(1 + \frac{C_E}{c_\pi}\right)}{1 + (\omega r_\pi c_\pi)^2} \qquad (D.1)$$

we can write: $\beta = g_m r_\pi$, $\omega_\beta = (r_\pi c_\pi)^{-1}$
further assumption: $\beta \gg 1$, $\beta c_\pi / C_E \gg 1$

$$Z_{in} \simeq r_b - \frac{\frac{\beta \omega_\beta}{C_E}}{1 + \left(\frac{\omega}{\omega_\beta}\right)^2} + \frac{1}{j\omega C_E} \frac{1 + \left(\frac{\omega}{\omega_\beta}\right)^2 \frac{1}{\beta}\left(1 + \frac{C_E}{c_\pi}\right)}{1 + \left(\frac{\omega}{\omega_\beta}\right)^2} \qquad (D.2)$$

List of Symbols

A	area
A_E	emitter area
Al	aluminum
As	arsenic
Au	gold
B	large-signal current gain
BER	bit error rate
B_{opt}	susceptance
BV_{CE0}	collector-emitter breakdown voltage
C	capacitance
C_d	diffusion capacitance
Cr	chromium
c	correlation coefficient
c_{ibic}	base to collector noise currents correlation coefficient
c_j	junction capacitance
c_x	extrinsic base-collector small-signal capacitance
c_μ	intrinsic base-collector small-signal capacitance
c_π	base-emitter small-signal capacitance
D_n, D_p	electron, hole diffusion constant
DUT	device under test
E	energy
E_g	bandgap energy
Er	erbium
$\mathcal{E}$	electric field
e_n	voltage noise source
F	noise figure
F_{min}	minimum noise figure
Fe	iron

$\mathcal{F}$	Fourier transform
f_{max}	maximum oscillation frequency
f_T	transit frequency
f_β	3 dB frequency of β
Ga	gallium
GBW	gain-bandwidth product
G_{opt}	optimum source conductance
G_P	power gain
G_S	source conductance
G_U	Mason's unilateral gain
g_m	transconductance
g_o	output conductance
(S)HBT	(single) heterojunction bipolar transistor
HEMT	high electron mobility transistor
h	Planck constant
I_B, I_E, I_C	base, emitter, collector DC-current
IM_3	third-order intermodulation product
In	indium
I_n, I_p	electron, hole DC-current
IP_3	third-order intercept point
I_S	saturation current
I_{SCR}	space charge recombination current
i_{bp}, i_{ep}	base, emitter hole small-signal current
$i_{br},$	base, recombination small-signal current
i_{cn}, i_{en}	collector, emitter electron small-signal current
i_{dx}	diffusion current at location x
i_g, i_r	generation, recombination current
i_n	current noise
$i_{n,p}$	electron, hole small-signal current
i_{nlf}	low-frequency noise source
$\Im$	imaginary part
J_{CK}	critical collector current density
j	current density
k	Boltzmann constant
L_E	emitter length
L_i	Lorentz spectrum
L_n, L_p	electron, hole diffusion length
LNA	low-noise amplifier
l	length
M	noise measure, statistical moment

MAG	maximum available gain
MIM	metal-insulator-metal
MMIC	monolithic microwave integrated circuit
MOVPE	metal-organic vapor-phase epitaxy
MSG	maximum stable gain
m^*	effective mass
N	noise power, number of electrons
N_C	collector doping concentration
NRZ	non-return to zero
n	electron concentration
n_B, n_F	ideality factors of the base, collector current
O	oxygen
OEIC	optical/electrical integrated circuit
P	phosphorus
P	power, probability, number of holes
P_E	emitter perimeter
PRBS	pseudo random bit sequence
Pt	platinum
p	hole concentration, probability density function
q	electron charge
R	resistance
R_B, R_E, R_C	base, emitter, collector DC-resistance
$R_c\ R_g, R_i$	contact, gap, intrinsic DC-resistance
R_n	noise resistance
R_{opt}	optimum source resistance
$\Re$	real part
$r_{bb'}, r_{bc}$	base, base contact small-signal resistance
r_e, r_c	emitter, collector small-signal resistance
r_o	output resistance
r_μ	base-collector leakage small-signal resistance
r_π	base-emitter small-signal resistance
S	power spectral density, signal power
SEM	scanning electron microscopy
Sn	tin
Si	silicon
T	temperature
Ta	tantalum
Ti	titanium
T_J	junction temperature
TWA	traveling wave amplifier

u_n	voltage noise
V	voltage
V_A	Early voltage
V_B, V_E, V_C	base, emitter, collector DC-voltage
V_{sat}	saturation or knee voltage
V_S	source voltage
V_T	thermal voltage
V_{bi}	built-in potential
v_B, v_E, v_C	base, emitter, collector small-signal voltage
v_{eff}	effective velocity
v_{sat}	saturation velocity
v_x	velocity in x-direction
W_E	emitter width
w	particle current
X_B, X_E, X_C	base, emitter, collector thickness
X_{cap}	thickness of the cap layer
X_{depl}	depletion width
X_{opt}	reactance
X_{subC}	subcollector thickness
Y_{in}	input admittance
Y_{opt}	optimum source admittance
Y	admittance
Y_S	source admittance
Z	impedance
Z_0	characteristic line impedance
Z_{in}	input impedance
Zn	zinc
Z_{opt}	optimum source impedance
Z_S	source impedance
α_H	Hooge parameter
β	small-signal current gain
Γ	reflection factor
Γ_{opt}	optimum source reflection factor
Γ_S	source reflection factor
γ	propagation constant
ε_0	dielectric constant
ε_r	relative dielectric constant
θ	average time between impacts
μ	mobility
μ_n, μ_p	electron, hole mobility

ρ_b	resistivity of the bulk material
ρ_c	specific contact resistance
σ	conductivity
τ	time constant, decay time
τ_B, τ_C	base, collector delay
τ_{EC}	emitter-to-collector delay
τ_g	group delay
τ_{gr}	carrier lifetime
τ_n, τ_p	electron, hole minority lifetime
ϕ_{xx}, ϕ_{xy}	auto-, cross-correlation function
ω	angular frequency
ω_β	3 dB angular frequency of β

Physical Constants

Planck constant	h	$= 6.62617 \cdot 10^{-34}$ Js
Boltzmann constant	k	$= 1.38066 \cdot 10^{-23}$ J/K
electron charge	q	$= 1.60218 \cdot 10^{-19}$ As
dielectric constant	ε_0	$= 8.85418 \cdot 10^{-12}$ F/m

Material Properties

InGaAs

bandgap energy	E_g	$= 0.75$ eV
conduction band effective density of states	N_C	$= 2.1 \cdot 10^{17}$ cm^{-3}
valence band effective density of states	N_V	$= 9.2 \cdot 10^{18}$ cm^{-3}
dielectric constant	ε_r	$= 13.9$
intrinsic carrier density	n_i	$= 6.8 \cdot 10^{11}$ cm^{-3}

InP

bandgap energy	E_g	$= 1.34$ eV
conduction band effective density of states	N_C	$= 5.4 \cdot 10^{17}$ cm^{-3}
valence band effective density of states	N_V	$= 1.2 \cdot 10^{19}$ cm^{-3}
dielectric constant	ε_r	$= 12.4$
intrinsic carrier density	n_i	$= 1.3 \cdot 10^{7}$ cm^{-3}

InP/InGaAs heterojunction

conduction band discontinuity	ΔE_C	$= 0.22$ eV
valence band discontinuity	ΔE_V	$= 0.37$ eV
base-emitter built-in potential [6]	V_{bi}	$= 1.00$ V
base-collector built-in potential [6]	V_{bi}	$= 0.93$ V

List of Figures

List of Tables

Seite Leer /
Blank leaf

References

[1] K. Runge, P. J. Zampardi, R. L. Pierson, P. B. Thomas, S. M. Beccue, R. Yu, and K. C. Wang, "High Speed AlGaAs/GaAs HBT Circuits For Up To 40 Gb/s Optical Communication," in *IEEE GaAs IC Symposium*, pp. 211–214, 1997.

[2] M. Rodwell, J. F. Jensen, W. E. Stanchina, R. A. Metzger, D. B. Rensch, M. W. Pierce, T. V. Kargodorian, and Y. K. Allen, "33-GHz Monolithic Cascode AlInAs/GaInAs Heterojunction Bipolar Transistor Feedback Amplifier," in *IEEE 1990 Bipolar Circuits and Technology Meeting*, pp. 252–255.

[3] J. Müllrich, T. F. Meister, M. Rest, W. Bogner, A. Schöpflin, and H.-M. Rein, "40 Gbit/s Transimpedance Amplifier in SiGe Bipolar Technology for the Receiver in Optical-Fibre TDM Links," *IEE Electronics Letters*, vol. 34, pp. 452–453, Mar. 1998.

[4] Q. Lee, S. C. Martin, D. Mensa, R. P. Smith, J. Guthrie, and M. J. W. Rodwell, "Submicron Transferred-Substrate Heterojunction Bipolar Transistor," *IEEE Electron Device Letters*, vol. 20, pp. 396–398, Aug. 1999.

[5] P. M. Smith, "Status of InP HEMT Technology for Microwave Receiver Applications," in *IEEE 1996 Microwave and Millimeter-Wave Monolithic Circuits Symposium*, pp. 129–132.

[6] R. Bauknecht, *InP Double Heterojunction Bipolar Transistors for Driver Circuits in Fibre Optical Communication Systems*. PhD thesis No. 12455, ETH Zürich, 1998.

[7] L. Escotte, J. P. Roux, R. Plana, J. Graffeuil, and A. Gruhl, "Noise Modeling of Microwave Heterojunction Bipolar Transistor," *IEEE Transactions on Electron Devices*, vol. 42, pp. 883–889, May 1995.

[8] J.-P. Roux, L. Escotte, R. Plana, J. Graffeuil, S. L. Delage, and H. Blanck, "Small-Signal and Noise Model Extraction Technique for Heterojunction Bipolar Transistor at Microwave Frequencies," *IEEE Transactions on Microwave Theory and Techniques*, vol. 43, pp. 293–297, Feb. 1995.

[9] R. A. Pucel, T. Daniel, A. Kain, and R. Tayrani, "A Bias and Temperature Dependent Noise Model of Heterojunction Bipolar Transistors," in *IEEE MTT-S Intl. Microwave Symposium Digest*, pp. 141–144, 1998.

[10] H. Dodo, Y. Amamiya, T. Niwa, M. Mamada, S. Tanaka, and H. Shimawaki, "Microwave Low-Noise GaAs HBTs," in *IEEE MTT-S International Microwave Symposium*, pp. 1–4, 1998.

[11] T. Daniel, "Bias and Temperature Dependent Noise Modeling of HBTs," in *IEEE MTT-S Intl. Microwave Symposium Digest*, pp. 1469–1472, 1997.

[12] J. J. Liou, T. J. Jenkins, L. L. Liou, R. Neidhard, D. W. Barlage, R. Fitch, J. P. Barrette, M. Mack, C. A. Bozada, R. H. Y. Lee, R.-W. Dettmer, and J. S. Sewell, "Bias, Frequency, and Area Dependencies of High Frequency Noise in AlGaAs/GaAs HBTs," *IEEE Transactions on Electron Devices*, vol. 43, pp. 116–122, Jan. 1996.

[13] Y. Takanashi and H. Fukano, "Low-Frequency Noise of InP/InGaAs Heterojunction Bipolar Transistors," *IEEE Transactions on Electron Devices*, vol. 45, pp. 2400–2406, Dec. 1998.

[14] B. Bayraktaroglu, G. Dix, and D. Pavlidis, "AlGaAs/GaAs HBT Reliability: Dependence on Material and Correlation to Baseband Noise," in *Technical Digest, 19th GaAs IC Symposium*, pp. 157–160, 1997.

[15] A. K. Kirtania, M. B. Das, S. Chandrasekhar, L. M. Lunardi, G. J. Qua, R. A. Hamm, and L. W. Yang, "Measurement and Comparison of $1/f$ Noise and g-r Noise in Silicon Homojunction and III-V Heterojunction Bipolar Transistors," *IEEE Transactions on Electron Devices*, vol. 43, pp. 784–792, May 1996.

[16] H. T. Friis, "Noise Figure of Radio Receiver," *Proceedings of the IRE*, vol. 32, pp. 419–422, July 1944.

[17] A. van der Ziel, *Noise in Solid State Devices and Circuits*. John Wiley & Sons Inc., 1986.

[18] A. Ambrózy, *Electronic Noise*. McGraw-Hill, 1982.

[19] R. E. Burgess, "The Statistics of Charge Carrier Fluctuations in Semiconductors," *Proc. of the Physical Society of London*, vol. 69B, pp. 1020–1027, 1956.

[20] W. J. Moore, "Statistical Studies of $1/f$ noise from carbon resistors," *Journal of Applied Physics*, vol. 45, pp. 1896–1901, Apr. 1974.

[21] S. T. Hsu, "Surface State Related $1/f$ Noise in $p - n$ Junctions," *Solid-State Electronics*, vol. 13, pp. 843–855, June 1970.

[22] F. N. Hooge, T. G. M. Kleinpenning, and L. K. J. Vandamme, "Experimental Studies on $1/f$ noise," *Report on Progress in Physics*, vol. 44, pp. 479–532, 1981.

[23] M. A. Calozannides, "Microcycle Spectral Estimates of $1/f$ Noise in Semiconductors," *Journal of Applied Physics*, vol. 45, pp. 307–316, Jan. 1974.

[24] A. L. McWhorter, *Semiconductor Surface Physics*, ch. $1/f$ Noise in Germanium Surface Properties, pp. 207–228. University of Pennsylvania Press, Philadelphia, 1957.

[25] F. N. Hooge, "Discussion of Recent Experiments on $1/f$ Noise," *Physica*, vol. 60, pp. 130–144, 1972.

[26] F. N. Hooge, "$1/f$ Noise is no Surface Effect," *Physics Letters*, vol. 29A, pp. 139–140, Apr. 1969.

[27] S. Martin, P. R. Smith, M. Haner, R. K. Montgomery, R. A. Hamm, A. Feygenson, and R. D. Yadvish, "Low Frequency Noise and Microwave Properties of InP/InGaAs Heterojunction Bipolar Transistors," in *Proceedings of the 6th Intl. Conf. on Indium Phosphide and Related Material*, pp. 531–534, 1994.

[28] A. Ouacha, M. Willander, R. Plana, J. Graffeuil, L. Escotte, and B. Willen, "Low Frequency Noise Characterization of Self-Aligned InP/InGaAs Heterojunction Bipolar Transistor," *Journal of Applied Physics*, vol. 78, pp. 2565–2567, Aug. 1995.

[29] M. N. Tutt, D. Pavlidis, and B. Bayraktaroglu, "An Assessment of Noise Sources and Characteristics of AlGaAs/GaAs Heterojunction Bipolar Transistors," in *International Symposium on GaAs and Related Compounds*, pp. 701–706, 1989.

[30] A. van der Ziel, "Proposed Discrimination Between $1/f$ Noise Source in Transistors," *Solid-State Electronics*, vol. 25, pp. 141–143, Feb. 1982.

[31] S. Chandrasekhar, "The Progress and Performance of Long Wavelength OEIC Photoreceivers Incorporating Heterojunction Bipolar Transistors," *International Journal of High Speed Electronics and Systems*, vol. 5, pp. 45–65, Mar. 1994.

[32] H. Krömer, "Heterostructure Bipolar Transistors and Integrated Circuits," *Proceedings of the IEEE*, vol. 70, pp. 227–239, Jan. 1982.

[33] B. Jalali, Y.-K. Chen, R. N. Nottenburg, D. Sivco, D. A. Humpherey, and A. Y. Cho, "Influence of Base Thickness on Collector Breakdown in Abrupt AlInAs/InGaAs Heterojunction Bipolar Transistors," *IEEE Electron Device Letters*, vol. 11, pp. 400–402, Sept. 1990.

[34] J. A. Baquedano, A. F. J. Levi, and B. Jalali, "Comparison of Graded and Abrupt Junctions $In_{0.53}Ga_{0.47}As$ Heterojunction Bipolar Transistors," *Applied Physics Letters*, pp. 67–69, Jan. 1994.

[35] A. Feygenson, O. A. Mezrin, P. R. Smith, R. A. Hamm, R. K. Montgomery, R. D. Yadvish, D. Ritter, and M. Haner, "Ballistic Transport Effects in InP/InGaAs Heterostructure Bipolar Transistors," in *1993 IEEE International Electron Device Meeting*, pp. 799–802.

[36] B. Jalali, *InP HBTs: Growth, Processing, and Applications*. Artech House, 1995.

[37] D. Ritter, R. A. Hamm, A. Feygenson, M. B. Panish, and S. Chandrasekhar, "Diffusive Base Transport in Narrow Base InP/$Ga_{0.47}In_{0.53}As$ Heterojunction Bipolar Transistors," *Applied Physics Letters*, vol. 59, pp. 3431–3433, Dec. 1991.

[38] S. M. Sze, *Physics of Semiconductor Devices*. John Wiley & Sons, Inc., 2nd ed., 1981.

[39] D. L. Bowler and F. A. Lindholm, "High Current Regimes in Transistor Collector Regions," *IEEE Transactions on Electron Devices*, vol. 20, pp. 257–263, Mar. 1973.

[40] G. P. Agrawal, *Fiber-Optic Communication Systems*. John Wiley & Sons, Inc., 1997.

[41] R. Bauknecht, H. P. Schneibel, J. Schmid, and H. Melchior, "12 Gbit/s Laser Diode and Optical Modulator Drivers with InP/InGaAs Double HBTs," *Electronics Letters*, vol. 32, pp. 2156–2157, Nov. 1996.

[42] D. Huber, M. Bitter, S. Romier, I. Schnyder, R. Bauknecht, T. Morf, C. Bergamaschi, and H. Jäckel, "23 GHz Monolithically Integrated InP/InGaAs PIN/HBT-Receiver with 12 THzΩ Gain-Bandwidth Product," in *Proc. of the 10th Intl. Conference on Indium Phosphide and Related Materials*, pp. 447–450, 1998.

[43] D. Costa and J. S. Harris, Jr., "Low-Frequency Noise Properties of $N-p-n$ AlGaAs/GaAs Heterojunction Bipolar Transistors," *IEEE Transactions on Electron Devices*, vol. 39, pp. 2383–2394, Oct. 1992.

[44] S. Tanaka, K. Kasahara, H. Shimawaki, and K. Honjo, "Stress Current Behavior of InAlAs/InGaAs and AlGaAs/GaAs HBTs with Polyimide Passivation," *IEEE Electron Device Letters*, vol. 13, pp. 560–562, Nov. 1992.

[45] H.-F. Chau and Y.-C. Kao, "High f_{max} InAlAs/InGaAs Heterojunction Bipolar Transistors," in *1993 IEEE International Electron Device Meeting*, pp. 783–786, Dec. 1993.

[46] M. F. Chang, ed., *Current Trends in Heterojunction Bipolar Transistors*, ch. InP-Based Heterojunction Bipolar Transistor, pp. 303–349. World Scientific, 1996.

[47] I. Getreu, *Modeling The Bipolar Transistor*. Tektronix, Inc., 1976.

[48] A. A. Grinberg and S. Luryi, "On the Thermionic-Diffusion Theory of Minority Transport in Heterostructures Bipolar Transistors," *IEEE Transactions on Electron Devices*, vol. 40, pp. 859–866, May 1993.

[49] S. J. Mason, "Power Gain in Feedback Amplifier," *Transactions of the I.R.E.*, vol. CT-1, pp. 20–25, June 1954.

[50] J. J. H. van den Biesen, "A simple regional analysis of transit times in bipolar transistors," *Solid-State Electronics*, vol. 29, no. 5, pp. 529–534, 1986.

[51] R. J. Whittier and D. A. Tremere, "Current Gain and Cutoff Frequency Falloff at High Currents," *IEEE Transactions on Electron Devices*, vol. 16, pp. 39–57, Jan. 1969.

[52] R. L. Pritchard, "High-Frequency Power Gain of Junction Transistors," *Proceedings of the IRE*, vol. 43, pp. 1075–1085, Sept. 1955.

[53] J. Lindmayer, "Power Gain of Transistors at High Frequencies," *Solid-State Electronics*, vol. 5, pp. 171–175, 1962.

[54] M. N. Tutt, D. Pavlidis, and H. F. Chau, "$1/f$ Noise Characteristics of InP/InGaAs Heterojunction Bipolar Transistors," in *Seventh International Conference on Indium Phosphide and Related Materials*, pp. 364–367, IEEE, 1992.

[55] A. K. Kirtania, M. B. Das, S. Chandrasekhar, L. M. Lunardi, R. A. Hamm, and L. W. Yang, "A Comparison of Low-Frequency Noise Characteristics of Silicon and III-V Heterojunction Bipolar Transistors," in *Proceedings of the 6th Intl. Conf. on Indium Phosphide and Related Material*, pp. 535–538, 1994.

[56] J.-H. Shin, Y. Chung, Y. Suh, and B. Kim, "Extraction of Low-Frequency Noise Model of Self-Aligned AlGaAs/GaAs Heterojunction Bipolar Transistor," in *1996 IEEE MTT-S International Microwave Symposium Digest*, pp. 1309–1312.

[57] G. Blasques and D. Sauvage, "Flicker Noise Due to Minority Carrier Trapping in the Bulk of Bipolar Transistors," in *Noise in Physical Systems and $1/f$ Noise*, pp. 405–407, 1985.

[58] X. Zhu and A. van der Ziel, "The Hooge Parameters of $n^+ - p - n$ and $p^+ - n - p$ Silicon Bipolar Transistors," *IEEE Transactions on Electron Devices*, vol. 32, pp. 658–661, Mar. 1985.

[59] R. A. Pucel, W. Struble, R. Hallgren, and U. L. Rohde, "A General Noise De-embedding Procedure for Packaged Two-Port Linear Active Devices," *IEEE Transactions on Microwave Theory and Techniques*, vol. 40, pp. 2013–2024, Nov. 1992.

[60] Hewlett Packard Company, *Application Note 57-1, Fundamentals of RF and Microwave Noise Measurements*.

[61] Hewlett Packard Company, *HP-ADS, Hewlett Packard Advanced Design System, Ver. 110.401*.

[62] P. Dodd and M. Lundstrom, "Minority Electron Transport in InP/InGaAs Heterojunction Bipolar Transistors," *Applied Physics Letters*, vol. 61, pp. 465–467, July 1992.

[63] D. Costa, W. U. Liu, and J. S. Harris, Jr., "Direct Extraction of the AlGaAs/GaAs Heterojunction Bipolar Transistor Small-Signal Equivalent Circuit," *IEEE Transactions on Electron Devices*, vol. 38, pp. 2018–2024, Sept. 1991.

[64] A. van der Ziel, "Theory of Shot Noise in Junction Diodes and Junction Transistors," *Proceedings of the IRE*, pp. 1639–1646, Nov. 1955.

[65] A. van der Ziel, "Noise in Solid-State Devices and Lasers," in *Proceedings of the IEEE*, vol. 58, pp. 1178–1206, Aug. 1970.

[66] *Properties of Indium Phosphide*. INSPEC, IEE, 1991.

[67] H. H. Berger, "Models for Contacts to Planar Devices," *Solid-State Electronics*, vol. 15, pp. 145–158, Feb. 1972.

[68] N. Chand, *Properties of Lattice-Matched and Strained Indium Gallium Arsenide*, ch. 4.4 Carrier Diffusion Length and Lifetimes in InGaAs, pp. 127–129. INSPEC, 1993.

[69] P. Ambrée, B. Gruska, and K. Wandel, "Dependence of the Electron Diffusion Length in p-InGaAs Layers on the Acceptor Diffusion Process," *Semiconductor Science and Technology*, vol. 7, pp. 858–860, June 1992.

[70] J. R. Hauser, "The Effects of Distributed Base Potential on Emitter-Current Injection Density and Effective Base Resistance for Stripe Transistor Geometries," *IEEE Transactions on Electron Devices*, vol. 11, pp. 238–242, May 1964.

[71] C. H. Henry, R. A. Logan, F. R. Merritt, and C. G. Bethea, "Radiative and Nonradiative Lifetimes in n-Type and p-Type 1.6 μm InGaAs," *Electronics Letters*, vol. 20, pp. 358–359, Apr. 1984.

[72] D. Caffin, A.-M. Duchenois, F. Héliot, C. Besombes, J.-L. Benchimol, and P. Launay, "Base-Collector Leakage Currents in InP/InGaAs Double Heterojunction Bipolar Transistors," *IEEE Transactions on Electron Devices*, vol. 44, pp. 930–936, June 1997.

[73] I. D. Robertson, ed., *MMIC Design*. The Institution of Electrical Engineers, 1995.

[74] B. Agarwa, A. E. Schmitz, J. J. Brown, M. Matloubian, M. G. Case, M. Le, M. Lui, and M. J. W. Rodwell, "112-GHz, 157-GHz, and

180-GHz InP HEMT Traveling-Wave Amplifiers," *IEEE Transactions on Microwave Theory and Techniques*, vol. 46, pp. 2553–2559, Dec. 1998.

[75] H. Suzuki, K. Watanabe, K. Ishikawa, H. Masuda, K. Ouchi, T. Tanoue, and R. Takeyari, "Very-High-Speed InP/InGaAs HBT ICs for Optical Transmission Systems," *IEEE Journal of Solid-State Circuits*, vol. 33, pp. 1313–1319, Sept. 1998.

[76] Y. Suzuki, H. Shimawaki, Y. Amamiya, N. Nagano, T. Niwa, H. Yano, and K. Honjo, "50–GHz-Bandwidth Baseband Amplifiers Using GaAs-Based HBTs," *IEEE Journal of Solid-State Circuits*, vol. 33, pp. 1336–1341, Sept. 1998.

[77] B. Agarwal, Q. Lee, D. Mensa, R. Pullela, J. Guthrie, and M. J. W. Rodwell, "Broadband Feedback Amplifier with AlInAs/GaInAs Transferred-Substrate HBT," *IEE Electronics Letters*, vol. 34, pp. 1357–1358, June 1998.

[78] I. Kipnis, J. F. Kukielka, J. Wholey, and C. P. Snapp, "Silicon Bipolar Fixed and variable Gain Amplifier MMICs for Microwave and Lightwave Applications up to 6 GHz," in *IEEE 1989 Microwave and Millimeter-Wave Monolithic Circuits Symposium Digest*, pp. 101–104.

[79] K. W. Kobayashi and A. K. Oki, "A DC-10 GHz High-Gain Low-Noise GaAs HBT Direct-Coupled Amplifier," *IEEE Microwave and Guided Wave Letters*, vol. 5, pp. 308–310, Sept. 1995.

[80] Sonnet Software, Inc., 1020 7th North Street, Suite 210, Liverpool, NY 13088 USA, *Sonnet User's Manual, Release 4.0*, 1996.

[81] Y. Suzuki, H. Shimawaki, Y. Amamiya, N. Nagano, T. Niwa, H. Yano, and K. Honjo, "50–GHz-Bandwidth Baseband Amplifiers Using GaAs-Based HBTs," in *1997 IEEE GaAs IC-Symposium Digest*, pp. 143–146.

[82] V. Hurm, W. Benz, W. Bronner, A. Hülsmann, T. Jakobus, K. Köhler, A. Leven, M. Ludwig, B. Raynor, J. Rosenzweig, M. Schlechtweg, and A. Thiede, "40 Gbit/s 1.55 μm PIN-HEMT photoreceiver monolithically integrated on a 3 in GaAs substrate," *IEE Electronics Letters*, vol. 34, pp. 2060–2061, Oct. 1998.

[83] E. Legros, S. Vuye, L. Giraudet, and C. Joly, "High-Sensitivity 40 Gbit/s Photoreceiver Using GaAs PHEMT Distributed Amplifiers," *IEE Electronics Letters*, vol. 34, pp. 1351–1352, June 1998.

[84] Z. Lao, V. Hurm, A. Thiede, M. Berroth, M. Ludwig, H. Lienhard, M. Schlechtweg, J. Hornung, W. Bronner, K. Köhler, A. Hülsmann, G. Kaufel, and T. Jakobus, "Modulator Driver and Photoreceiver for 20 Gb/s Optic-Fiber Links," *Journal of Lightwave Technology*, vol. 16, pp. 1491–1497, Aug. 1998.

[85] A. Huber, C. Bergamaschi, T. Morf, and H. Jäckel, "A DC–21 GHz High-Gain Noise-Matched InP/InGaAs HBT Differential Amplifier," in *Proc. of the 22nd Workshop on Compound Semiconductor Devices and Circuits*, pp. 78–79, May 1998.

[86] T. Vanisri and C. Toumazou, "Integrated High Frequency Low-Noise Current-Mode Optical Transimpedance Preamplifier: Theory and Practice," *IEEE Journal of Solid-State Circuits*, vol. 30, pp. 677–685, June 1995.

[87] D. Huber, M. Bitter, T. Morf, C. Bergamaschi, H. Melchior, and H. Jäckel, "46 GHz Bandwidth Monolithic InP/InGaAs PIN/SHBT Photoreceiver," *IEE Electronics Letters*, vol. 35, pp. 40–41, Jan. 1999.

[88] S. Chen, S. Tadayon, T. Ho, K. Pande, P. Rice, J. Adair, and M. Ghahremani, "U-Band MMIC HBT DRO," *IEEE Microwave and Guided Wave Letters*, vol. 4, pp. 50–52, Feb. 1994.

[89] H. Wang, K. W. Chang, L. T. Tran, J. C. Cowles, T. R. Block, E. W. Lin, G. S. Dow, A. K. Oki, D. C. Streit, and B. R. Allan, "Low Phase Noise Millimeter-Wave Frequency Source Using InP-Based HBT MMIC Technology," *IEEE Journal of Solid-State Circuits*, vol. 31, pp. 1419–1425, Oct. 1996.

[90] I. Aoki, K. Tezuka, H. Matsuura, S. Kobayashi, T. Fujita, T. Yakihara, S. Oka, and A. Miura, "64 GHz AlGaAs-HBT Oscillator," *Electronics Letters*, vol. 32, pp. 463–464, Feb. 1996.

[91] H. Hillbrand and P. H. Russer, "An Efficient Method for Computer Aided Noise Analysis of Linear Amplifier Networks," *IEEE Transactions on Circuits and Systems*, vol. 23, pp. 235–238, Apr. 1976.

Seite Leer /
Blank leaf

List of Publications

[1] A. Huber, C. Bergamaschi, R. Bauknecht, H. Jäckel, and H. Melchior, "RF Noise Characterization of a High Performance InP/InGaAs HBT," in *Proc. of the 20th Workshop on Compound Semiconductor Devices and Circuits*, pp. 83–84, May 1996.

[2] A. Huber, C. Bergamaschi, R. Bauknecht, H. Jäckel, and H. Melchior, "Minimization of the Noise Measure of InP/InGaAs HBTs," in *Proc. of the 9th Intl. Conference on Indium Phosphide and Related Materials*, 1997.

[3] A. Huber, C. Bergamaschi, R. Bauknecht, H. Jäckel, and H. Melchior, "Low-Frequency and Microwave Noise Performance of InP/InGaAs HBTs as a Function of Bias Point, Temperature and Emitter Geometry," in *Proc. of the 21st Workshop on Compound Semiconductor Devices and Circuits*, pp. 122–123, 1997.

[4] A. Huber, C. Bergamaschi, T. Morf, and H. Jäckel, "Broadband Noise Model for InP/InGaAs HBTs," in *10th Intl. Conference on Indium Phosphide and Related Materials*, 1998.

[5] A. Huber, C. Bergamaschi, T. Morf, and H. Jäckel, "A DC–21 GHz High-Gain Noise-Matched InP/InGaAs HBT Differential Amplifier," in *Proc. of the 22nd Workshop on Compound Semiconductor Devices and Circuits*, pp. 78–79, May 1998.

[6] A. Huber, D. Huber, C. Bergamaschi, T. Morf, and H. Jäckel, "A Lumped DC–50 GHz Amplifier using InP/InGaAs HBTs," *IEE Electronics Letters*, vol. 35, pp. 53–55, Jan. 1999.

[7] A. Huber, D. Huber, C. Bergamaschi, T. Morf, and H. Jäckel, "Design and Characterization of a 50 GHz InP/InGaAs HBT Amplifier,"

in *Proc. of the 11th Intl. Conference on Indium Phosphide and Related Materials*, pp. 191–194, 1999.

[8] T. Morf, D. Huber, A. Huber, V. Schwarz, and H. Jäckel, "50 to 70 GHz InP/InGaAs HBT Amplifier with 20 dB Gain," in *Proc. of the 11th Intl. Conference on Indium Phosphide and Related Materials*, pp. 431–434, 1999.

[9] C. Bergamaschi, A. Huber, D. Huber, V. Schwarz, M. Rohner, T. Morf, and H. Jäckel, "High Performance InP-based HBT Technology for Optoelectronic Applications," in *Proc. of the 23th Workshop on Compound Semiconductor Devices and Circuits*, May 1999.

[10] A. Huber, D. Huber, T. Morf, H. Jäckel, C. Bergamaschi, V. Hurm, M. Ludwig, and M. Schlechtweg, "Monolithic, High Transimpedance Gain (3.3 kΩ), 40 Gb/s InP-HBT Photoreceiver with Differential Outputs," *IEE Electronics Letters*, vol. 35, pp. 897–898, May 1999.

[11] V. Schwarz, T. Morf, A. Huber, H. Jäckel, and H.-R. Benedickter, "Differential InP-HBT Current Controlled LC-Oscillator with Center Frequencies of 43 GHZ and 67 GHz," *Electronics Letters*, vol. 35, pp. 1197–1198, July 1999.

[12] T. Morf, S. Hübscher, D. Huber, A. Huber, V. Schwarz, and H. Jäckel, "98-GHz InP/InGaAs HBT Amplifier with 26-dB Gain," *IEEE Microwave and Guided Wave Letters*, vol. 9, pp. 523–525, Dec. 1999.

Acknowledgment

First, I like to thank Prof. Dr. H. Jäckel for his continuous support and his interest in my work. I always appreciated his advices during my time at the Swiss Federal Institute of Technology. I also express my thanks to Prof. Dr. W. Bächtold for his readiness to co-examine this thesis.

My further appreciation goes to Prof. Dr. C. Bergamaschi for his motivating discussions which contributed immensely to successfully accomplish this study.

A special thank is addressed to the members of the 'HBT-group' of the Electronics Laboratory, who were not only co-workers but also friends. Many technical and non-technical discussions helped me to finish this work. My special thanks go therefore to:

- Thomas Morf, the leader of the HBT-group, who always had helpful advices ready on microwave and measurement problems

- Dieter Huber, for wafer processing and the improvements of the transistor technology

- Volker Schwarz, for his support in circuit simulation techniques

- Marcel Rohner who gave assistance in device physics

Furthermore, I acknowledge R. Bauknecht of the Microelectronics and Optoelectronics Laboratory of ETHZ who developed the InP-HBT process and also did material growth and processing.

I like to thank H. R. Benedickter being with the Laboratory of Electromagnetics Fields and Microwave Electronics of ETHZ for his assistance and suggestions during RF and noise measurements.

Finally, I like to thank my parents for their generous support during the whole time of my studies.

Curriculum Vitae

Alex Huber
Citizen of Dietlikon ZH, Switzerland

7. July 1967	Born in Zürich, Switzerland
1974–1980	Primarschule in Dietlikon
1980–1982	Sekundarschule in Dietlikon
1982–1986	Kantonsschule im Lee, Winterthur
1986	Matura Typus C
1987–1990	Studies in Electrical Engineering at the Swiss Federal Institute of Technology, Zürich (ETHZ)
1990–1991	Practical work at Datacolor AG, Dietlikon
1991–1993	Continuation of the studies at ETHZ
1993	Diploma degree in Electrical Engineering at ETHZ (Dipl. El. Ing. ETH)
1993–2000	Research assistant at the Electronics Laboratory of ETHZ The present work was accomplished in the years from 1996–2000.
1999–	Project manager and design engineer at the 'Zentrum für Mikroelektronik' of the 'Fachhochschule Aargau'